

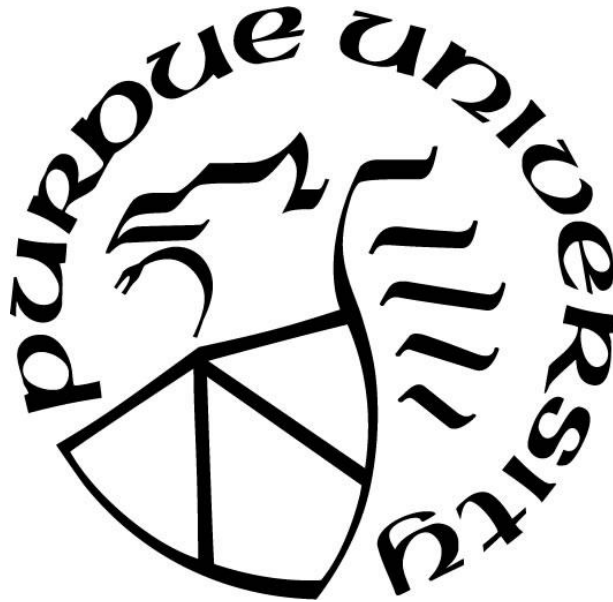
**BIODYNAMIC IMAGING OF BACTERIAL INFECTION AND
ADVANCED PHASE-SENSITIVE SPECTROSCOPY**

by
Honggu Choi

A Dissertation

*Submitted to the Faculty of Purdue University
In Partial Fulfillment of the Requirements for the degree of*

Doctor of Philosophy



Department of Physics and Astronomy

West Lafayette, Indiana

May 2020

**THE PURDUE UNIVERSITY GRADUATE SCHOOL
STATEMENT OF COMMITTEE APPROVAL**

Dr. David Nolte, Chair

Department of Physics and Astronomy

Dr. Andrew Mugler

Department of Physics and Astronomy

Dr. Ken Ritchie

Department of Physics and Astronomy

Dr. Daniel Elliott

Department of Physics and Astronomy

Approved by:

Dr. David Nolte

Devoted to my family and friends

ACKNOWLEDGMENTS

I am greatly indebted by my thesis advisor Dr. Nolte for his considerable support and advisory. It would not be successful without his patients and insights. His disciplines in performing experimental studies have taught me to be an independent researcher. I also thank Dr. Turek for providing cancer cell lines and biopsies with chemotherapeutic agents. Without his help, I would have been in trouble many times. Dr. Ximenes and Dr. Ladisch from LORRE supported me by providing a place for culturing bacteria and preparing culturing medium. I also thank Jessica Zuponic for instructing the equipment and facility usages in LORRE. Also, Dr. Savran provided a tone of support for measuring biodynamic phenotypes of single-cell derived spheroids.

There have been frequent productive discussions with my colleagues, Zhe Li, and Zhen Hua. Our discussion sometimes became arguing, however, they have eventually provided further insights and new perspectives to describe new problems. Also, other colleagues from other laboratories, Jeremy Munsell and Trang Nguyen provided many entertaining moments and kept me away from being depressed. Discussions with Akhil Sheroran and Keichiro Furuya provided many mathematical insights. Also, informal meetings with Michael Vennetilli, Jered Blend, and Terrence Edmonds were a good time to discuss with people outside of my field.

Lastly, I would like to thank my brother Dr. Jungu Choi for introducing me to Dr. Nolte. Thanks to his effort, I was able to start my graduate study at Purdue.

TABLE OF CONTENTS

LIST OF TABLES	7
LIST OF FIGURES	8
ABSTRACT	13
CHAPTER 1. INTRODUCTION TO BIODYNAMIC IMAGING AND ITS APPLICATIONS	14
1.1 Introduction to Biodynamic Imaging.....	14
1.2 Speckle Spectroscopy by Dynamic Light Scattering.....	14
1.3 Low-coherence Light and Coherence-gated Spectroscopy.....	15
1.4 Temporal Fourier Transformation and Power Spectrum	23
1.5 References.....	25
CHAPTER 2. PRECLINICAL TRIAL ON CANINE LYMPHOMA CANCER AND CHOP THERAPY	27
2.1 Introduction to Preclinical Trial for Chemotherapy Efficacy Assessment	27
2.2 Chemotherapeutic Agents Phenotypes Measured by Biodynamic Imaging.....	29
2.3 Phenotype Correlation and Similarity Matrices for Machine Learning.....	29
2.4 Discussion.....	34
2.5 References.....	36
CHAPTER 3. BIODYNAMIC IMAGING OF BACTERIAL SWARMS	38
3.1 Environmental Rapid Change Induced Migration	38
3.2 Nutrient and Osmolarity Shock on Bacteria Pellets	40
3.3 Doppler Spectroscopy of Bacterial Pellets	42
3.4 Tissue Dynamics Spectroscopy (TDS) of Antibiotic Responses.....	46
3.5 Spectral Density Normalization.....	49
3.6 Examples of Normalizations and Representations	51
3.7 Discussion.....	53
3.8 References.....	53
CHAPTER 4. BIODYNAMIC IMAGING OF BACTERIAL INFECTION OF LIVING TISSUE	56
4.1 Infection Assay of Pathogenic Bacteria within a Cell Line	56

4.2	Infection-Induced Intracellular Activity	58
4.3	TDS of Infection Assays	65
4.4	Doppler Spectral Band Analysis	67
4.5	Tissue-dynamic Spectroscopic Imaging of Infection Assay	70
4.6	Antibiotic Responses of Antibiotic Resistance Bacteria	71
4.7	Discussion	74
4.8	References	74
CHAPTER 5. PHASE-SENSITIVE BIODYNAMIC IMAGING.....		76
5.1	Introduction and Background	76
5.2	Dynamic Light Scattering: Homodyne and heterodyne detection	77
5.3	Calibration Experiments	77
5.3.1	Vertically Moving Paper.....	77
5.3.2	Bacterial Dynamics.....	79
5.4	Phase-Sensitive Detection.....	80
5.4.1	Phase Displacements and Probability Density Function (PDF)	81
5.4.2	Probability Density Function (PDF) of Phase Excursions	82
5.4.3	Calibration with Macroscopic Directed Motion	83
5.4.4	PDF of Bacterial Swarms Induced by Nutrient Shock	85
5.4.5	Stabilization of the Heterodyne Doppler Spectrum.....	86
5.5	Levy Stable Distributions	88
5.6	Levy Spectroscopy	91
5.6.1	Levy-like Characteristics of PDFs.....	91
5.6.2	Bacteria and Host-cell Selection and Preparation	93
5.6.3	Infection Assay	93
5.7	Conclusions.....	95
5.8	References.....	96
APPENDIX A. DOPPLER LIGHT SCATTERING FROM INTRACELLULAR DYNAMICS OF SINGLE-CELL DERIVED SPHEROIDS.....		99
PUBLICATIONS.....		106

LIST OF TABLES

Table 3.1 Bacterial strains and corresponding physical characteristics.....	39
Table 3.2 Bacterial strain information	39
Table 5.1 Response characteristics to different reagents.	86
Table 5.2 Levy Alpha Spectroscopy of Bacterial Infections.	95

LIST OF FIGURES

- Figure 1.1 Schematic diagram of volumetric scattering from a biological specimen. Reflected light forms volumetric speckle at an image plane of the collecting optics. Selective interference is possible by adjusting the optical path delay in a reference beam. With shorter coherence, a better volumetric resolution is possible. 16
- Figure 1.2 Optical configuration of biodynamic imaging (BDI). A Mach-Zehnder interferometer with low-coherence light forms an off-axis digital holographic interference pattern at the camera by adjusting the optical path delay at the reference arm. The optical delay can be adjusted in 1 μm steps. The beam splitters BS2 and BS3 are slightly tilted (2 degrees) to avoid specular reflection from a specimen [6-8]. 17
- Figure 1.3 OCI reconstruction by Fourier transform. (a) Fourier image taken at the FP (b) two conjugated twin images after performing spatial Fourier transform on the Fourier image (c) speckle reconstruction at the FP after demodulation, and (d) autocorrelation of the FP speckle. 18
- Figure 1.4 DLS with randomly moving particles. Particles in 3-dimensional space have isotropic dynamic densities. Doppler shifts with 3D Isotropic motion induce a broadband Doppler shift. The broadband power spectrum has a power-law shape [17]. 20
- Figure 1.5 Example of an intensity time series in dynamic speckle. 22
- Figure 1.6 Backscatter brightness (BSB) map of reconstructed holographic image (OCI) and motility contrast image (MCI) of a canine lymphoma biopsy. OCI and MCI of post-dose speckle were measured 7 hours after adding CHOP (doxorubicin (10 μM), 4-hydroxycyclophosphamide (5 μM), vincristine (60 nM), and prednisolone (0.6 μM) with 0.1% DMSO) [19]. 23
- Figure 1.7 Calibration experiments on dynamic speckle and power spectra. (a) Schematic diagram of the experimental design. Two identical pieces of paper were prepared in plastic wells. One is fixed at the bottom and the other one is sinking with a constant velocity caused by the water surface evaporation. (b) Homodyne fluctuation power spectra of the two paper targets on a log-log scale. A Doppler peak appears in the power spectrum of the sinking paper at 0.45 Hz, which corresponds to a settling speed of 150 nm/s. 24
- Figure 2.1 Spectrograms of various drug-response phenotypes. (a) Drug-resistant spectrograms and (b) sensitive spectrograms. (c) Spectrogram difference between resistant and sensitive groups. Prednisolone showed a minimal phenotypic difference, and Doxorubicin showed the most significant phenotypic difference [19]. 30
- Figure 2.2 (a) Feature vectors of patients and (b) similarity matrix. (c) Progression-free survival time (PFS) [19]. 31
- Figure 2.3 Comparison of log-likelihood and perceptron quorum. Two linear separabilities in N-dimensional space showed 84 % accuracy according to patient PFS [19]. 33
- Figure 2.4 Similarity network between canine patients. Red nodes and blue nodes represent short-PFS and long-PFS respectively. The separation between short-PFS and long-PFS showed 84% accuracy with one false-negative and two false-positives [19]. 34

Figure 3.1 SEM pictures of (a) <i>E. coli</i> [10] (b) <i>S. enterica</i> [11] and (c) <i>L. monocytogenes</i> [12]. The dynamic and physical characteristics are shown in the table below.	39
Figure 3.2 OCI and MCI image of <i>E. coli</i> pellet. LB medium was applied to induce a motility response. Post-dose OCI and MCI were measured immediately after applying the lysogeny-broth (LB) medium. MCI enhancement at post-dose is prominent when compared to baseline MCI. .	41
Figure 3.3 Temporal responses of BSB and NSD for <i>Escherichia coli</i> (<i>E. coli</i>), <i>Salmonella enterica</i> (<i>S. enterica</i>), and <i>Listeria monocytogenes</i> (<i>L. monocytogenes</i>) pellets after applying various reagents. The three curves represent the temporal responses of the old medium, 1% NaCl and the LB medium, respectively. All data points are 3-replicate averages.	42
Figure 3.4 Baseline spectra of <i>E. coli</i> , <i>S. enterica</i> , and <i>L. monocytogenes</i> . The spectra in all three samples show with 1/f-like spectral density. The expected bacterial dynamics of the spectral densities are 3D isotropic motion [20]......	43
Figure 3.5 Example of a Doppler-edge fit to the bacterial pellet response to a nutrient shock. The average edge frequency and Doppler number are shown for two times: one immediately after the nutrient application, and another 2 minutes later, showing a rapid relaxation back towards the 1/f spectrum.	44
Figure 3.6 (a) Doppler edges produced by applying the LB medium. (b) Relative spectral enhancements of <i>E. coli</i> , <i>S. enterica</i> , and <i>L. monocytogenes</i> pellets are demonstrated. The responses occurred immediately after applying the LB medium.....	45
Figure 3.7 Nutrient shock-responses of <i>E. coli</i> , <i>S. enterica</i> , and <i>L. monocytogenes</i> pellets. Dramatic low-frequency enhancement occurred (the Doppler edge). The nutrient shock showed the strongest response in <i>E. coli</i> . Spectra were normalized by the baselines averages. (Intensity normalization)	46
Figure 3.8 Response of <i>E. coli</i> pellets to ethanol (70 %). The response is inhibitory with strong 60% suppression in the mid and lower frequencies.....	47
Figure 3.9 Spectrograms of <i>E. coli</i> pellets after applying NaOH and bleach respectively. Low frequency is highly suppressed after adding chemical agents.	47
Figure 3.10 (a) Ciprofloxacin (Cipro) responses of <i>E. coli</i> , <i>S. enterica</i> , and <i>L. monocytogenes</i> respectively. (b) The spectral response within 2 minutes after applying Cipro to the three bacterial strains. The Nyquist floors for 3 strains showed almost identical values. The low-frequency responses were immediate and weaker than for the LB medium. <i>L. monocytogenes</i> has the weakest response to Cipro. The corresponding spectrograms are shown in Figure 3.11	48
Figure 3.11 Cipro response spectrograms of <i>E. coli</i> , <i>S. enterica</i> , and <i>L.monocytogenes</i> . All strains do not have Cipro resistance.	49
Figure 3.12 Spectrograms obtained from different normalization methods. <i>S. enterica</i> infection of DLD-1 (10^7 CFU/well).	50
Figure 3.13 <i>L. monocytogenes</i> infection of DLD-1 with different extracellular matrix (ECM) densities. Infection signature by <i>L. monocytogenes</i> of DLD-1 with lower ECM density (U-bottom growth) and higher ECM density (bioreactor growth). The red dashed lines represent the <i>L. monocytogenes</i> inoculation by 10^6 CFU per well. The average rate of <i>L. monocytogenes</i> infection	

of higher ECM density shows slower development. The vertical dashed lines represent the frequency shift of maximum Doppler spectral density at f_1 to f_2 52

Figure 4.1 *L. monocytogenes* infection mechanism. (From [5]) *L. monocytogenes* physically penetrate a host cell's membrane and internalize. After internalization, *L. monocytogenes* polymerize actin molecules and form polymeric Filament-actins (F-actin). The F-actin formation at the end of *L. monocytogenes* physically pushes toward the neighboring host cell and spreads the infection. The average propulsion speed is about 10 $\mu\text{m}/\text{min}$ 57

Figure 4.2 *S. enterica* internalization. (From [6]). *S. enterica* adheres to a host cell's membrane and manipulates F-actin formation. F-actin formation induces a local cellular membrane motion that engulfs *S. enterica*. Internalized *S. enterica* uses the host cell's resources and replicates. After multiple replications inside of a host cell *S. enterica* saturates, bursts, and releases *S. enterica* daughter cells that forage other host cells..... 58

Figure 4.3 Inoculation with 10^7 CFU/well. (a) BSB change of *E. coli* and *S. enterica*, *L. monocytogenes*, and *L. innocua* after inoculation in DLD-1 spheroids (red dashed lines). (b) Temporal responses of NSD. 59

Figure 4.4 Inoculation by a lower number of bacteria (10^6 CFU/well). (a) BSB enhancement of all strains showed a similar degree of enhancement. (b) NSD of *L. monocytogenes* decreased most rapidly and *S. enterica* showed the slowest decrease. 60

Figure 4.5 Dynamic range of (a) 10^7 CFU/well and (b) 10^6 CFU /well. The lower dose inoculation shows temporally delayed responses. 10^6 CFU inoculation of *L. monocytogenes* shows different behavior of 10^7 CFU which suggests 10^7 CFU inoculation partially captures Doppler signals from rapidly moving bacteria as well. 61

Figure 4.6 Initial and final (a) OCI and (b) MCI of DLD-1 spheroids infection by various bacteria strains by inoculating 10^7 CFU/well. 63

Figure 4.7 (a) OCI and (b) MCI for 10^6 CFU/well inoculation. 64

Figure 4.8 Spectrum of DLD-1 under infection by 10^7 CFU/well of *E. coli*. The time difference between the baseline and the final measurement is 6 hours. 65

Figure 4.9 Tissue dynamics spectrograms (TDS) of DLD-1 tissue spheroids inoculated (red dashed lines) by 10^7 CFU/well of *E. coli*, *S. enterica*, *L. monocytogenes*, and *L. innocua*..... 66

Figure 4.10 Spectrograms of *E. coli*, *L. monocytogenes*, and *S. enterica* at 10^6 CFU/well..... 67

Figure 4.11 Time development of the relative spectral changes for a dose of 10^7 CFU/well. (a) The low-frequency limit for the rheology band. All bacterial strains showed temporal variation in this band. *E. coli* infection displays the strongest suppression. The two pathogenic strains, *S. enterica*, and *L. monocytogenes* show non-monotonic increases, with a decrease after the first maximum, followed by a long-term increase. Long-term increases for the rheology band have been associated with blebbing or the formation of apoptotic bodies associated with either uncontrolled or controlled cell death. *L. innocua* show a slow and monotonic increase. (b) Change in the Doppler rheology band for three selected times and standard errors. (c) Time dependence of the high-frequency band associated with organelle transport. *L. monocytogenes* show strong initial increases within one hour followed by a slow decrease at longer times. *S. enterica* show a

weak enhancement at 3 hours after inoculation. The case for *E. coli* shows strong suppression consistent with an overall inhibition of Doppler activity. (d) Change in the Doppler organelle transport band at three selected times. 69

Figure 4.12 An example of tissue-dynamic spectroscopic imaging (TDSI). The blue and red color represents a blueshift or a redshift of power spectral density. The region R1 and R2 show different spectral shifts. 70

Figure 4.13 Bacterial infection and the corresponding TDSI. The invasive strains (*S. enterica* and *L. monocytogenes*) show spreading blueshift while non-invasive strains (*E. coli* and *L. innocua*) did not. Lower graphs represent a 1D plot at the centers of TDSIs. 71

Figure 4.14 Ampicillin resistant *E. coli* colony formation on an agar plate (a) with ampicillin and (b) with Cipro. (c) The RPMI-1640 medium inoculated by 10^6 CFU/well *E. coli* and incubated for 24 hours. The pH of the RPMI-1640 medium was altered by the *E. coli* growth but the medium with Cipro did not. The increment of pH of the RPMI-1640 medium is caused by losing CO_2 dissolved in the bicarbonate buffer. 72

Figure 4.15 Antibiotic-resistant assay. The upper row group was inoculated by *E. coli*. The lower group was not inoculated. The first column was treated by the RPMI-1640 growth medium without antibiotics. The second column was treated by RPMI-1640 with ampicillin (50 $\mu\text{g}/\text{mL}$). The last column was treated by Cipro (3.5 $\mu\text{g}/\text{mL}$). The group treated by Cipro completely recovered from the infection. 73

Figure 5.1 Calibration experiments of the power spectra of dynamic speckle. (a) Schematic diagram of BDI and (b) reconstructed hologram intensity and phase at a fixed time. Speckle formed at the image plane (IP) is Fourier transformed to the Fourier plane (FP). (c) Homodyne and heterodyne power spectra of the vertically moving paper due to the water surface evaporation. A Doppler peak appears in the power spectrum of the sinking paper at 0.45 Hz, which corresponds to a settling speed of 150 nm/s. (d) Homodyne power spectral density enhancement of *Escherichia coli* (*E. coli*) pellet by applying the Lysogeny broth (LB) medium shows a prominent Doppler edge, (e) while the heterodyne power spectra cannot detect the Doppler edge. 78

Figure 5.2 Schematic diagram of dynamic light scattering. The total phase value ϕ_{tot} is determined by contributions of N identical photons with slightly different phases. Black and red arrows represent the average velocities of scattering elements over the sampling window (40 ms) and wave vectors of scattered photons, respectively. When photons interact with (a) 3D random isotropic dynamic particles, the average phase displacement of the Doppler shift per sampling window becomes zero. (b) On the other hand, when the dynamic particle has 3D ballistic dynamics or 1D isotropic motion, the average phase displacement of the Doppler shift has a non-zero value. 80

Figure 5.3 Doppler information acquisition from functional images. (a) Schematic diagram of phase information time series of dynamic speckle. $PDF(\tau)$ is obtained from the subtraction between frames with a τ difference and histogrammed. PDFs of (b) stationary paper and (c) slowly moving paper in Figure 5.1 (b) and the corresponding 2D PDF representations of (d) stationery paper and (e) moving paper. The Doppler slope of the average displacement $\Delta\bar{\phi}$ shown in (f) with different time intervals in (c) is 2.70 rad/s which corresponds to 0.43 Hz and 143 nm/s by Eq. 5.6.

The Doppler peak of the power spectrum in Figure 5.1(b) and the average phase displacement of the PDF show good agreement. 84

Figure 5.4 Temporal evolution of PDFs of *E. coli* pellets and Doppler slopes. (a) Temporal response of PDFs immediately after applying negative-control reagents (perturbed medium with a pipette and adding 1% NaCl medium) and (b) high-osmotic pressure solution (7% NaCl), and nutrient (LB). (c) Doppler slopes from PDFs. One data point represents a single measurement. Applying medium (pipetting perturbation) and 1% NaCl solution (LB medium base without nutrient compound) did not induce significant shifts. 7% NaCl (osmotic shock) and LB (nutrient shock) media showed shifts of PDFs with opposite signs. 85

Figure 5.5 (a) PDF of the vertically moving paper from Figure 5.3 (b) Autocorrelation (AC) obtained from (a) by Eq. (5.12). The AC of negative time is the complex conjugate of positive time, so the real valued AC is symmetric and the imaginary valued AC is asymmetric. (c) The power spectrum derived from the complex autocorrelation by the Weiner-Khinchin theorem and compared with the heterodyne spectrum. Positive and negative spectral components are compared. (d) Homodyne power spectrum of nutrient shock applied to an *E. coli* pellet and (e) the raw heterodyne power spectrum. (f) Heterodyne power spectrum derived from PDFs in Figure 5.4(b). For the relative spectral density comparisons, all Nyquist floors were calibrated to have the same values at 12.5 Hz. 88

Figure 5.6 Levy stable probability distribution functions between $\alpha = 1$ (Cauchy) and $\alpha = 2$ (Gaussian). The heavy tail is seen even for $\alpha = 1.99$ close to the Gaussian case. 90

Figure 5.7 PDFs of various targets fitted with Levy, Gaussian, and Cauchy distributions of (a) stationary paper, (b) vertically moving paper, (c) DLD-1 spheroids, and (d) *E. coli* pellet. The Cauchy probability density shows power-law tails with $a = 1$ (black solid lines) and the Gaussian probability density with $\alpha = 2$ (green solid lines). Levy distributions show similar heavy tails of experimentally obtained PDFs'. The power-law tails of Levy probability densities are numerically obtained and fitted with the smallest residual squares. To quantify the slopes of the power-law tails, the maximum likelihoods of PDFs are shifted at $\Delta\phi = 0$ to plot symmetrically. 92

Figure 5.8 Levy Alpha spectroscopy infection assays. Two bacterial strains with the same genus with different pathogenicities were inoculated into DLD-1. (a) Examples of PDF and Levy distribution comparison. *Listeria innocua* (*L. innocua*) induces a slight change in the Levy alpha while *Listeria monocytogenes* (*L. monocytogenes*) significantly decreased the Levy alpha. (b) Statistical analysis of the Levy alpha value change ($\Delta\alpha$) of 12 replicates. Bacteria were inoculated at 60 min (Red-dashed line) and PDFs were measured for 6 hours. The Levy alpha changes of the control and the *L. innocua* infection group showed comparable variations, while *L. monocytogenes* showed a significant decrease in the alpha. (c) The histogram of Levy alpha value spectroscopy, collected from Figure 8(b). Invasive *L. monocytogenes* induces Levy-alpha shifts while passive *L. innocua* shows only a minor shift on the average Levy-alpha value. Control and baselines showed almost identical statistical behaviors. Lines are fitted Gaussian distributions. 94

ABSTRACT

Biological dynamics have been studied by many methods. Fluorescence dynamic microscopy and optical coherence tomography provided fundamental understandings of biological systems. However, their high NA optics only represent local characteristics. Biodynamic imaging (BDI) technique implements a low NA optics and acquires the statistical average of Doppler shifts that occurred by dynamic light scattering with biological dynamic subsystems provided globally averaged dynamic characteristics.

BDI is used for this study to investigate biomedical applications. The chemotherapy efficacy measurement by BDI demonstrated a good agreement between the Doppler spectral phenotypes and the preclinical outcomes. Also, dynamic responses of microbiomes by chemical stimuli demonstrated featured Doppler characteristics. The bacterial infection of epithelial spheroids showed consistent spectral responses and antibiotic-resistant *E. coli* infection treatment with a sensitive and resistive antibiotic showed a dramatic contrast. Furthermore, the phase-sensitive characteristics of BDI provided a clue to understanding the characteristics of the random process of biological systems. Levy-like heavy-tailed probability density functions are demonstrated and the shape changed by infection will be discussed.

CHAPTER 1. INTRODUCTION TO BIODYNAMIC IMAGING AND ITS APPLICATIONS

1.1 Introduction to Biodynamic Imaging

Biodynamic imaging (BDI) is a biomedical imaging technique that is performed *in vitro* on small (mm^3 – size) living tissue samples. The image contrast is provided by intracellular motion, which is detected through volumetric dynamic speckle using a low-coherence light source. Speckle forms when coherent light illuminates a heterogeneous target and is reflected as partial waves that have random intensity and phase distributions. The speckle intensity distribution would be static if a specimen has no internal dynamics. However, intensity fluctuations from living tissue are caused by Doppler shifts from light scattering from dynamic processes within a specimen. Typical Doppler shifts from intracellular motions are in the range from 0.01 Hz to 10 Hz, arising from intracellular speeds between 3 nm/s to 3 $\mu\text{m/s}$ using the current measurement scheme.

1.2 Speckle Spectroscopy by Dynamic Light Scattering

Dynamic light scattering (DLS) measures light intensity correlations of random light scattered from a dynamic specimen [1-4]. Dynamics are represented through the correlation function of the speckle, obtained by time-autocorrelation $A(\tau)$ or temporal Fourier transformation $S(\omega)$ that are related through the Wiener-Khinchin Theorem [5]

$$S(\omega) = \int_{-\infty}^{\infty} A(\tau) e^{-i\omega\tau} d\tau \quad (1.1)$$

In much of the following presentation, temporal Fourier transformation is the primary approach used to measure a specimen's dynamics through Doppler frequency shifts.

Dynamics within a specimen, such as molecular transport, membrane undulations or cellular shape changes, have different velocities and different persistence times. (Note that thermal molecular diffusion has time scales too fast to detect with our system. Hence, all dynamics measured by BDI relate to active transport driven by molecular motors and cytoskeletal restructuring.) The dynamics are represented in dynamic speckle intensity as beats among their Doppler frequency shifts induced by light scattering from moving particles inside the specimen. When a photon

propagates with a wave vector \mathbf{k}_1 , it becomes \mathbf{k}_2 after scattering with a dynamic particle, and the momentum transfer is

$$\mathbf{q} = \mathbf{k}_1 - \mathbf{k}_2 \quad (1.2)$$

where the magnitude of the transferred momentum into a scattering angle θ is

$$|\mathbf{q}| = 2k \sin\left(\frac{\theta}{2}\right) \quad (1.3)$$

The frequency shift of a photon $\Delta\omega = \omega_D$ is related to a particle's speed \mathbf{v} through

$$\omega_D = \mathbf{q} \cdot \mathbf{v} \quad (1.4)$$

In our experiments, $\lambda = 840$ nm, and the maximum amplitude of the momentum transfer vector \mathbf{q} is $20 \mu\text{m}^{-1}$ in our backscattering geometry. The Doppler frequency shift by a particle with a $1 \mu\text{m/s}$ velocity corresponds to a 3 Hz frequency shift [6-8].

1.3 Low-coherence Light and Coherence-gated Spectroscopy

Spectroscopy can study material characteristics by measuring optical absorption and reflection [9-12]. Low-coherence light has replaced pulsed lasers in the spectroscopy of biomedical optics because low-coherence light can generate optical coherence without requiring pulsed lasers [13-15]. Pulsed lasers operating in direct detection of time-of-flight require precise temporal control, while low-coherence only requires spatial precision, which is easier to accomplish. The low-coherence light source has a limited coherence length that enables optical-path specific interference. To form an interference pattern with the low coherence light, the optical path lengths of the reference and the object arm should be matched within the coherence length. Selective interference using the advantage of short-coherence is called *coherence gating* because the coherence-gated position determines the selected section of the optical coherence image (OCI). Furthermore, 3-dimensional OCI reconstruction of a volumetric structure is possible by scanning through a volume with the coherence-gate.

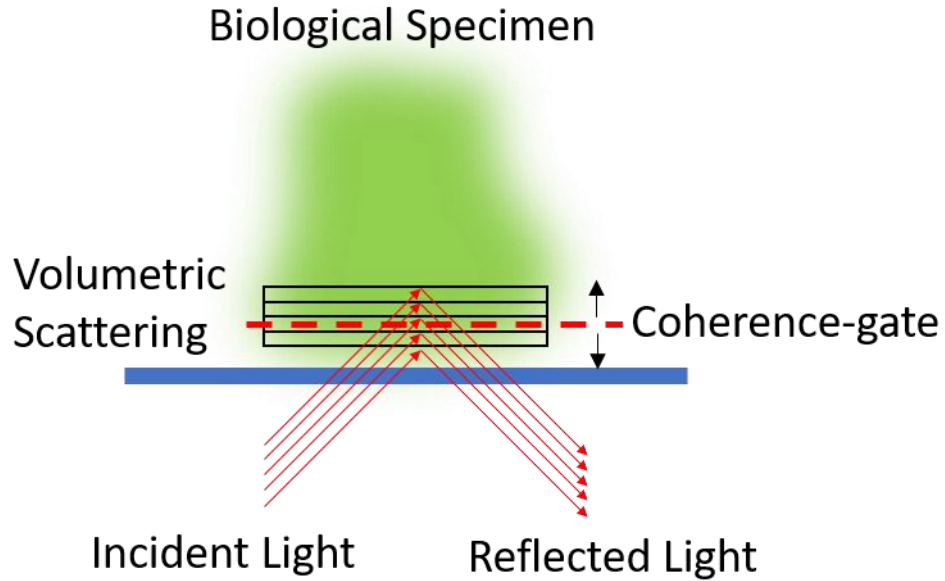


Figure 1.1 Schematic diagram of volumetric scattering from a biological specimen. Reflected light forms volumetric speckle at an image plane of the collecting optics. Selective interference is possible by adjusting the optical path delay in a reference beam. With shorter coherence, a better volumetric resolution is possible.

The optical configuration of the BDI Mach-Zehnder-type interferometer is shown in Figure 1.2. Low-coherence light (central wavelength $\lambda = 840$ nm, Superlum S850-G-I-20, coherence length $20\mu\text{m}$) is split into object and reference arms with a 9:1 intensity ratio. The beam in the object arm illuminates the specimen at normal incidence. Reflected speckle is collected by lens L1. The speckle is transferred to the image plane (IP) by a 4-f system (L1 and L2, $f = 15$ cm). The Fourier lens (L3, $f = 5$ cm) performs a Fourier transform and forms a Fourier image at the Fourier plane (FP) where it is recorded by the camera (QImaging, Rolera EM-C2) with 25 fps sampling frequency. The coherence-length of the low-coherence light is approximately $20\mu\text{m}$, and the optical path lengths of the object and reference arms are matched to within $20\mu\text{m}$ to form an interference pattern at the FP. Volumetric light scattering from the specimen can be selectively interfered by adjusting the optical path delay in the reference arm.

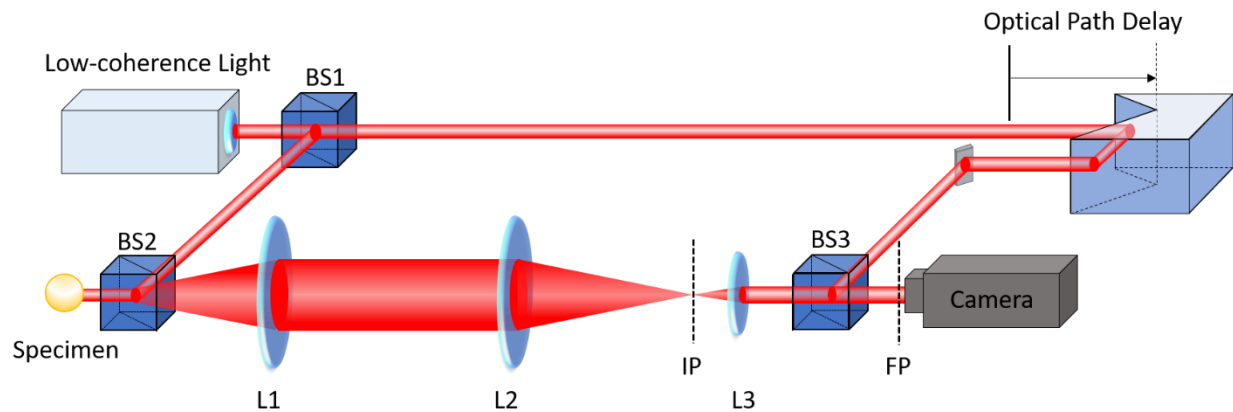


Figure 1.2 Optical configuration of biodynamic imaging (BDI). A Mach-Zehnder interferometer with low-coherence light forms an off-axis digital holographic interference pattern at the camera by adjusting the optical path delay at the reference arm. The optical delay can be adjusted in $1\ \mu\text{m}$ steps. The beam splitters BS2 and BS3 are slightly tilted (2 degrees) to avoid specular reflection from a specimen [6-8].

Holographic reconstruction is performed using a 2-dimensional spatial Fourier transform on the Fourier image that is captured by the digital camera at the FP. A Fourier image is shown in Figure 1.3 (a) with a fringe orientation at approximately 135-degrees and the Fourier transform has two conjugated images in the 1st and 3rd quadrants.

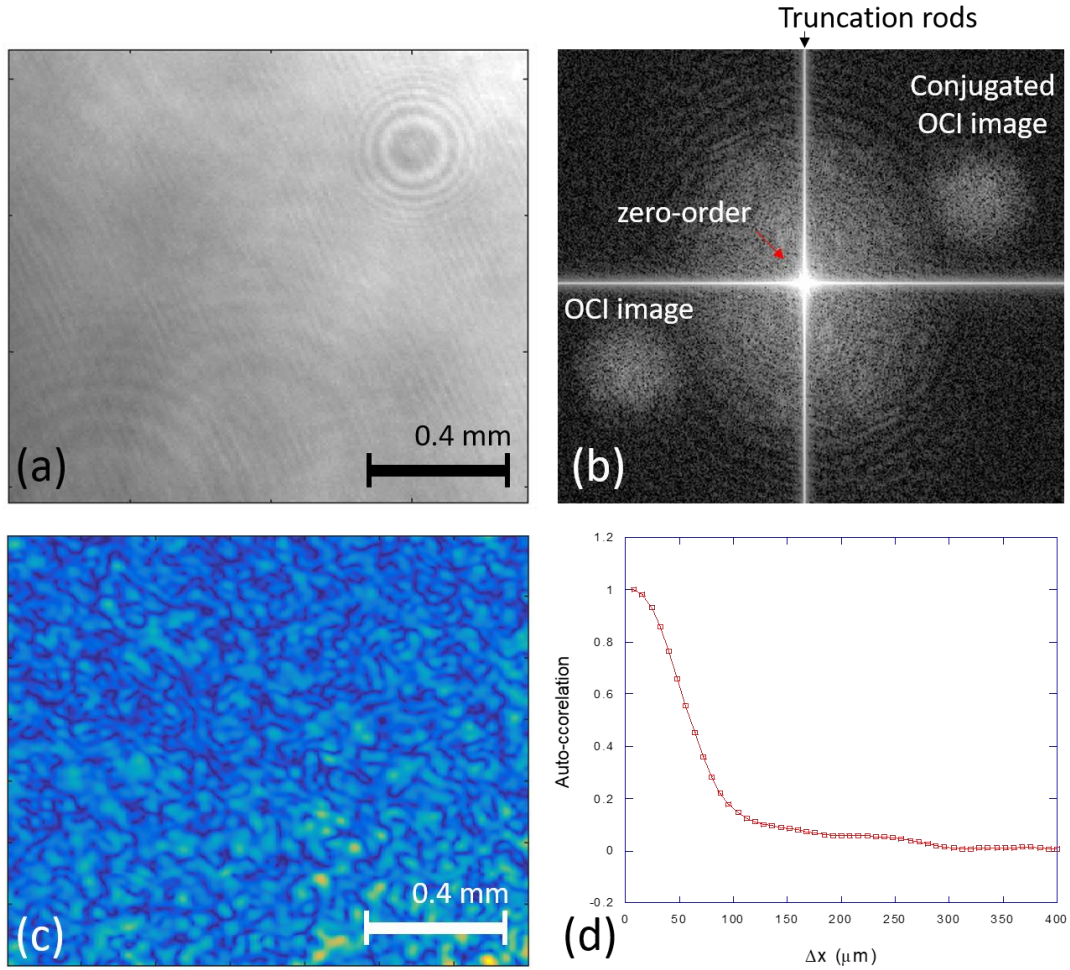


Figure 1.3 OCI reconstruction by Fourier transform. (a) Fourier image taken at the FP (b) two conjugated twin images after performing spatial Fourier transform on the Fourier image (c) speckle reconstruction at the FP after demodulation, and (d) autocorrelation of the FP speckle.

The two images are identical OCI versions of the specimen but are phase conjugated. The intensity of the 1st quadrant OCI in Figure 1.3 (b) was obtained by taking the absolute value of the complex field squared at each reconstructed pixel. The speckle size was estimated by demodulating a carrier frequency [16] in Figure 1.3 (a) and performing an inverse Fourier transform to obtain speckle at the FP, shown in Figure 1.3 (c). The spatial autocorrelation in Figure 1.3 (d) shows the size of speckle which is approximately 80 μm on the FP.

The scattered light collected at the FP by L3 with the aperture Σ and the focal length f can be approximated by Fraunhofer diffraction. The electric field of the light scattered from the object at the FP is

$$\psi_{FP}^{obj}(x, y) \approx \iint_{\Sigma} e^{i\frac{q}{f}(xx'+yy')} dx' dy' \quad (1.5)$$

Assuming the reference beam is a plane wave propagating with the direction \mathbf{r} , the interference intensity at the FP becomes

$$\left| \psi_{FP}^{obj}(x, y) + \psi_{FP}^{ref}(x, y) \right|^2 \approx I_{DC} + 2 \operatorname{Re} \left[e^{-i\mathbf{q}\cdot\mathbf{r}} \iint_{\Sigma} e^{i\frac{q}{f}(xx'+yy')} dx' dy' \right] \quad (1.6)$$

where I_{DC} is a background intensity that does not interfere. Recorded holograms at the Fourier plane are reconstructed by performing a spatial Fourier transform of Eq.(1.6). The OCI distribution at the digitally reconstructed holographic image is

$$OCI(x, y) \approx \lambda f \left[\Sigma \delta(x - r_x, y - r_y) + \Sigma^* \delta(x + r_x, y + r_y) \right] \quad (1.7)$$

The locations of the OCIs are at $\mathbf{x} = (r_x, r_y)$ and $\mathbf{x} = (-r_x, -r_y)$ with complex conjugate phase. The maximum spatial frequency is limited by the Nyquist sampling theorem so 3 pixels record one fringe. The center of the OCI should be at 45 degrees from the origin to avoid overlapping with truncation rods, then the spatial frequency of the holographic images at the FP is

$$k_x = k_y = \frac{1}{3\Delta x} = \frac{1}{3W_{pixel}} \quad (1.8)$$

When the CCD pixel size is 8 μm then the spatial frequency of the fringes W_{pixel} is 40 mm^{-1} .

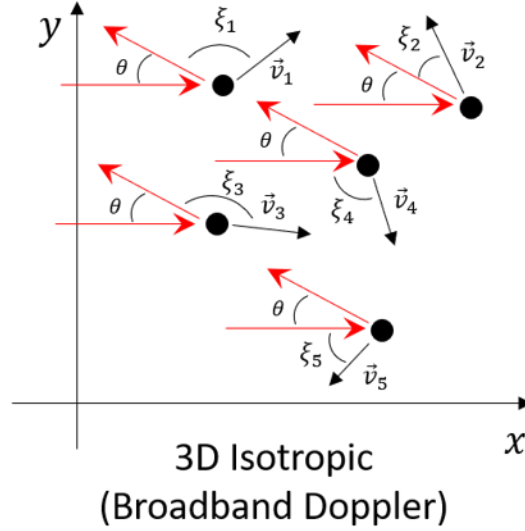


Figure 1.4 DLS with randomly moving particles. Particles in 3-dimensional space have isotropic dynamic densities. Doppler shifts with 3D Isotropic motion induce a broadband Doppler shift. The broadband power spectrum has a power-law shape [17].

Scattered light from randomly moving particles in Figure 1.4 forms temporally fluctuating dynamic speckle. The intensity fluctuation is induced by particles' dynamics [1]. The $g^{(2)}(\tau)$ correlation function of the intensity fluctuation is the conventional way of quantifying the dynamic characteristics of particles.

$$g^{(2)}(\tau) = \frac{\langle I(t)I(t+\tau) \rangle_t}{\langle I(t) \rangle_t^2} \quad (1.9)$$

The $g^{(2)}(\tau)$ correlation function is an intensity correlation, and the power spectrum derived from $g^{(2)}(\tau)$ is a homodyne power spectrum. A phase-sensitive correlation is

$$g^{(1)}(\tau) = \frac{\langle E(t)E(t+\tau) \rangle_t}{\langle E(t) \rangle_t^2} \quad (1.10)$$

and has a complex value. For classical random light, $g^{(1)}(\tau)$ and $g^{(2)}(\tau)$ have a relation that is [18]

$$g^{(2)}(\tau) = 1 + |g^{(1)}(\tau)|^2 \quad (1.11)$$

Performing a temporal Fourier transform on $g^{(1)}(\tau)$ gives a heterodyne power spectrum. The $g^{(2)}(\tau)$ correlation function in Eq. (1.11) is a phase-insensitive measurement, because taking an absolute value of $g^{(1)}(\tau)$ loses phase dependence. However, the intensity fluctuations induced by random interference carry phase information by Eq.(1.4). Therefore, the beating interference caused by the Doppler shifts enables measurements of Doppler shifts indirectly. Homodyne and heterodyne spectra have mathematically similar characteristics with different sensitivities due to the beating interference. A more detailed analysis will be provided in CHAPTER 5. Because our interest is in Doppler shifts, the analysis results will be represented in power spectra.

Dynamic speckle has intensity fluctuations caused by the specimen's internal dynamics. One simple estimate of the motility of a specimen is the normalized standard deviation (NSD) of the intensity time series, which is [6-8]

$$NSD(x, y) = \sqrt{\frac{1}{N} \sum_{t=1}^N \left[\frac{I_t(x, y) - \bar{I}(x, y)}{\bar{I}(x, y)} \right]^2} \quad (1.12)$$

where N is the number of OCI time series. A map of NSD represents a motility contrast image (MCI) which shows the dynamic activity of a specimen.

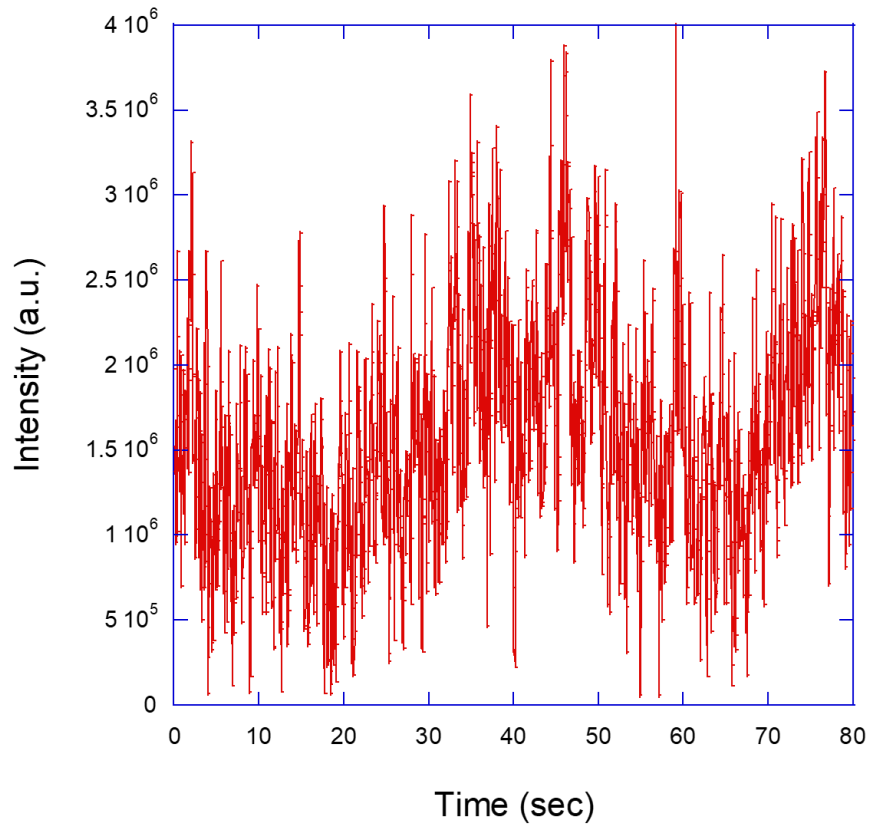


Figure 1.5 Example of an intensity time series in dynamic speckle.

Examples of OCI and MCI are shown in Figure 1.6. OCI is the temporal-average intensity of speckle. The baseline MCI has NSD values close to 1, which represents a highly active state. However, after adding chemotherapeutic agents, the MCI is significantly suppressed.

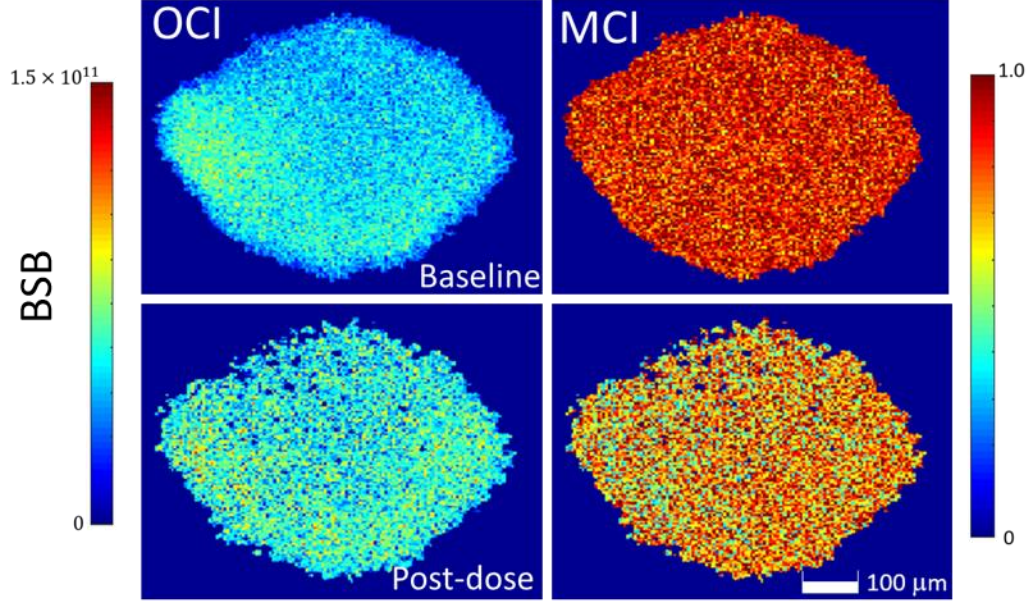


Figure 1.6 Backscatter brightness (BSB) map of reconstructed holographic image (OCI) and motility contrast image (MCI) of a canine lymphoma biopsy. OCI and MCI of post-dose speckle were measured 7 hours after adding CHOP (doxorubicin (10 μ M), 4-hydroxycyclophosphamide (5 μ M), vincristine (60 nM), and prednisolone (0.6 μ M) with 0.1% DMSO) [19].

1.4 Temporal Fourier Transformation and Power Spectrum

A power spectrum can be obtained by conducting a temporal Fourier transform on a time-dependent signal. Dynamic speckle produces a time series from an intensity array. Conducting a temporal Fourier transform on speckle time series produces a power spectrum of the dynamic speckle. The temporal Fourier transform for obtaining a power spectrum is

$$S(\omega) = \frac{1}{N} \sum_{r_{ij}}^N \left| \int_{-\infty}^{\infty} I(r_{ij}, t) e^{i\omega t} dt \right|^2 \quad (1.13)$$

where, $I(r_{ij}, t)$ is the time series of intensity at coordinate r_{ij} , and the total number of pixels is N .

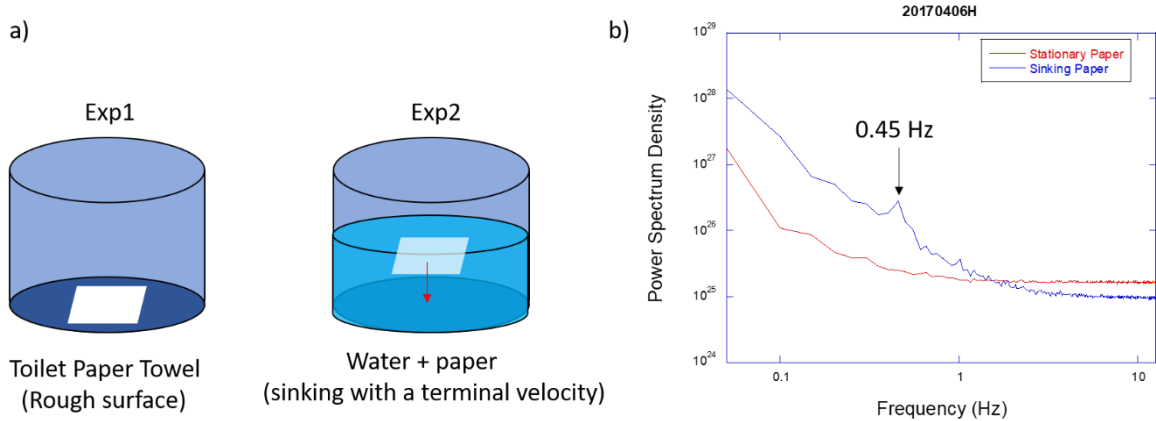


Figure 1.7 Calibration experiments on dynamic speckle and power spectra. (a) Schematic diagram of the experimental design. Two identical pieces of paper were prepared in plastic wells. One is fixed at the bottom and the other one is sinking with a constant velocity caused by the water surface evaporation. (b) Homodyne fluctuation power spectra of the two paper targets on a log-log scale. A Doppler peak appears in the power spectrum of the sinking paper at 0.45 Hz, which corresponds to a settling speed of 150 nm/s.

Dynamic speckles from two identical pieces of paper were measured (shown in Figure 1.7). One remained stationary, and the other vertically moved with a constant velocity caused by water surface evaporation. The water temperature was set to be 37 degrees Celsius and the evaporation speed was estimated at 10 mm/day (100 nm/s). To measure the speed of paper induced by water evaporation, a circular shaped paper with a 3 mm diameter and 15 μm thickness floated at the water surface. The diameter of the paper was slightly smaller than the radius of a 96-well plate's reservoir diameter. When the paper was at the coherence-gated depth, a holographic dynamic speckle was recorded with 25 fps for 20 seconds. Fourier transformation on the 500-frame intensity time series has 249 positive and negative non-zero frequency components and one DC component at $\omega = 0$. Positive and negative non-zero Fourier components are symmetric, and the positive components are plotted in Figure 1.7 (b). The homodyne power spectrum shows a clear peak at 0.45 Hz, which corresponds to a constant velocity of 150 nm/sec for the vertically moving paper. The homodyne spectrum shows only a “residual” Doppler peak. In Chapter 5, a phase-sensitive heterodyne power spectrum will be shown that displays a strong Doppler signature for the sinking paper target. Because living tissue has isotropic motion (and little or no directed motion), the homodyne detection approach provides the characteristic Doppler spectrum while maintaining

better spectral stability compared to phase-sensitive heterodyne detection. This will be part of the discussion of CHAPTER 5.

1.5 References

- [1]. W. I. Goldberg, "Dynamic light scattering," *American Journal of Physics* **67**(1999).
- [2]. B. J. Berne and R. Pecora, *Dynamic light scattering : with applications to chemistry, biology, and physics*, Dover ed. (Dover Publications, Mineola, N.Y., 2000), pp. vii, 376 p.
- [3]. R. Pecora, "Dynamic Light Scattering Applications of Photon Correlation Spectroscopy," pp. 1 online resource (XIV, 420 p. 422 illus.).
- [4]. S. R. Aragon and R. Pecora, "Theory of dynamic light scattering from polydisperse systems," *J. Chem. Phys* **64**(1976).
- [5]. S. M. Kay and S. L. Marple JR, "Spectrum Analysis-A modern Perspective," *Proc. of the IEEE* **69**(1981).
- [6]. K. Jeong, J. J. Turek, and D. D. Nolte, "Imaging Motility Contrast in Digital Holography of Tissue Response to Cytoskeletal Anti-cancer Drugs," *Opt. Express* **15**(2007).
- [7]. K. Jeong, J. J. Turek, and D. D. Nolte, "Speckle fluctuation spectroscopy of intracellular motion in living tissue using coherence-domain digital holography," *J. Biomed. Opt.* **15**, 030514 (2010).
- [8]. D. D. Nolte, R. An, J. Turek, and K. Jeong, "Holographic tissue dynamics spectroscopy," *J Biomed Opt* **16**, 087004 (2011).
- [9]. N. Dudovich, D. Oron, and Y. Silberberg, "Single-pulse coherently controlled nonlinear Raman spectroscopy and microscopy," *Nature* **418**, 512-514 (2002).
- [10]. E. P. Ippen and C. V. Shank, "Dynamic spectroscopy and subpicosecond pulse compression," *Applied Physics Letters* **27**, 488-490 (1975).
- [11]. V. T. Jordanov and G. F. Knoll, "Digital synthesis of pulse shapes in real time for high resolution radiation spectroscopy," *Nucl. Instr. and Meth. in Phys. Res. A* **345**, 347 (1994).
- [12]. D. Pestov, R. K. Murawski, G. O. Ariunbold, X. Wang, M. Zhi, A. V. Sokolov, V. A. Sautenkov, Y. V. Rostovtsev, A. Dogariu, Y. Huang, and M. O. Scully, "Optimizing the laser-pulse configuration for coherent Raman spectroscopy," *Science* **316**, 265-268 (2007).

- [13]. T. Ozawa, M. Kaneko, A. Horii, H. Ueno, S. Takehana, H. Sangu, I. Hirao, H. Mizuno, T. Kawai, H. Hibino, H. Adachi, H. Takizawa, T. Uesugi, M. Ohno, H. Aoki, J. Hiroya, K. Imaizumi, E. Yasuda, Y. Oaki, and Y. K., "Optical Imaging apparatus which radiates a low coherence light beam onto a test object, receives optical information from light scattered by the object and constructs therefrom a cross-sectional image of the object," United State Patent.
- [14]. S. C. Hyde, N. P. Barry, R. Jones, J. C. Dainty, and P. M. French, "Sub-100- μ m depth-resolved holographic imaging through scattering media in the near infrared," *Opt Lett* **20**, 2330 (1995).
- [15]. D. Huang, E. A. Swanson, C. P. Lin, J. S. Schuman, W. G. Stinson, W. Chang, M. R. Hee, T. Flotte, K. Gregory, C. A. Puliafito, and et al., "Optical coherence tomography," *Science* **254**, 1178-1181 (1991).
- [16]. S. Seebacher, W. Osten, T. Baumbach, and W. Jüptner, "The determination of material parameters of microcomponents using digital holography," *Optics and Lasers in Engineering* **36**, 103-126 (2001).
- [17]. Z. Li, H. Sun, J. Turek, S. Jalal, M. Childress, and D. D. Nolte, "Doppler fluctuation spectroscopy of intracellular dynamics in living tissue," *J Opt Soc Am A Opt Image Sci Vis* **36**, 665-677 (2019).
- [18]. R. Loudon, *The quantum theory of light*, 3rd ed., Oxford science publications (Oxford University Press, Oxford ; New York, 2000), pp. ix, 438 pages.
- [19]. H. Choi, Z. Li, H. Sun, D. Merrill, J. Turek, M. Childress, and D. Nolte, "Biodynamic digital holography of chemoresistance in a pre-clinical trial of canine B-cell lymphoma," *Biomed Opt Express* **9**, 2214-2228 (2018).

CHAPTER 2. PRECLINICAL TRIAL ON CANINE LYMPHOMA CANCER AND CHOP THERAPY

One of the applications for BDI is phenotypic drug-response measurements on living biopsies taken from cancer patients during the diagnostic phase of their prognostic assessment. The drug response of the biopsies (measured by BDI) to various chemotherapeutic agents show consistent behavior. With a low sample-by-sample variation, a preclinical phenotype measurement by BDI can estimate the efficacy of the chemotherapeutic treatments. Predicting chemotherapy sensitivity becomes an important task to improve patients' quality of life and prescribe a personalized drug combination [1]. Chemosensitivity tests that rely on two-dimensional cell culture derived from cancer patient biopsies have not achieved significant improvement in the selection of chemotherapy. The two-dimensional assay format loses the important three-dimensional tumor microenvironment that controls many aspects of drug distribution and efficacy [2-5]. Alternatively, tests that rely on xenograft growth in PDX models are time-consuming and expensive [6], and the PDX models produce non-native host microenvironments and possible phenotypic outgrowth that does not represent the personal biology of the cancer patient. Therefore, there is a pressing need to develop a rapid, inexpensive test of the efficacy of chemotherapy, applied to *ex vivo* biopsies, that can inform doctors about patient resistance to standard-of-care treatments.

2.1 Introduction to Preclinical Trial for Chemotherapy Efficacy Assessment

Patient resistance to chemotherapy is a major problem for cancer treatment. Although there is standard-of-care for specific cancers, it has been statistically shown that only about 40% of patients experience remission (averaged across all cancers and treatments). Assays for the selection of effective drugs have relied on 2D cell culture from patients, but it has not shown a significant improvement over standard-of-care [1]. One reason may be that 2D cell culture often loses the 3-dimensional characteristics and local microenvironment of the sample [2-5]. Non-Hodgkin lymphomas (NHL) in dogs have histopathologic, molecular, and clinical features similar to NHL in humans [7]. Doxorubicin-based combination chemotherapy is the standard of care for dogs with NHL with the goal to provide durable cancer remission and long-term disease palliation while preserving the quality of life, rather than to cure cancer. Clinical endpoints can be assessed rapidly

in dogs with NHL. Objective response to chemotherapy appears within days following treatment, and the progression-free survival time (PFST) after chemotherapy is approximately 4–9 months [8]. Spontaneous NHL in dogs is biologically and clinically diverse, with a response to chemotherapy varying dramatically from dog to dog. The heterogeneity in response to therapy makes NHL in dogs an appropriate model for comparative oncology in which to study the canine analog of the human disease. Despite this heterogeneity, *ex vivo* biodynamic imaging (BDI) has shown great promise as a means to discriminate NHL in dogs that will respond favorably or unfavorably to chemotherapy. For instance, Custead et al. [9] reported that *ex vivo* BDI on canine B-cell lymphoma predicted sensitivity to single-agent doxorubicin chemotherapy with high accuracy. A preclinical trial was performed which directly tested chemotherapeutic-agent responsiveness by measuring the dynamics of patients' biopsies. The preclinical trial included 19 enrolled canine patients with Non-Hodgkin lymphomas (NHL). Biopsies were collected at the Purdue college of veterinary medicine. For each patient, 32 biopsy-cells were prepared and standard-of-care drugs were applied. BDI measured the drug response phenotypes and were analyzed by machine-learning software.

The study protocol was approved by the Purdue Animal Care and Use Committee (PACUC), and written informed consent was obtained from each dog's owner before enrollment. All dogs underwent surgical lymph node biopsy at the time of enrollment. A portion of each dog's lymph node biopsy was submitted for histopathologic confirmation of disease, while the residual portion was reserved for *ex vivo* BDI. Following the biopsy, all dogs were treated with the previously-described 25-week CHOP chemotherapy protocol. CHOP combination therapy consists of doxorubicin, prednisolone, vincristine, and the active metabolite of cyclophosphamide. The therapy is administered as a combination therapy in humans, but as a sequence of monotherapies in dogs. Objective response to chemotherapy was assessed by caliper-based measurement of peripheral lymph nodes, according to previously-described criteria [10]. Dogs that completed their 25-week course of chemotherapy were re-evaluated at the PUVTH once monthly until the time of measurable cancer progression or death due to any cause, whichever came first. Progression-free survival (PFS) time for each dog was defined as the time (in days) from initiation of CHOP chemotherapy to the time that the sum of the longest diameters of up to 5 peripheral lymph nodes was at least 20% greater than its lowest recorded value.

2.2 Chemotherapeutic Agents Phenotypes Measured by Biodynamic Imaging

Harvested biopsies from a preclinical trial patient were dissected into 16 pieces at the college of veterinary medicine in Purdue and immobilized in a 96-well plate by agar. The volume of the well is 350 μL , and 50 μL was filled by a dissected biopsy and an agar immobilization unit. The rest of the volume was filled by RPMI-1640 medium containing penicillin (100 U/ml), streptomycin (0.1 mg/mL), and 25 mM HEPES. For reagents, 0.1 % DMSO was used as a carrier agent, and CHOP chemotherapeutic agents were prepared. When applying chemotherapeutic agents, 150 μL of RPMI-1640 medium was subtracted and prepared drugs were added.

The protocol for biopsy phenotyping by BDI consists of 3 hours of baseline measurements and 7.5 hours of post-dose measurements. For a given patient, 32 sections of a single lymph-node biopsy were measured over two days, and 5-replicate-wells were prepared for each drug. The measurement and data analysis took 12 hours and 4 hours, respectively. Drug phenotypes could be obtained within one day after a biopsy was delivered. A control group of biopsy segments was treated with 0.1% DMSO which is the drug carrier.

2.3 Phenotype Correlation and Similarity Matrices for Machine Learning

The drug-response spectrogram averages are shown in Figure 2.1. These are 2D plots of power spectra normalized by the baseline measurement. Drug-response phenotype spectrograms $D(\omega, t)$ were generated by

$$D(\omega, t) = \log S(\omega, t) - \log S_0(\omega) \quad (2.1)$$

where the baseline S_0 is a 4-baseline average [11]

$$S_0(\omega) = \frac{1}{4} \sum_{t=1}^4 S(\omega, t) \quad (2.2)$$

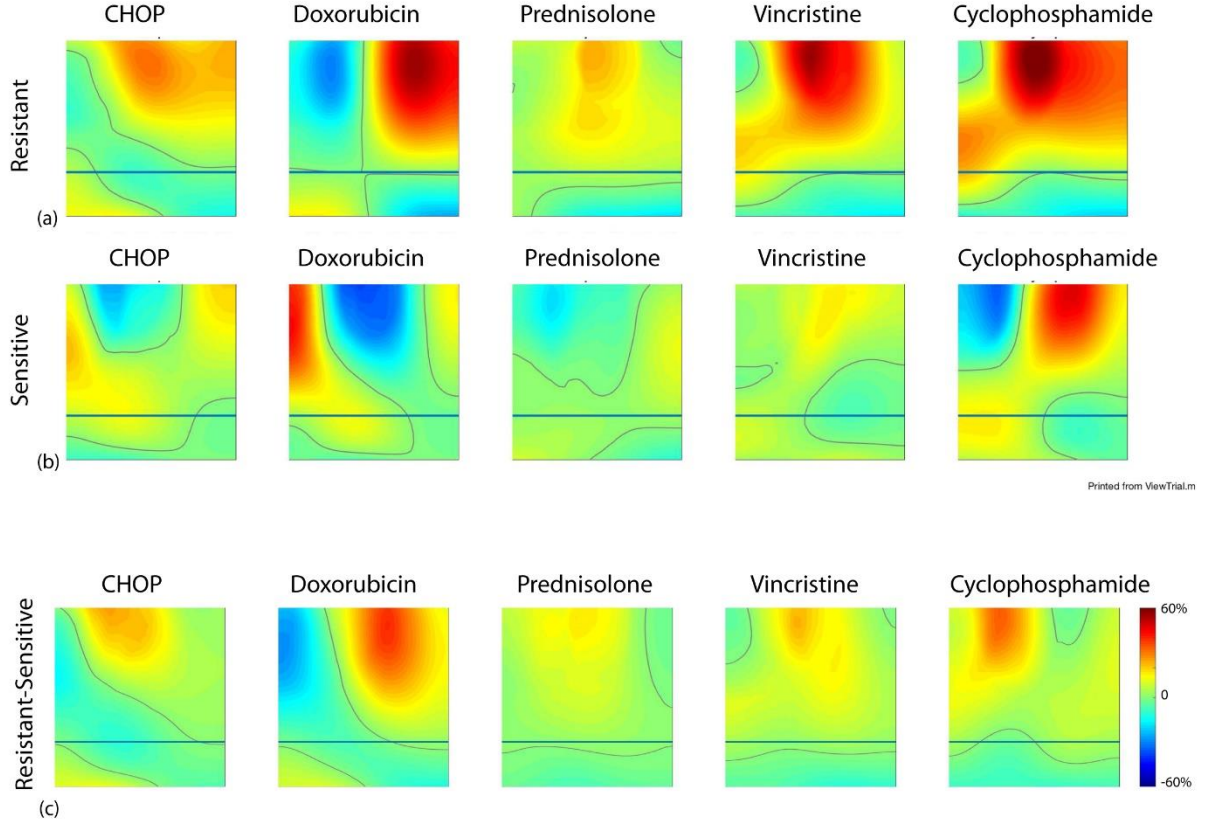


Figure 2.1 Spectrograms of various drug-response phenotypes. (a) Drug-resistant spectrograms and (b) sensitive spectrograms. (c) Spectrogram difference between resistant and sensitive groups. Prednisolone showed a minimal phenotypic difference, and Doxorubicin showed the most significant phenotypic difference [12].

The averaged power spectrograms show the phenotypes of the corresponding drugs. The spectrograms were converted into feature values using coefficients P_n of Legendre polynomials

$$P_n(t) = \frac{2n+1}{2} \int_{-1}^1 D(\omega, t) P_n(\omega) d\omega \quad (2.3)$$

The set of coefficients form a multi-dimensional vector \mathbf{v} , and each spectrogram can be represented by this feature vector, where each vector component is called a biomarker [11-14]. Feature vectors are multi-dimensional vectors and their correlations were obtained by taking direction cosines. Similarity matrix elements A_{ij} are direction cosine of feature vectors of i th and j th patients \mathbf{v}_i and \mathbf{v}_j obtained as

$$A_{ij} = \cos \theta_{ij} = \frac{\mathbf{v}_i \cdot \mathbf{v}_j}{|\mathbf{v}_i| |\mathbf{v}_j|} \quad (2.4)$$

The direction cosine value becomes positive unity or negative unity in cases of perfect correlation and anti-correlation, respectively. A similarity matrix in Figure 2.2(b) displays the direction cosine cross-correlation between all feature vectors.

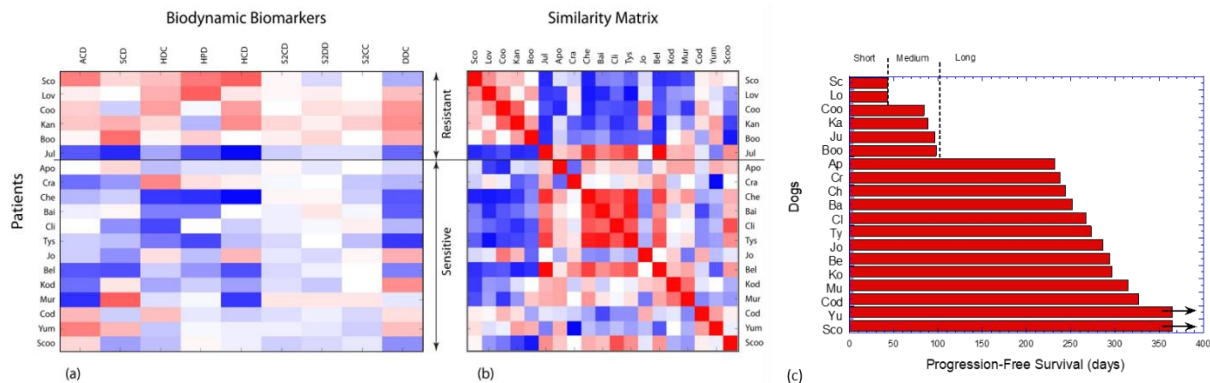


Figure 2.2 (a) Feature vectors of patients and (b) similarity matrix. (c) Progression-free survival time (PFS) [12].

The degree of correlation of the similarity matrix with clinical outcome can be used to predict which phenotype is drug resistant or sensitive by applying machine learning to analyze the feature vectors and classify their phenotypes. The linear separability of resistive and sensitive groups by an N-dimensional hyperplane was estimated using a neural perceptron algorithm [15, 16]. A perceptron is the simplest possible neural net with a single neuron having multiple inputs (the values of the feature vector) and a single output (clinical outcome). The optimization process finds the neural weights of the inputs and the bias of the neuron that minimizes a cost function. The neuron sigmoidal response function is a hyperbolic tangent (\tanh) that saturates to ± 1 for large positive/negative arguments that are compared to the ± 1 classification based on the PFS. The cost function uses a chi-squared error and a regularization cost. The regularization cost measures the mean squared distance from the mean hyperplane that is defined as the bisector of the vector between the center of mass of each class of points. Regularization is required when finding hyperplanes to keep the hyperplane parameters from drifting to large values during optimization. The regularization factor in our analysis was chosen to be 10%, which is a commonly-used rule-of-thumb. The perceptron is trained using gradient descent on the cost function. The linear separability analysis of the canine B-cell lymphoma trial agreed with objective clinical outcome (progression-free survival) with 84% accuracy [12].

An alternative linear separation method to cross-validate the perceptron machine-learning process was done by log-likelihood (LL) estimation [15]

$$LL = \sum_a \log \frac{1 + P_R(v_a)}{1 + P_S(v_a)} \quad (2.5)$$

where the sum is over all selected biomarkers for a given patient and P_R and P_S are the probability density function of resistive and sensitive groups according to their clinical outcomes. A comparison on the perceptron and LL is shown in Figure 2.3. The classifier results were obtained through training a simple neural perceptron. The perceptron was trained using the hold-out procedure in which 18 of the dogs were used for training and the 19th dog was classified, and then repeating the hold-out procedure 19 times (once per dog). The perceptron identified the best linear separability of the point cloud in the feature space separating the sensitive from the resistant patients. All but three patients (Cli, Jo and Jul) were correctly classified for the majority of the training runs using gradient descent for cost-function minimization. Three additional patients were marginal (Yum, Cod and Bai). The patient Jul showed very strong biodynamic signatures of therapy sensitivity, yet had a medium PFS time similar to Boo and should have been classified as resistant. On the other hand, no distinct clinical observations could be highlighted for the other two misclassified patients and the three marginal cases. It is important to point out that the biodynamic assay measures the response of biopsy tissues *ex vivo* and disconnected to the immune system of the patient, while the ability to sustain remission depends on an individual's immune system. Measures of endogenous anti-tumor immunity in lymphoma patients correlates with survival, and it is becoming clear that the immune system is probably a major factor keeping a cancer in remission once that remission has been produced by the chemotherapy.

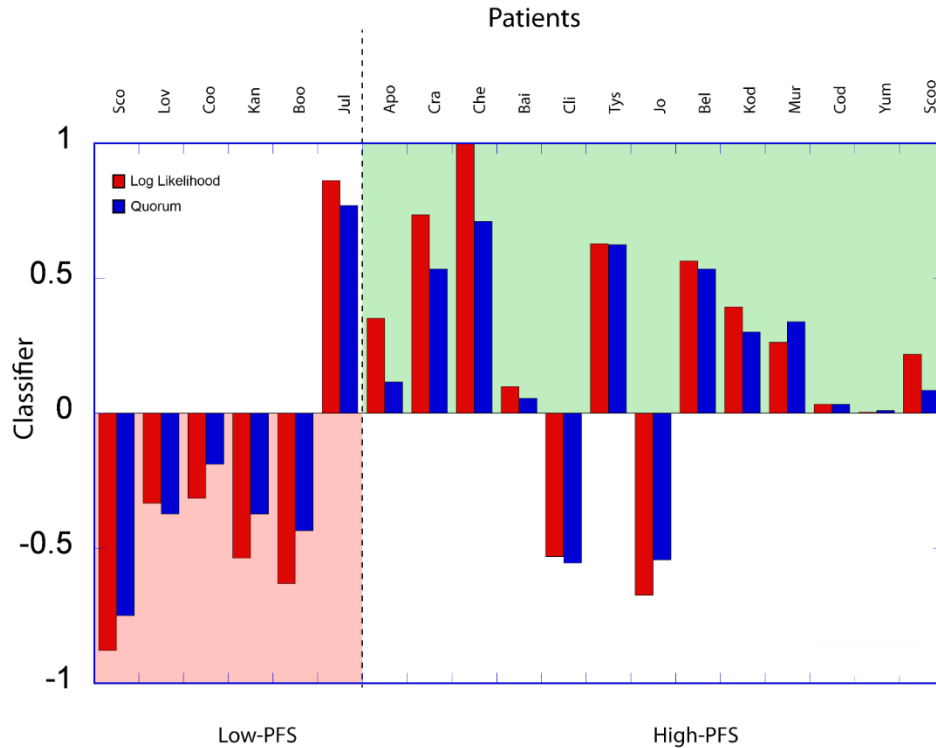


Figure 2.3 Comparison of log-likelihood and perceptron quorum. Two linear separabilities in N-dimensional space showed 84 % accuracy according to patient PFS [12].

Network similarities were obtained and are visualized in Figure 2.4. The similarity network showed 3 miss-classified cases (1 false-negative and two false positives). The direction cosine is independent of the overall magnitude of the feature vector while capturing the similarities in the patterns of feature values. The resulting similarity matrix is converted into a similarity network by selecting a threshold that converts the similarity matrix into an adjacency matrix for the network. The key result of the similarity network analysis is the segregation of the long-PFS and short-PFS patients into two relatively distinct sub-clusters.

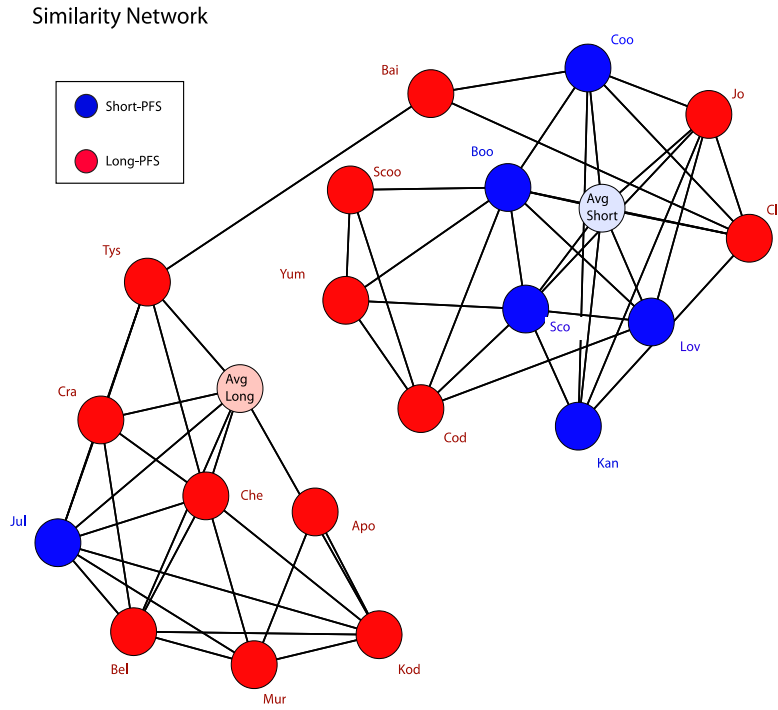


Figure 2.4 Similarity network between canine patients. Red nodes and blue nodes represent short-PFS and long-PFS respectively. The separation between short-PFS and long-PFS showed 84% accuracy with one false-negative and two false-positives [12].

2.4 Discussion

This chapter described the application of biodynamic digital holography to assess the response of *ex vivo* living biopsies to a standard-of-care combination therapy (CHOP) that is prescribed for both human and canine patients with non-Hodgkin’s B-cell lymphoma. In the *ex vivo* testing, separate biopsy samples were exposed to physiologically-relevant doses of each of the single-agent therapies (doxorubicin, cyclophosphamide, prednisolone, and vincristine) as well as the combination therapy. By testing the single-agent therapies, the drug-response biodynamic signatures of each agent (having distinct mechanisms of action) are isolated, allowing the individual responses to be assessed in addition to the response to the combination therapy. The mean-subtracted and normalized biomarkers are feature vectors in a high-dimensional feature space representing the response of each of the 19 canine patients to the *ex vivo* treatments. The analysis identifies biodynamic biomarkers, selected from the collection of single-agent and combination therapies, that are most consistent in the classification of patient response to therapy.

Relative similarities among all pairs of patients are calculated using the feature vectors. While there are many ways to define similarity in a multidimensional vector space we found that the direction cosine provides a simple, robust and reproducible measure of similarity among the patient drug-response feature vectors. The direction cosine is independent of the overall magnitude of the feature vector while capturing the similarities in the patterns of feature values. The resulting similarity matrix is converted into a similarity network by selecting a threshold that converts the similarity matrix into an adjacency matrix for the network. The key result of the similarity network analysis is the segregation of the long-PFS and short-PFS patients into two relatively distinct subclusters. The classifier results were obtained through training a simple neural perceptron. The perceptron was trained using the hold-out procedure in which 18 of the dogs were used for training and the 19th dog was classified and then repeating the hold-out procedure 19 times. The perceptron identified the best linear separability of the point cloud in the feature space separating the sensitive from the resistant patients. All but three patients (Cli, Jo and Jul) were correctly classified for the majority of the training runs using gradient descent for cost function minimization. Three additional patients were marginal (Yum, Cod, and Bai). The patient Jul showed very strong biodynamic signatures of therapy sensitivity, yet had a medium PFS time similar to Boo and should have been classified as resistant. In the clinical assessment, Jul was a very large dog and subsequently may have been under-dosed. The selection of individual doses is based on the patient's surface area, which is a procedure that may under-dose large patients. The fact that Jul was an outlier in the patient size distribution may account for its incorrect classification in this trial. On the other hand, no distinct clinical observations could be highlighted for the other two misclassified patients and the three marginal cases. It is important to point out that the biodynamic assay measures the response of biopsy tissues *ex vivo* and disconnected to the immune system of the patient, while the ability to sustain remission depends on an individual's immune system. Furthermore, there may be some physiologic processes within the patients that the biodynamic profile cannot capture, such as drug delivery to the tumor. Finally, tumor heterogeneity as well as biopsy subsampling heterogeneity contributes large variances to the biodynamic measurements with only 3 to 5 replicates for each treatment. The multiple subsamples help to average over the variability, but some patients may still have large variances. Future developments of higher multiplexed assays and stronger histological guidance for subsample dissection may further reduce the effects of sample variance. Producing spectrograms from smaller regions could image this

heterogeneity directly, further improving the spatial selection of the most relevant drug responses. Also, it would be interesting in future work to study whether patients displaying marginal biodynamic response signatures have different genotypes. The biodynamic signatures of drug mechanisms of action are only beginning to be mapped out. The connection between physiological effects of a drug, and especially the personal response, are still largely unknown. Nonetheless, the high accuracy of this preclinical trial and the strong phenotypic differences between sensitive and resistant patient responses provide a significant approach for predicting patient response to therapy. Future development of biodynamic profiling will continue to utilize tool compounds and reference drugs with known mechanisms of action to identify the biodynamic signatures of specific subcellular processes. More extensive use of neural networks in the analysis of biodynamic biomarkers may help in this process as well as in the selection of the biomarkers that carry the most information related to drug sensitivity. An important next step in the analysis, using multilayer neural networks with hidden-layer neurons, is to develop a continuous-valued predictor that can differentiate strong responders from moderate responders, providing a continuous degree of sensitivity to help clinicians make decisions. Future developments of biodynamic profiling will seek to identify which therapies are best matched to individual patients for personalized therapy selection. Additional biodynamic therapy assessment studies are currently underway in human ovarian and breast cancer as well as human esophageal cancer.

2.5 References

- [1]. I. A. Cree, "Chemosensitivity and chemoresistance testing in ovarian cancer," *Curr Opin Obstet Gynecol* **21**, 39-43 (2009).
- [2]. L. G. Griffith and M. A. Swartz, "Capturing complex 3D tissue physiology in vitro," *Nat Rev Mol Cell Biol* **7**, 211-224 (2006).
- [3]. N. T. Elliott and F. Yuan, "A review of three-dimensional in vitro tissue models for drug discovery and transport studies," *J Pharm Sci* **100**, 59-74 (2011).
- [4]. S. Y. Sung, C. L. Hsieh, D. Wu, L. W. Chung, and P. A. Johnstone, "Tumor microenvironment promotes cancer progression, metastasis, and therapeutic resistance," *Curr Probl Cancer* **31**, 36-100 (2007).
- [5]. S. Breslin and L. O'Driscoll, "Three-dimensional cell culture: the missing link in drug discovery," *Drug Discov Today* **18**, 240-249 (2013).

- [6]. E. J. Hartsough and A. E. Aplin, "Of Mice and Melanoma: PDX System for Modeling Personalized Medicine," *Clin Cancer Res* **22**, 1550-1552 (2016).
- [7]. D. Ito, A. M. Frantz, and J. F. Modiano, "Canine lymphoma as a comparative model for human non-Hodgkin lymphoma: recent progress and applications," *Veterinary Immunology and Immunopathology* **159**, 192-201 (2014).
- [8]. L. D. Garrett, D. H. Thamm, R. Chun, R. Dudley, and D. M. Vail, "Evaluation of a 6-month chemotherapy protocol with no maintenance therapy for dogs with lymphoma," *J Vet Intern Med* **16**, 704-709 (2002).
- [9]. M. R. Custead, R. An, J. J. Turek, G. E. Moore, D. D. Nolte, and M. O. Childress, "Predictive value of ex vivo biodynamic imaging in determining response to chemotherapy in dogs with spontaneous non-Hodgkin's lymphomas: a preliminary study," *Converg Sci Phys Oncol* **1**(2015).
- [10]. D. M. Vail, G. M. Michels, C. Khanna, K. A. Selting, C. A. London, and G. Veterinary Cooperative Oncology, "Response evaluation criteria for peripheral nodal lymphoma in dogs (v1.0)--a Veterinary Cooperative Oncology Group (VCOG) consensus document," *Vet Comp Oncol* **8**, 28-37 (2010).
- [11]. D. D. Nolte, R. An, J. Turek, and K. Jeong, "Tissue dynamics spectroscopy for phenotypic profiling of drug effects in three-dimensional culture," *Biomed Opt Express* **3**, 2825-2841 (2012).
- [12]. H. Choi, Z. Li, H. Sun, D. Merrill, J. Turek, M. Childress, and D. Nolte, "Biodynamic digital holography of chemoresistance in a pre-clinical trial of canine B-cell lymphoma," *Biomed Opt Express* **9**, 2214-2228 (2018).
- [13]. D. Merrill, R. An, H. Sun, B. Yakubov, D. Matei, J. Turek, and D. Nolte, "Intracellular Doppler Signatures of Platinum Sensitivity Captured by Biodynamic Profiling in Ovarian Xenografts," *Sci Rep* **6**, 18821 (2016).
- [14]. D. Merrill, R. An, J. Turek, and D. D. Nolte, "Digital holography of intracellular dynamics to probe tissue physiology," *Appl Opt* **54**, A89-97 (2015).
- [15]. J. Watt, R. Borhani, and A. K. Katsaggelos, *Machine learning refined : foundations, algorithms, and applications* (2016).
- [16]. C. L. Gardel and J. J. Mekalanos, "Alterations in *Vibrio cholerae* motility phenotypes correlate with changes in virulence factor expression," *Infect Immun* **64**, 2246-2255 (1996).

CHAPTER 3. BIODYNAMIC IMAGING OF BACTERIAL SWARMS

3.1 Environmental Rapid Change Induced Migration

Bacteria are among the simplest lifeforms on Earth. Their biological features are well known and deeply studied. However, physical aspects such as swarming or chemotaxis mechanisms are still under investigation. Swarming motion and long-distance bacteria interaction by chemical signaling show cellular communication. As bacteria are the most primitive lifeform, understanding the biophysical characteristics of bacterial collective motion would provide a preliminary understanding of the random process of homogeneous individuals. To establish statistics of swarms, it is necessary to collect dynamic information of swarms beyond the order of the microbiome's cell size. Frequently-used methods to measure bacterial motility are soft agar assay and optical imaging [1-4]. The soft agar assay requires many cell cycles to measure a meaningful colony diameter to estimate bacterial motility, which limits real-time and high throughput measurements. Also, dynamic characteristics vary over time. Optical imaging methods [1-3, 5-8] have a limited field of view (FOV), and data acquisition of bacterial motility is localized. The advantages of BDI compared to conventional motility measurements are: i) the coherence-gate and the large beam diameter enable the collection of signals from a large number of the specimen (several millions of bacteria), ii) quasi-real-time measurement using a short data acquisition time, and iii) controlling the chemical composition of the medium during measurement. The measurements conducted by BDI in this chapter tested nutrient-shock and anti-biotic-driven motility within a high-cell-density bacterial pellet. The following chapter explores bacterial infecting living tissue.

Bacteria strains used for the experiments are motile bacteria. Their flagella induce swimming and tumbling motions and bacteria can freely migrate by changing the frequencies of the motions. The dynamics of bacteria at free space and swarm have distinct characteristics. Using dynamic light scattering is one of the effective ways to study the dynamics of a huge number of bacteria. BDI has a beam diameter illuminating a sample is about 400 μm , which covers the area about 0.5 mm^2 , and assuming bacteria are packed in the scanning volume (beam diameter times the coherence-

gating depth (20 μm)), then the signal collected at the FP is from about 20 millions of bacteria. To make a packed structure of bacteria, the bacteria medium was centrifuged.

The different strain has different characteristics. *Escherichia coli* (*E. coli*), *Salmonella enterica* (*S. enterica*) *Listeria monocytogenes* (*L. monocytogenes*) *Listeria innocua* (*L. innocua*) are foodborne pathogens and commonly found in daily lives. Their physical dimensions and microscopic images are shown in Figure 3.1. Bacteria were cultured in an LB medium (1% tryptone, 0.5% bacto yeast extract, 0.1% glucose, and 1.5% bacto agar) [9] for 24 hours at 37 degrees Celsius to reach 10^8 CFU/ml concentration. During cell culture, test tubes were shaken with 90 rpm. *L. innocua* have a slow reproduction rate, so cells were cultured for 48 hours.

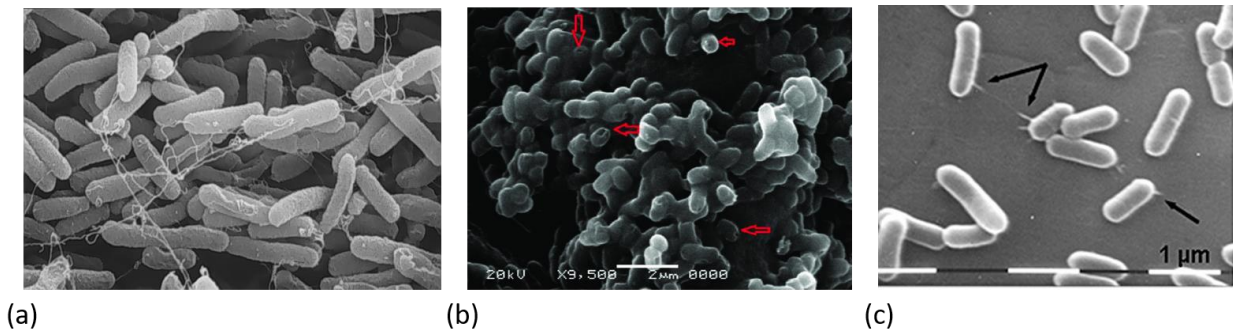


Figure 3.1 SEM pictures of (a) *E. coli* [10] (b) *S. enterica* [11] and (c) *L. monocytogenes* [12]. The dynamic and physical characteristics are shown in the table below.

Table 3.1 Bacterial strains and corresponding physical characteristics

Strain	<i>E. coli</i>	<i>L. monocytogenes</i>	<i>S. enterica</i>
Speed ($\mu\text{m/s}$)	20 ^[13]	6 ^[14]	20 ^[15]
Width (μm)	0.25 ^[16]	0.7~1.5 ^[17]	0.4~0.5 ^[18]
Length (μm)	1~2	2.0~5.0	1~2

Table 3.2 Bacterial strain information

Strain	<i>E. coli</i>	<i>L. monocytogenes</i>	<i>L. innocua</i>	<i>S. enterica</i>
ID#	43894	104035S		Phage Type 21

3.2 Nutrient and Osmolarity Shock on Bacteria Pellets

To measure the 3D dynamics of bacteria, a bacterial pellet is formed by centrifuging a bacterial medium (10^8 CFU/mL). The centrifuging process increases the density of bacteria (10^{10} CFU/mL) and forms an opaque viscous material. The cellular packing of a bacterial pellet is easily disrupted by various external stimuli such as mechanical perturbations, nutrients, osmotic pressure, or antibiotics. The bacteria in steady-state are relatively quiescent in terms of speckle motility but external stimuli produce bacterial dynamics within a pellet. To measure bacterial dynamics within a pellet, 20 μ L of the pellet was prepared at the bottom of a 96-well plate and carefully dipped in 300 μ L of 1% NaCl medium. To establish bacteria in the steady-state, measurements were conducted after 5 hours of resting time. After 5 hours, 3 baselines were measured and half of the medium (150 μ L) was subtracted. Then the well was filled by double-concentration LB medium (2% tryptone, 1% bacto yeast extract, 0.2% glucose, and 3% bacto agar) after measuring baselines, so the medium inside of the well has the standard LB medium chemical component concentration. The wells were held at 36 degrees Celsius, which is an optimized temperature for bacteria. An experiment consisted of 3 baselines and 13 post-dose measurements. Each measurement took approximately 2 minutes, and 2058 frames were recorded including 10 background frames. To investigate the nutrient shock effect, 150 μ L of the LB medium was added. The pipetting perturbation effect was tested by subtracting and adding the same medium from the well (old medium). The effect of adding a fresh medium without nutrient was examined by refreshing half of the medium volume.

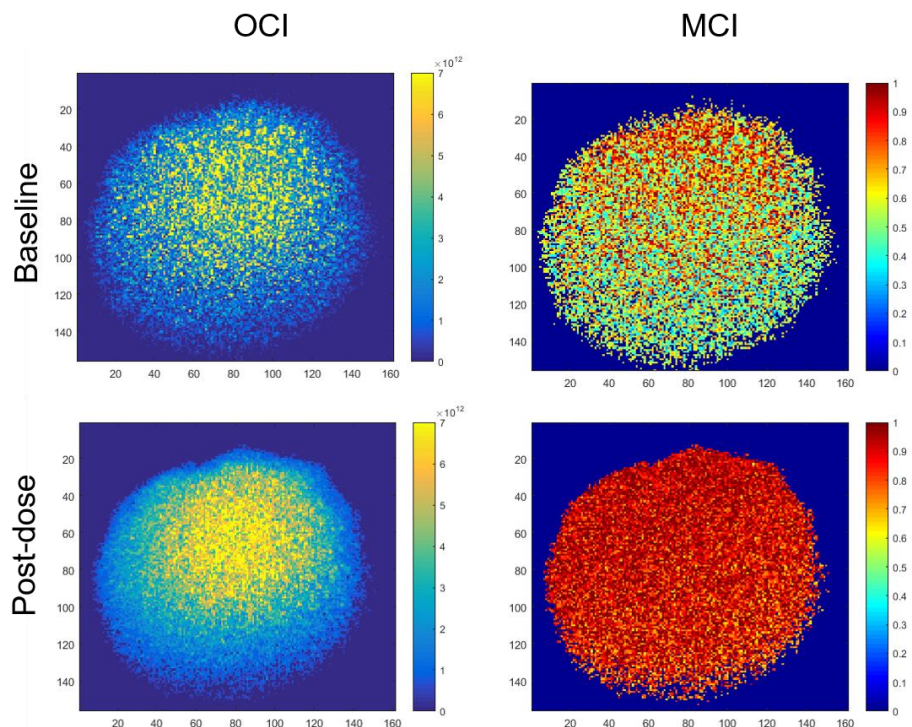


Figure 3.2 OCI and MCI image of *E. coli* pellet. LB medium was applied to induce a motility response. Post-dose OCI and MCI were measured immediately after applying the lysogeny-broth (LB) medium. MCI enhancement at post-dose is prominent when compared to baseline MCI.

The backscatter brightness (BSB) and the NSD are shown in Figure 3.3 for *E. coli*, *S. enterica*, and *L. monocytogenes* pellets. The three curves are measurements of responses after applying the old medium (subtracted from a well containing a bacteria pellet), 1% NaCl and the LB medium, respectively. When the LB medium was applied, a prominent increment in BSB was observed, while the wells with other reagents did not show observable changes. The BSB increases within 6 minutes and remained at the same level. The motility shows an immediate increase after applying the LB medium and decreases slowly over 10 minutes. The final motility value becomes lower than the initial NSD for *E. coli* but remains higher in the cases of *L. monocytogenes* and *S. enterica*.

An increase in BSB may be caused by increased optical heterogeneity in the pellet. The fact that it stabilizes at a higher value than the starting value in all three bacteria cases suggests that there is a permanent (over at least 20 minutes which is comparable to a cell cycle) change in the physical property of the pellet, or dynamics of the individual bacterial cells, stimulated by the LB medium.

The immediate increase in the motility is probably caused by chemotaxis, but the later decrease could be caused by increased BSB (NSD is normalized by BSB).

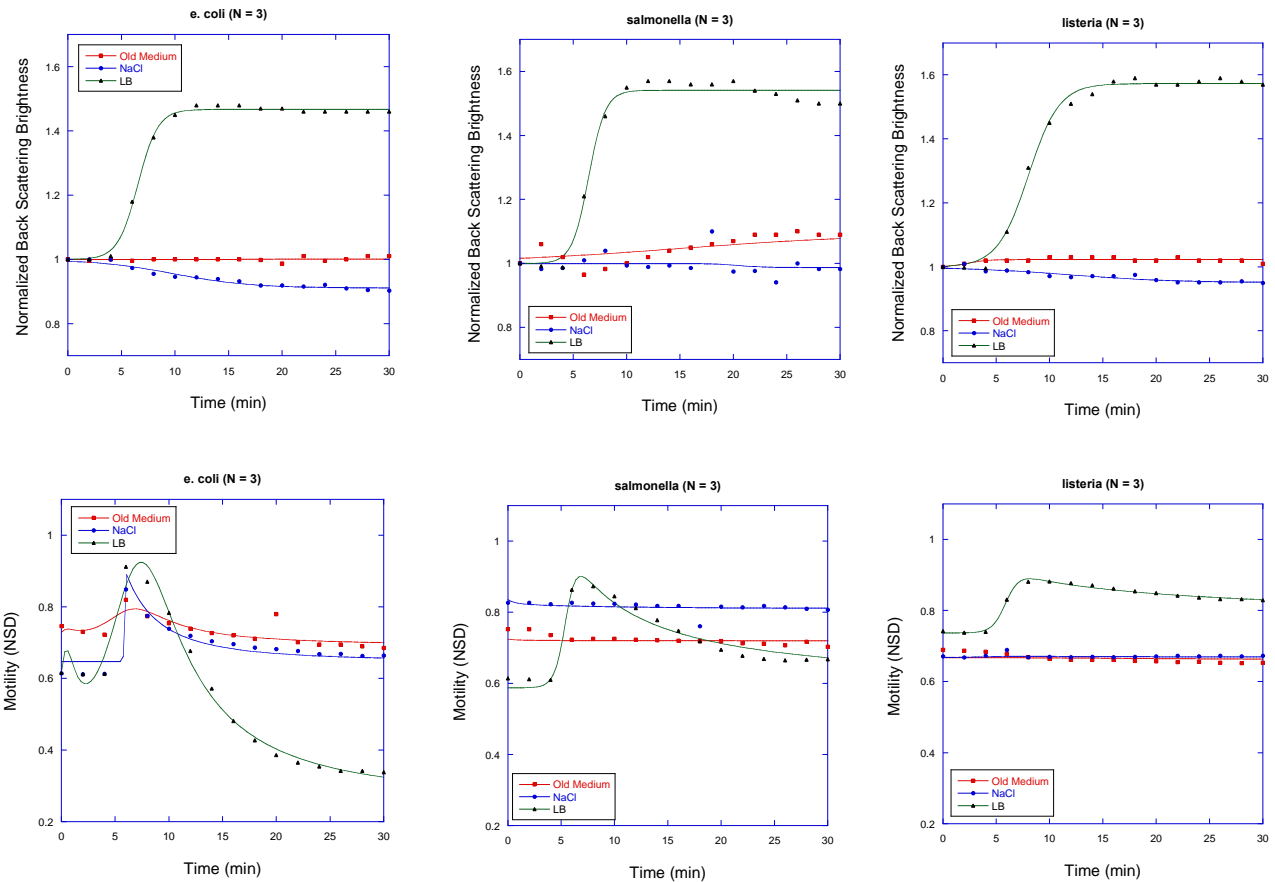


Figure 3.3 Temporal responses of BSB and NSD for *Escherichia coli* (*E. coli*), *Salmonella enterica* (*S. enterica*), and *Listeria monocytogenes* (*L. monocytogenes*) pellets after applying various reagents. The three curves represent the temporal responses of the old medium, 1% NaCl and the LB medium, respectively. All data points are 3-replicate averages.

3.3 Doppler Spectroscopy of Bacterial Pellets

To study dynamics induced by chemotaxis, the power spectral density was analyzed which is called tissue dynamics spectroscopy (TDS) [19]. Previously, TDS studied chemotherapeutic response phenotypes of biopsies, xenografts and standard cancer cell lines. Applying the same approach to the bacterial pellets, 3D dynamics that occurred after applying the LB medium can be investigated by TDS. It is known that motile bacteria have flagella and gain propulsion force by manipulating flagella. To compare the dynamics of bacteria in the stationary state or dynamic state, extracted pellet rested in 1% NaCl medium for 5 hours to ensure the bacteria in pellets are in the

stationary state. 3 baselines were measured (Figure 3.3) and the LB medium was applied to induce chemotaxis. The baseline spectra for *E. coli*, *S. enterica*, and *L. monocytogenes* are shown in Figure 3.4. The frequency span is from 0.01 Hz to 10 Hz which corresponds to the approximate speed of 3 nm/s to 3 μ m/s. The baseline spectra show 1/f spectral density which represents the Doppler signal produced by 3D random diffusive dynamics [20].

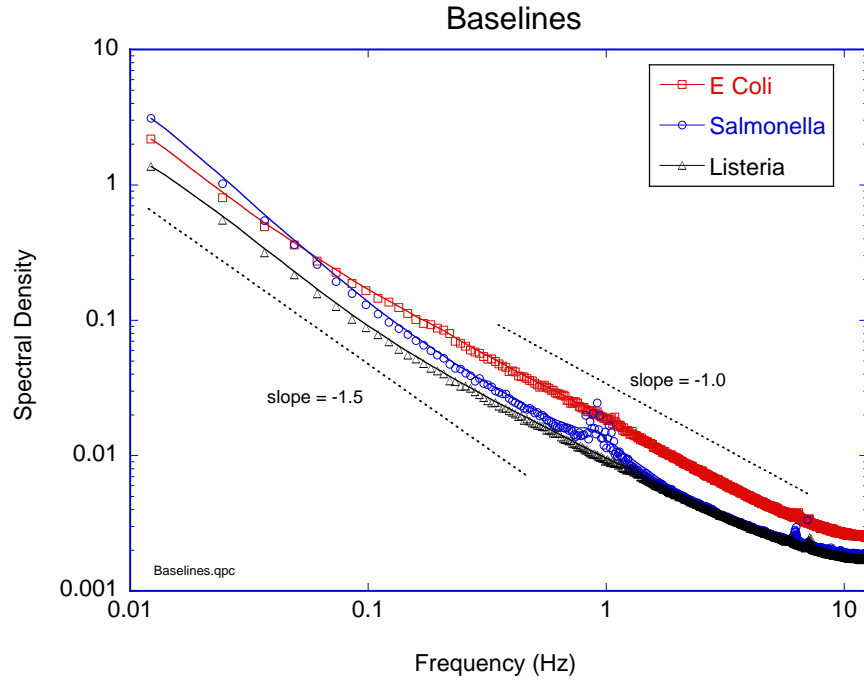


Figure 3.4 Baseline spectra of *E. coli*, *S. enterica*, and *L. monocytogenes*. The spectra in all three samples show with 1/f-like spectral density. The expected bacterial dynamics of the spectral densities are 3D isotropic motion [20].

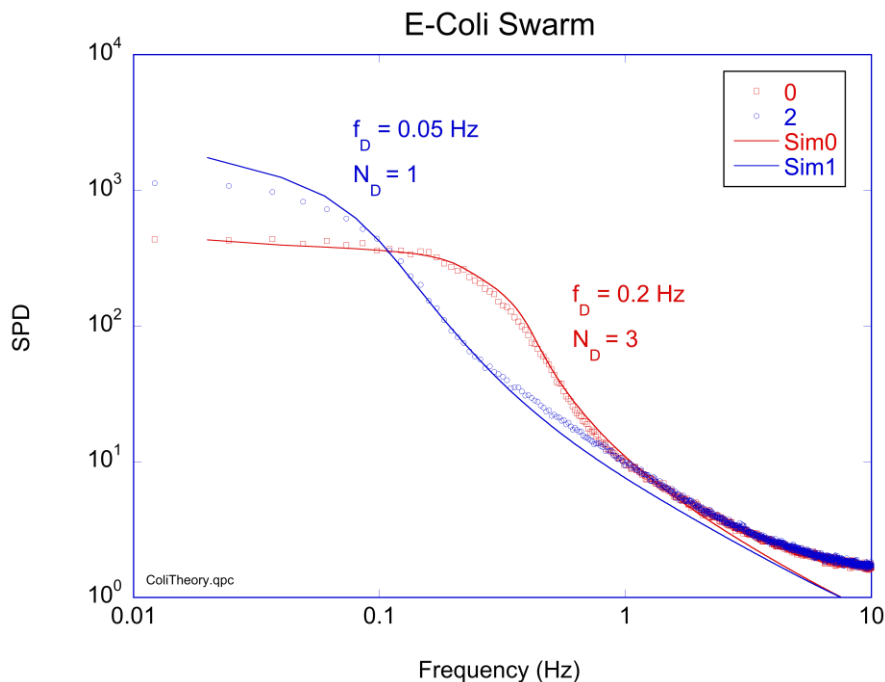


Figure 3.5 Example of a Doppler-edge fit to the bacterial pellet response to a nutrient shock. The average edge frequency and Doppler number are shown for two times: one immediately after the nutrient application, and another 2 minutes later, showing a rapid relaxation back towards the $1/f$ spectrum.

The response of an *E. coli* pellet to a nutrient shock is shown in Figure 3.5. Immediate spectral enhancement occurred after the LB medium was applied. The shape of the spectral enhancement is called a Doppler edge. From the Doppler edge, the average speed and the characteristic time can be estimated by obtaining the maximum spectral enhancement. The Doppler edge's maximum spectral enhancement occurs at the inverse of the characteristic time τ_c [20],

$$\frac{1}{\tau_c} = \mathbf{q} \cdot \mathbf{v} \quad (3.1)$$

where \mathbf{q} and \mathbf{v} are the wavevector and scattering element's velocity respectively. The immediate responses of Doppler edges are shown in Figure 3.6(a) for several bacterial strains. The maximum spectral density enhancement occurred at 0.2 Hz for *E. coli* (corresponding to the average speed of about 100 nm/s). The Doppler spectral density shows a clear hump after applying the LB medium and estimated Doppler numbers are about $ND = 3$. This Doppler signal represents about 100 nm/s average swarming speed produced by the LB medium. Within 2 minutes after applying the LB medium, the Doppler edge shifted to 0.05 Hz with a lower-bound Doppler number of 1. This rapid relaxation process is consistent with the rapid relaxation of NSD shown in Figure 3.2.

E. coli showed the strongest spectral response. *S. enterica* showed a moderate enhancement and *L. monocytogenes* showed the weakest enhancement. The spectral enhancement comparison is shown in Figure 3.5 (b) by normalizing the enhanced spectral density by the average baseline spectral density. All bacteria showed spectral enhancements and prominent Doppler edges after applying the LB medium.

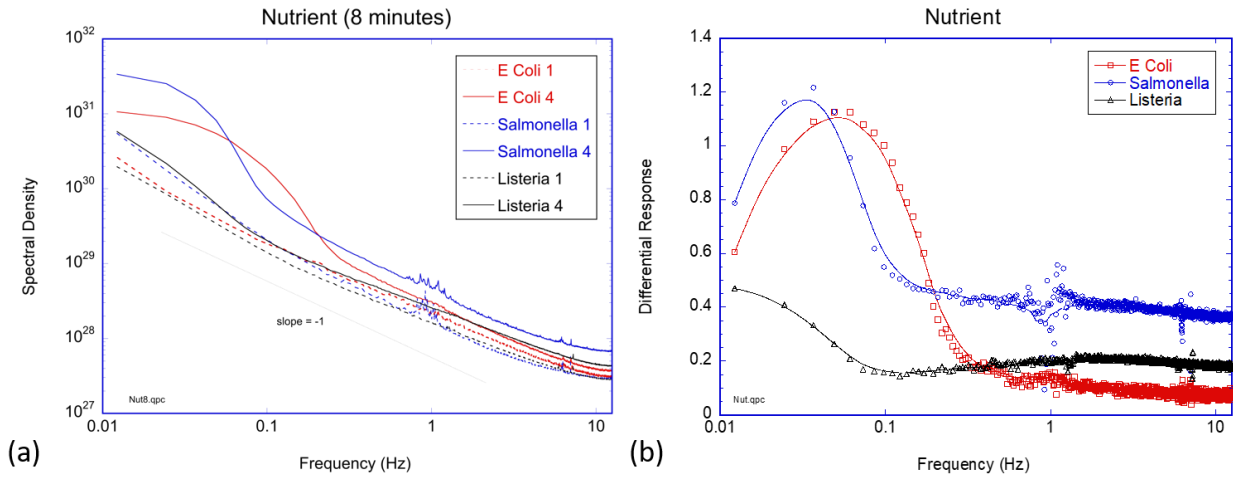


Figure 3.6 (a) Doppler edges produced by applying the LB medium. (b) Relative spectral enhancements of *E. coli*, *S. enterica*, and *L. monocytogenes* pellets are demonstrated. The responses occurred immediately after applying the LB medium.

The temporal responses of spectral density can be visualized in a 2D spectrogram by using Eq. (2.1). The nutrient shock spectrograms of various bacterial strains are shown in Figure 3.7. The background suppression that occurred in the *E. coli* response was caused by the enhanced BSB enhancement shown in Figure 3.2.

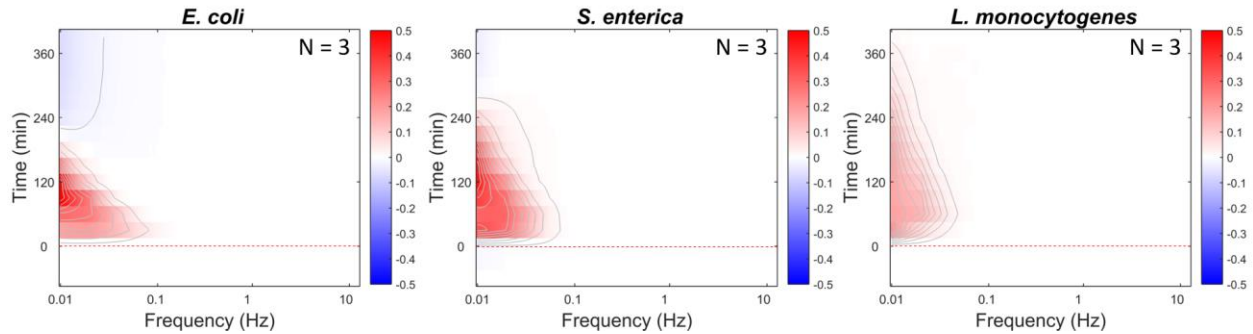


Figure 3.7 Nutrient shock-responses of *E. coli*, *S. enterica*, and *L. monocytogenes* pellets. Dramatic low-frequency enhancement occurred (the Doppler edge). The nutrient shock showed the strongest response in *E. coli*. Spectra were normalized by the baselines averages. (Intensity normalization)

The measured average speed of 100 nm/s is much slower than the free-swimming speed of *E. coli* that is about 30 microns per second. The speeds of bacteria in pellets may be suppressed by the dense structure of the pellets. Detailed pictures of bacterial motions will be demonstrated in CHAPTER 5 on phase-sensitive detection.

3.4 Tissue Dynamics Spectroscopy (TDS) of Antibiotic Responses

Testing antibiotic efficacy is one possible application of BDI. The indiscriminate use of antibiotics has caused the rise of antibiotic-resistant bacteria. Rapid detection of antibiotic-resistant bacteria and selecting sensitive antibiotics is an important task, and the bacterial motion measured by BDI may demonstrate a sensitive or resistant response of bacteria when various antibiotics are applied. An example of inhibition of *E. coli* dynamics by ethanol is shown in Figure 3.8. The spectral densities of mid and low frequency are inhibited by approximately 60%, while the highest frequency is relatively unaffected. The response of *E. coli* to NaOH and bleach are shown in Figure 3.9. The responses of ethanol and bleach are similar, while NaOH shows broad inhibition of activity (broad-frequency cell death).

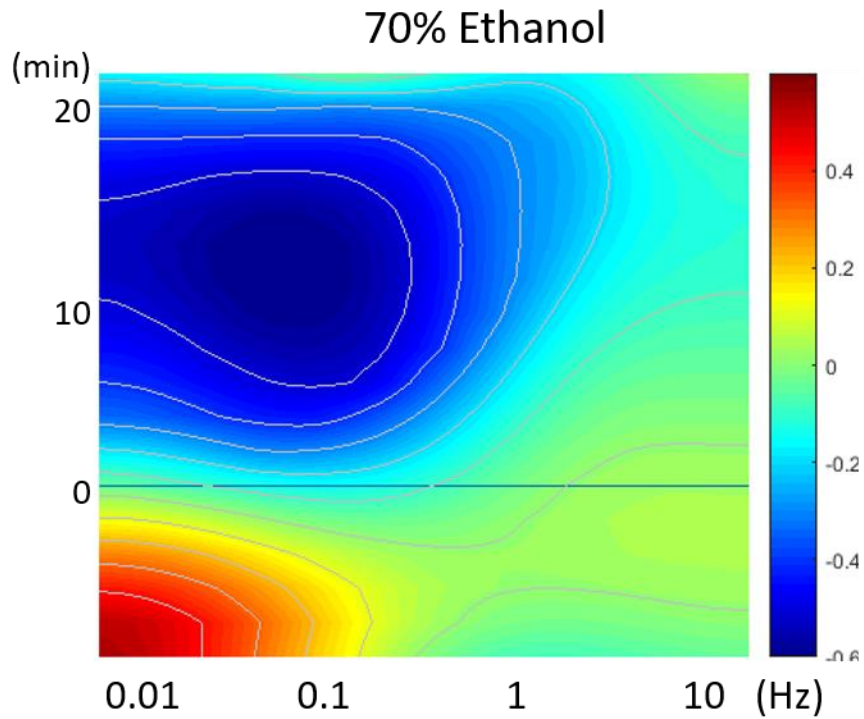


Figure 3.8 Response of *E. coli* pellets to ethanol (70 %). The response is inhibitory with strong 60% suppression in the mid and lower frequencies.

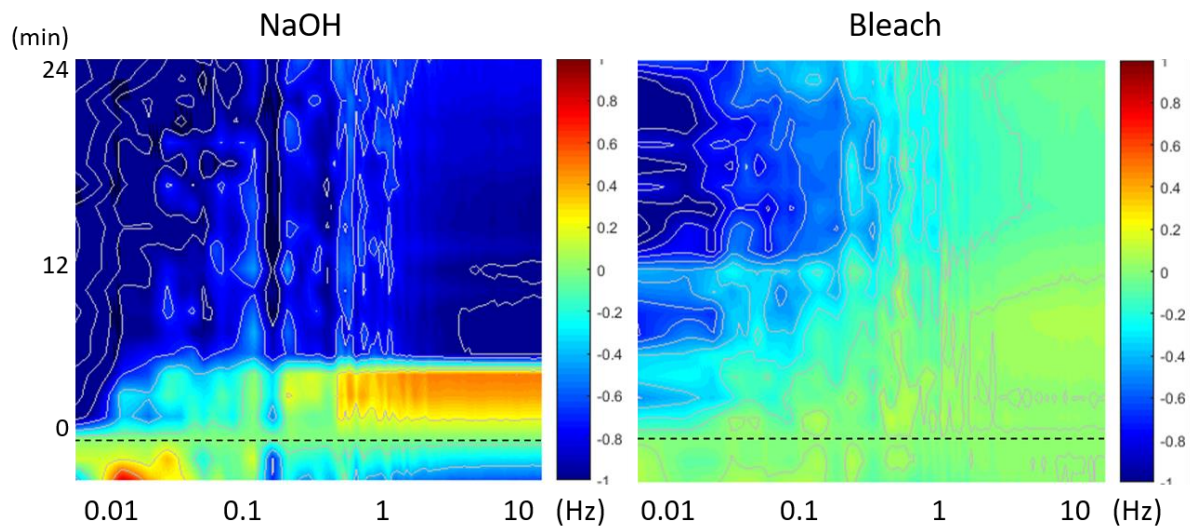


Figure 3.9 Spectrograms of *E. coli* pellets after applying NaOH and bleach respectively. Low frequency is highly suppressed after adding chemical agents.

The responses of *E. coli*, *S. enterica*, and *L. monocytogenes* pellets to the antibiotic Ciprofloxacin (Cipro) are shown in Figure 3.10(a). Cipro is a broadband antibiotic used for various bacterial infections. The mechanism of action of Cipro is inhibiting DNA gyrase, a Type II topoisomerase, and topoisomerase IV [21, 22] which prohibits DNA replication and results in cell death. To increase water solubility, Ciprofloxacin hydrochloride was used for the antibiotic resistance test (3.5 $\mu\text{g/mL}$). The spectral density changes in the spectral content for Cipro are shown in Figure 3.10(b), and the corresponding spectrograms are shown in Figure 3.11. The response to Cipro is similar to the response produced by the LB medium. Bacterial strains are stimulated by Cipro and induce chemotaxis. *L. monocytogenes* has the weakest response to Cipro, while *E. coli* and *S. enterica* showed stronger Doppler edge enhancement. The highest frequencies in all three cases are not affected. In contrast to the nutrient shock, the Nyquist floors of spectral densities were not altered.

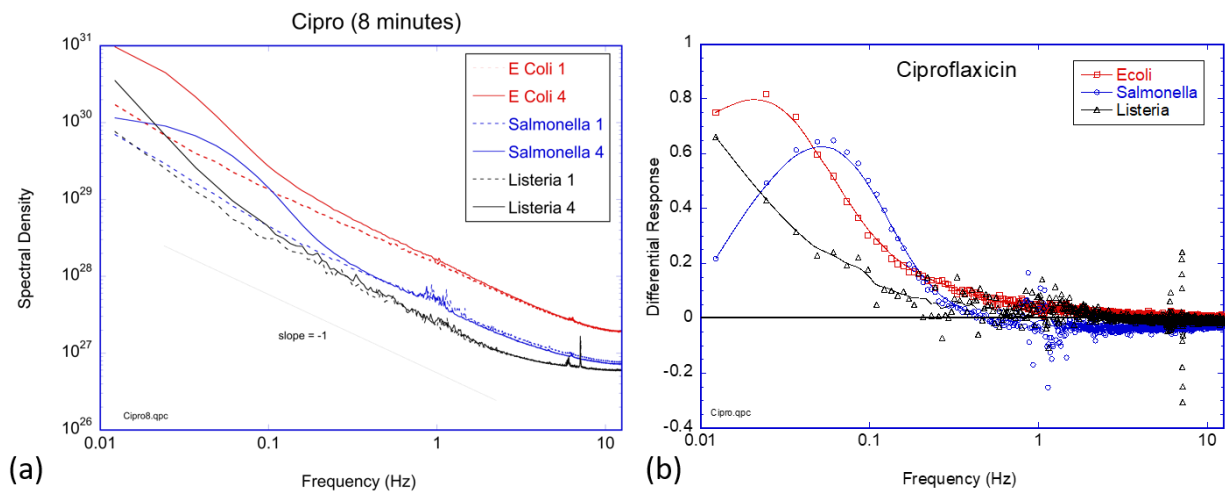


Figure 3.10 (a) Ciprofloxacin (Cipro) responses of *E. coli*, *S. enterica*, and *L. monocytogenes* respectively. (b) The spectral response within 2 minutes after applying Cipro to the three bacterial strains. The Nyquist floors for 3 strains showed almost identical values. The low-frequency responses were immediate and weaker than for the LB medium. *L. monocytogenes* has the weakest response to Cipro. The corresponding spectrograms are shown in Figure 3.11

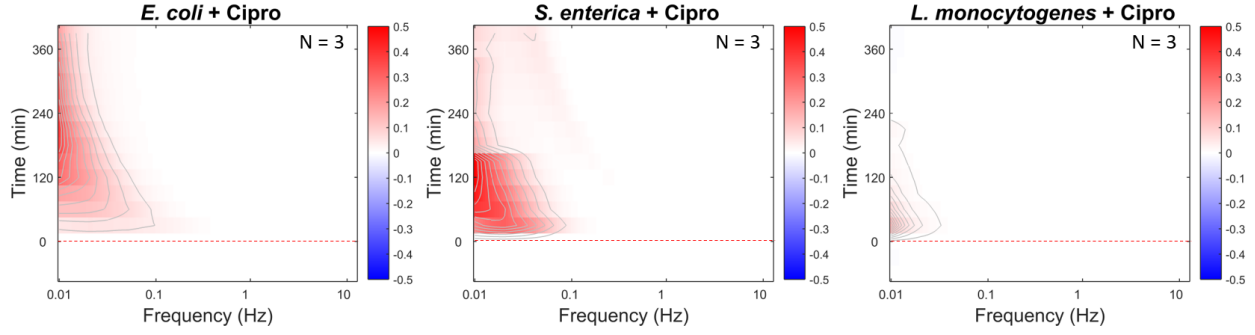


Figure 3.11 Cipro response spectrograms of *E. coli*, *S. enterica*, and *L. monocytogenes*. All strains do not have Cipro resistance.

The antibiotic responses in Figure 3.11 showed a marginal difference compared to the nutrient shock shown in Figure 3.7. The reason why the bacteria showed similar dynamics is that the bacteria swarm when they are exposed to exotic chemical compounds. To test the antibiotic responses further, mammalian host cells are infected by the bacterial strains. The infection assay testing antibiotic sensitivity will be demonstrated in CHAPTER 4.

3.5 Spectral Density Normalization

Previous measurements on biological samples have not had significant BSB enhancement. However, BSB enhancements by bacterial inoculation are physical phenomena that may be caused by bacterial proliferation and increased cellular heterogeneity. Increasing BSB enhances power spectral density and different spectrogram normalizations would result in different analyses. Conventionally, spectral densities were normalized by the sum of spectral components including the DC component ($\omega = 0$). However, a sudden increase in BSB also increases the DC component and makes interpretations of spectrograms confusing. To compensate for the effect and to focus on spectral shifts, three different normalization methods are defined.

$$\begin{aligned}
 S_{norm}(\omega, t) &= S_{raw}(\omega, t) \\
 S_{norm}(\omega, t) &= \frac{S_{raw}(\omega, t)}{I^2} \\
 S_{norm}(\omega, t) &= \frac{S_{raw}(\omega, t)}{\int_{0.01}^{12.5} \frac{S_{raw}(\log \omega, t)}{\omega} d\omega}
 \end{aligned} \tag{3.2}$$

The first normalization is simply the averaged raw baseline spectral density. The result includes the shift of optical power, and the method is not appropriate for analyzing bacterial infection. The second method is normalizing power spectral density by the intensity square. As the total sum of spectral density is the optical intensity square, this normalization method represents the relative dynamic density and excludes the optical power shift. The method assumes the spectral density beyond 12.5 Hz contributes to the Nyquist floor by the stroboscopic effect. The last method is similar to the second method, but the normalization only considers the limited bandwidth (0.01 Hz ~ 12.5 Hz) which deals with the power spectral density from the perspective of probability. The methods are called “Raw spectrum”, “intensity normalization”, and “zero-sum normalization”, respectively. For instance, 4 different spectrograms of *S. enterica* infection (10^7 CFU/well) with different normalization methods are shown in Fig 3.12.

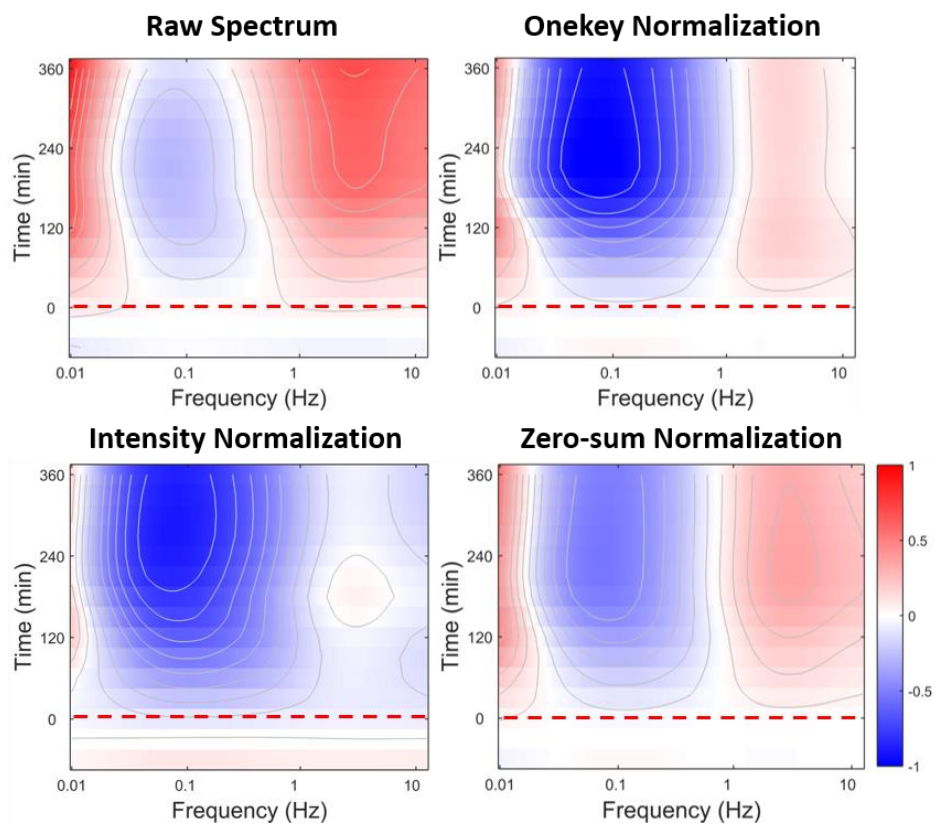


Figure 3.12 Spectrograms obtained from different normalization methods. *S. enterica* infection of DLD-1 (10^7 CFU/well).

In Figure 3.12, the spectrogram derived from raw spectra shows strong enhancement at the low and high-frequency region. The conventional Onekey normalization partially compensates the optical power shift effect, but the spectral enhancement still contains the BSB enhancement effect. Intensity normalization shows the temporal relative dynamic density changes after inoculation while the overall power spectral density is suppressed. Zero-sum normalization shows the probabilistic dynamic density after inoculation.

3.6 Examples of Normalizations and Representations

To demonstrate the perspectives of the normalization methods, two cohorts of genetically identical host-cells were prepared using two different culture conditions and were subsequently infected by *L. monocytogenes* (10^6 CFU per well). The experiments performed in this paper used a relatively fast growth technique that uses non-adherent Corning U-bottom plates to allow cells to aggregate within two days to form loose spheroid samples. Alternatively, a rotating bioreactor can be used to grow tumor spheroids starting from small clumps of cells. The bioreactor growth requires approximately 3 weeks and produces more tightly bound tumor spheroids with a significantly denser extracellular matrix than for the U-bottom samples.

The signature of *L. monocytogenes* infecting U-bottom spheroids is compared to the infection of bioreactor-grown spheroids in Figure 3.13 for the different normalization methods. The lower extracellular matrix (ECM) density of the U-bottom samples produces higher characteristic frequencies than the ECM-rich bioreactor samples. The characteristic frequencies are a factor of 3x to 5x lower for the bioreactor tissue, reflecting the tighter cellular junctions with the ECM. The infection signature of higher ECM density shows a minor spectral enhancement in the high-frequency region (1~10 Hz) after inoculation while the lower ECM density shows globally suppressed spectral density.

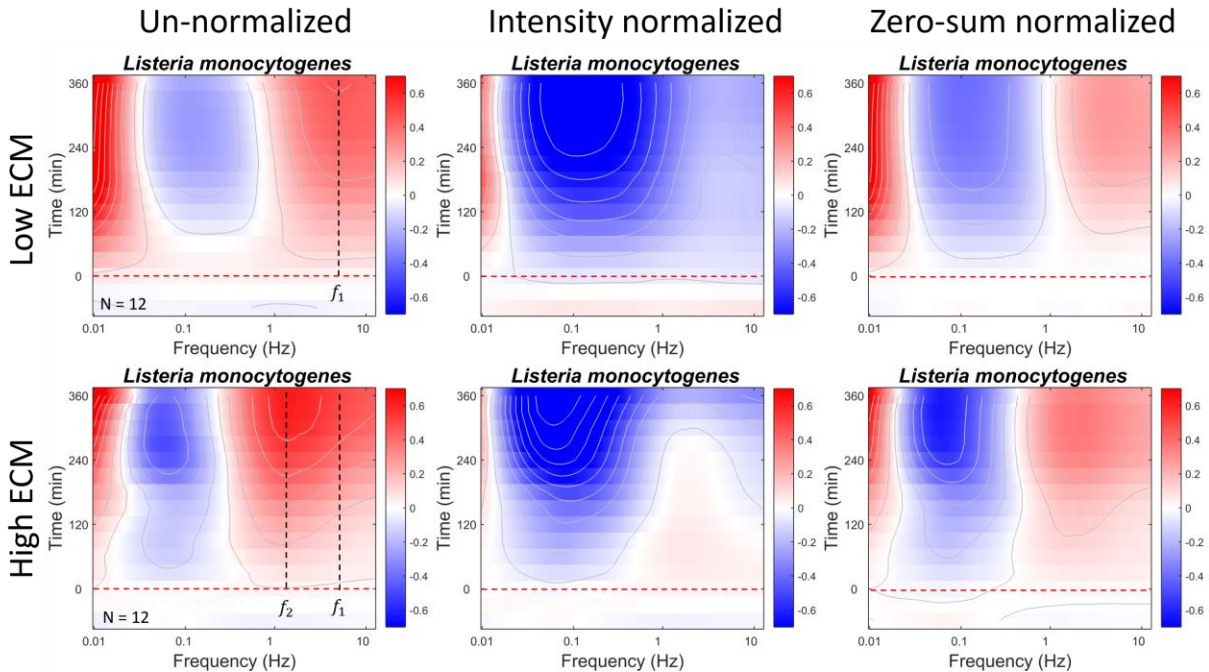


Figure 3.13 *L. monocytogenes* infection of DLD-1 with different extracellular matrix (ECM) densities. Infection signature by *L. monocytogenes* of DLD-1 with lower ECM density (U-bottom growth) and higher ECM density (bioreactor growth). The red dashed lines represent the *L. monocytogenes* inoculation by 10^6 CFU per well. The average rate of *L. monocytogenes* infection of higher ECM density shows slower development. The vertical dashed lines represent the frequency shift of maximum Doppler spectral density at f_1 to f_2 .

The physical representation of the 3 different normalization methods can be summarized by comparing the spectrogram shapes of the low ECM density cohort and the high ECM density cohort. From the un-normalized spectrograms, the maximum spectral density bands can be compared. The enhancements include increased BSB effects, but the maximum densities represent the maximum dynamic density enhancement after inoculation. The un-normalized spectrograms cannot distinguish the enhancement or suppression of the quantitative dynamic, but the qualitative comparison of the dynamic density enhancement is possible. The intensity normalized spectrograms show a quantitative dynamic density comparison. Spectral densities are compensated to exclude BSB enhancement effects, and the quantitative dynamic density shows the difference at the 1 Hz band. The high ECM density cohort has lower high-frequency dynamics which possibly show the dynamics of *L. monocytogenes* immediately after inoculation. The estimated *L. monocytogenes* speed is 330 nm/s (about 20 $\mu\text{m}/\text{min}$) which approximately agrees with the speed measured from previous reports (10 $\mu\text{m}/\text{min}$). The zero-sum normalization spectrograms show a

temporal probability of dynamic densities. The spectral density of the low ECM density cohort has a stable spectral density of about 120 minutes after inoculation. However, the spectral density of the high ECM density cohort shows stabilization after 240 min.

3.7 Discussion

Bacterial motility induced by various reagents were demonstrated. Bacteria is the simplest lifeform, and the swarming characteristics have been recently highlighted to help understand cell-to-cell communication and long-distance interactions. Studying swarming dynamics with conventional methods often hinder establishing reasonable statistics because the number of bacteria forming a swarm is enormous. BDI provides statistical average by measuring Doppler shifts over a million bacteria at the same time. To provide good signal-to-noise ratios and statistics, the bacterial medium was condensed and pellets were extracted. Several strains of bacteria are used to test the swarming motions induced by various reagents. The application of the LB medium stimulated a strong mechanical excitation of the bacterial pellet and changed the optical characteristics. The brightness of the pellet increased immediately after applying the LB medium which is possibly caused by increased optical heterogeneity. In contrast, applying Cipro induced persistent dynamics, but the brightness of the pellet did not change. Testing antibiotic resistance characteristics could not differentiate bacterial dynamics, because reagents always induced bacterial motion inside of the pellet. Infection of mammalian cells with a limited number of bacteria and their characteristic change will be demonstrated in CHAPTER 4.

3.8 References

- [1]. M. C. Lane, V. Lockett, G. Monterosso, D. Lamphier, J. Weinert, J. R. Hebel, D. E. Johnson, and H. L. Mobley, "Role of motility in the colonization of uropathogenic *Escherichia coli* in the urinary tract," *Infect Immun* **73**, 7644-7656 (2005).
- [2]. M. A. Luzar, M. J. Thomassen, and T. C. Montie, "Flagella and motility alterations in *Pseudomonas aeruginosa* strains from patients with cystic fibrosis: relationship to patient clinical condition," *Infect Immun* **50**, 577-582 (1985).

- [3]. L. Sanders, T. M. Andermann, and K. M. Ottemann, "A supplemented soft agar chemotaxis assay demonstrates the *Helicobacter pylori* chemotactic response to zinc and nickel," *Microbiology* **159**, 46-57 (2013).
- [4]. S. E. Childers, S. Ciufu, and D. R. Lovley, "Geobacter metallireducens accesses insoluble Fe(III) oxide by chemotaxis," *Nature* **416**, 767-769 (2002).
- [5]. C. L. Gardel and J. J. Mekalanos, "Alterations in *Vibrio cholerae* motility phenotypes correlate with changes in virulence factor expression," *Infect Immun* **64**, 2246-2255 (1996).
- [6]. H. C. Berg and L. Turner, "Chemotaxis of bacteria in glass capillary arrays. *Escherichia coli*, motility, microchannel plate, and light scattering," *Biophys J* **58**, 919-930 (1990).
- [7]. D. B. Kearns, "A field guide to bacterial swarming motility," *Nat Rev Microbiol* **8**, 634-644 (2010).
- [8]. L. G. Wilson, V. A. Martinez, J. Schwarz-Linek, J. Tailleur, G. Bryant, P. N. Pusey, and W. C. K. Poon, "Differential Dynamic Microscopy of Bacterial Motility," *Physical Review Letters* **106**, 018101 (2011).
- [9]. J. Sambrook, E. F. Fritsch, and T. Maniatis, *Molecular cloning: a laboratory manual* (Cold Spring Harbor Laboratory Press, Cold Spring Harbor, NY, 1989), p. xxxviii + 1546 pp.
- [10]. S. Owens, "E. coli SEM image," Center for Electron Optics, MSU (1996).
- [11]. S. Rabea, M. Salem-Bekhet, F. Alanazi, A. Yassin, N. Moneib, A. Elgawad, and M. Hashem, "A novel protocol for bacterial ghosts' preparation using tween 80," *Saudi Pharmaceutical Journal* (2017).
- [12]. S. Renier, M. Hébraud, and M. Desvaux, "Molecular biology of surface colonization by *Listeria monocytogenes*: An additional facet of an opportunistic Gram-positive foodborne pathogen," *Environmental microbiology* **13**, 835-850 (2010).
- [13]. F. C. Cheong, C. Wong, Y. Gao, M. H. Nai, Y. Cui, S. Park, L. Kenney, and C. T. Lim, "Rapid, High-Throughput Tracking of Bacterial Motility in 3D via Phase-Contrast Holographic Video Microscopy," *Biophysical journal* **108**, 1248-1256 (2015).
- [14]. E. Wright, S. Neethirajan, K. Warriner, S. Retterer, and B. Srijanto, "Single cell swimming dynamics of *Listeria monocytogenes* using a nanoporous microfluidic platform," *Lab Chip* **14**, 938-946 (2014).

- [15]. T. Mashimo, M. Hashimoto, S. Yamaguchi, and S.-I. Aizawa, "Temperature-Hypersensitive Sites of the Flagellar Switch Component FliG in *Salmonella enterica* Serovar Typhimurium," *Journal of Bacteriology* **189**, 5153 (2007).
- [16]. H. E. Kubitschek, "Cell volume increase in *Escherichia coli* after shifts to richer media," *Journal of Bacteriology* **172**, 94 (1990).
- [17]. A. Andino and I. Hanning, "Salmonella enterica: survival, colonization, and virulence differences among serovars," *ScientificWorldJournal* **2015**, 520179-520179 (2015).
- [18]. S. Wang and R. H. Orsi, in *Foodborne Infections and Intoxications (Fourth Edition)*, J. G. Morris and M. E. Potter, eds. (Academic Press, San Diego, 2013), pp. 199-216.
- [19]. D. D. Nolte, R. An, J. Turek, and K. Jeong, "Holographic tissue dynamics spectroscopy," *J Biomed Opt* **16**, 087004 (2011).
- [20]. Z. Li, H. Sun, J. Turek, S. Jalal, M. Childress, and D. D. Nolte, "Doppler fluctuation spectroscopy of intracellular dynamics in living tissue," *J Opt Soc Am A Opt Image Sci Vis* **36**, 665-677 (2019).
- [21]. Y. Pommier, E. Leo, H. Zhang, and C. Marchand, "DNA Topoisomerases and Their Poisoning by Anticancer and Antibacterial Drugs," *Chemistry & Biology* **17**, 421-433 (2010).
- [22]. K. Drlica and X. Zhao, "DNA gyrase, topoisomerase IV, and the 4-quinolones," *Microbiol Mol Biol Rev* **61**, 377-392 (1997).

CHAPTER 4. BIODYNAMIC IMAGING OF BACTERIAL INFECTION OF LIVING TISSUE

4.1 Infection Assay of Pathogenic Bacteria within a Cell Line

Immortalized cancer cell lines are a common and versatile resource as three-dimensional tissue surrogates to study intracellular dynamics in microenvironments that simulate natural living tissues [1-4]. These tissue constructs have characteristic biodynamic spectra that span three orders of magnitude in Doppler frequencies and tend to have characteristic frequencies, known as knee frequencies, that are a single broad spectral feature. Different cell lines can display different knee frequencies depending on how cohesive the tissue is. To investigate infection phenotypes, DLD-1 (adenocarcinoma cancer cell line) were used. All bacterial strains in this study are foodborne pathogens and they actively engage epithelial cells. DLD-1 is a cluster of epithelial cells and has a 3D structure that is expected to represent practical infection processes.

Bacterial infection of living tissue occurs through several different mechanisms. For instance, *L. monocytogenes* actively penetrate the cell membrane (Figure 4.1) [5], while *S. enterica* hijack the actin processes of the cellular membrane to allow them to be internalized (Figure 4.2) [6]. *E. coli*, in contrast, adheres to the exterior of the cell [7]. These different mechanisms may be expected to alter the underlying cellular dynamics of the tissue in different ways that may be related to the characteristics of the bacteria. DLD-1 was inoculated by various strains and the infection phenotypes of the bacterial strains were studied. Furthermore, antibiotic-resistant bacteria infection phenotypes were compared by treating with sensitive and resistive antibiotics.

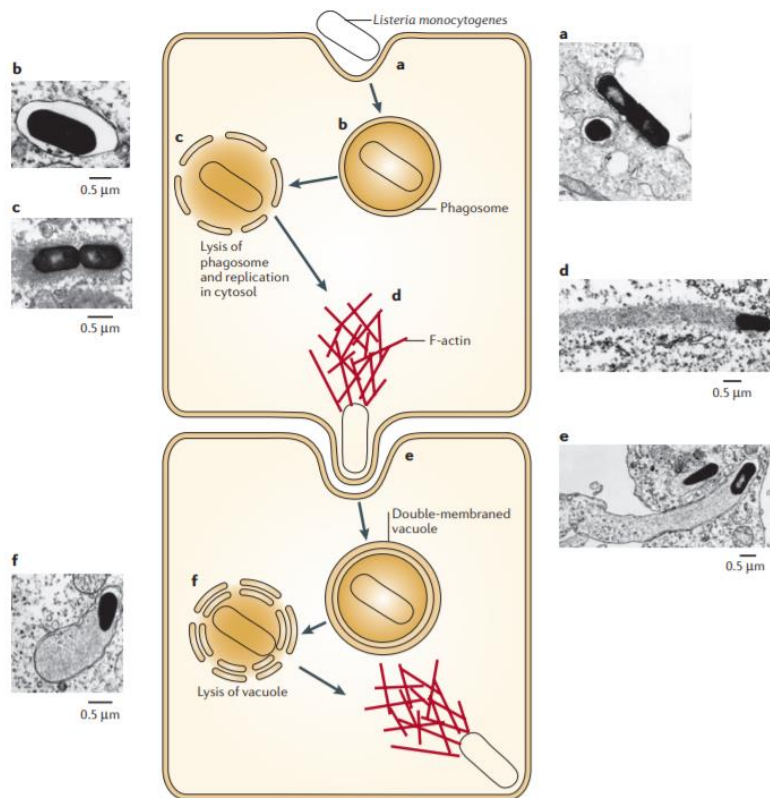


Figure 4.1 *L. monocytogenes* infection mechanism. (From [5]) *L. monocytogenes* physically penetrate a host cell's membrane and internalize. After internalization, *L. monocytogenes* polymerize actin molecules and form polymeric Filament-actins (F-actin). The F-actin formation at the end of *L. monocytogenes* physically pushes toward the neighboring host cell and spreads the infection. The average propulsion speed is about 10 μm/min.

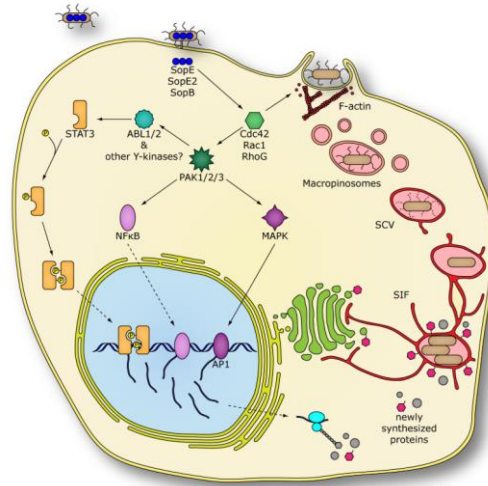


Figure 4.2 *S. enterica* internalization. (From [6]). *S. enterica* adheres to a host cell's membrane and manipulates F-actin formation. F-actin formation induces a local cellular membrane motion that engulfs *S. enterica*. Internalized *S. enterica* uses the host cell's resources and replicates. After multiple replications inside of a host cell *S. enterica* saturates, bursts, and releases *S. enterica* daughter cells that forage other host cells.

4.2 Infection-Induced Intracellular Activity

The temporal responses of bacterial infection of DLD-1 spheroids are shown in Figure 4.3. 10^7 colony formation units (CFU) of bacteria were inoculated per well [8]. All of the speckle brightness increased, and NSD decreased after bacterial inoculation. *L. innocua* has a minimal effect on DLD-1 due to their inefficient replication [9], while other bacterial strains changed the optical characteristics of DLD-1. *E. coli* inoculation induced the strongest BSB enhancement. The negative control has a stable BSB and NSD.

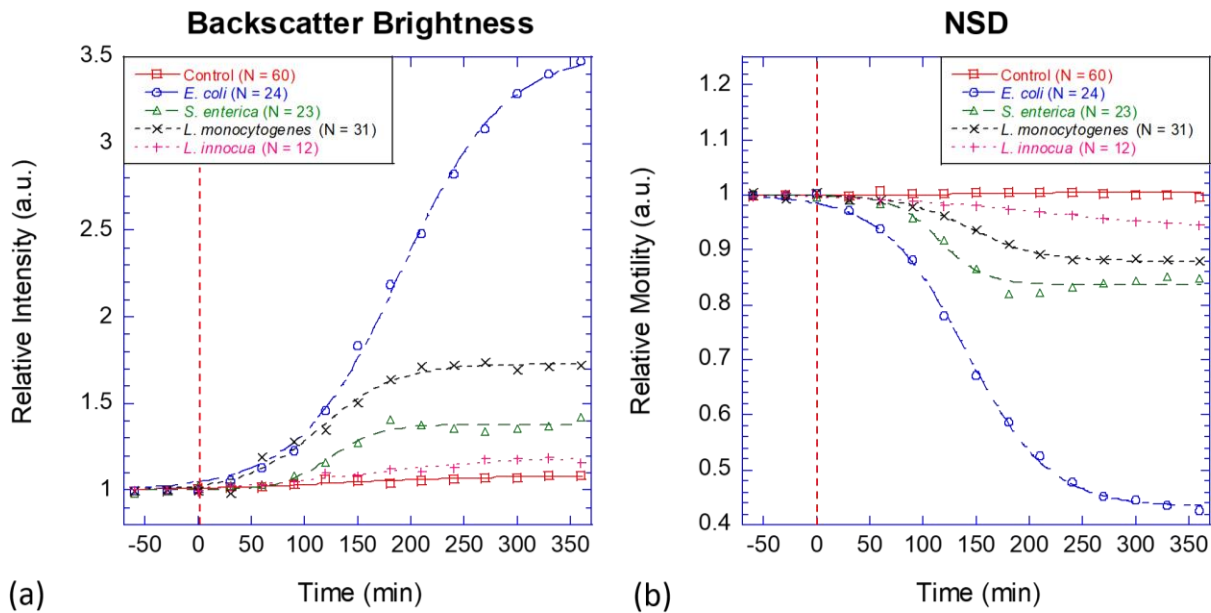


Figure 4.3 Inoculation with 10^7 CFU/well. (a) BSB change of *E. coli* and *S. enterica*, *L. monocytogenes*, and *L. innocua* after inoculation in DLD-1 spheroids (red dashed lines). (b) Temporal responses of NSD.

Bacterial replication inside of wells may enhance BSB significantly which may be caused by increased optical heterogeneity. 10^6 CFU/well inoculation is also demonstrated in Figure 4.4. *S. enterica* and *L. monocytogenes* showed a similar degree of BSB enhancement, while *E. coli* showed a decreased BSB enhancement compared to 10^7 CFU/well BSB enhancement.

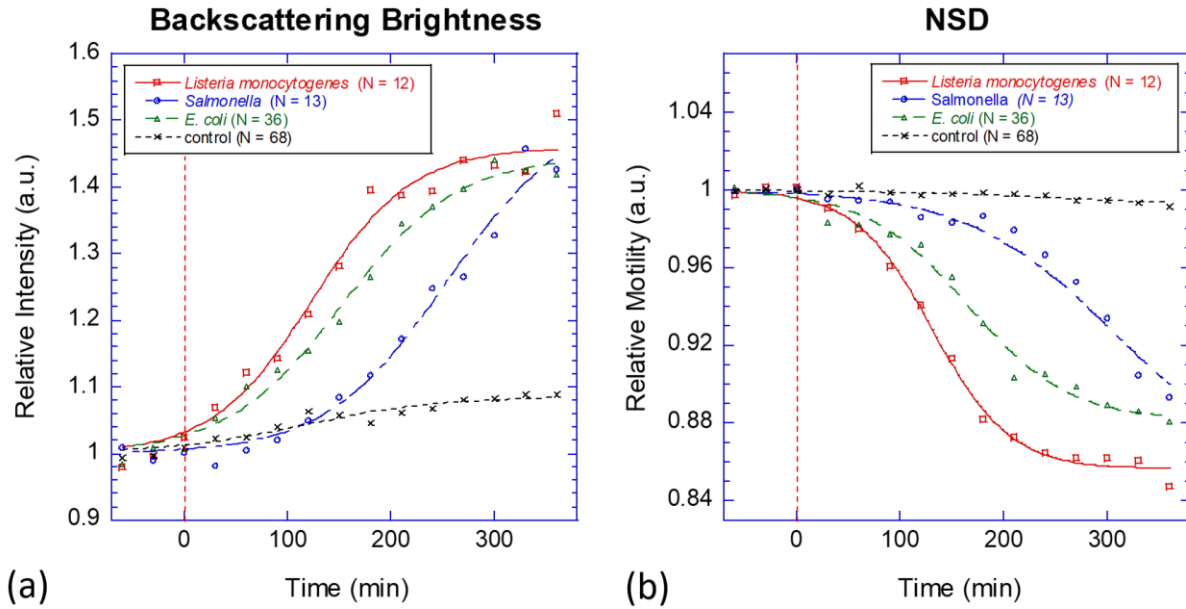


Figure 4.4 Inoculation by a lower number of bacteria (10^6 CFU/well). (a) BSB enhancement of all strains showed a similar degree of enhancement. (b) NSD of *L. monocytogenes* decreased most rapidly and *S. enterica* showed the slowest decrease.

BSB and NSD are two phenotypic features representing dynamic characteristics of DLD-1, but the significant enhancement of BSB might dominate NSD. To investigate the bacteria inoculation effect, the dynamic range (DR) was introduced as a BSB independent biomarker and compared. DR of the spectral density estimates the change in dynamics. DR is the ratio of the first 5 lowest-frequency Doppler power spectral density average divided by the highest-frequency 5 components. DR decreases when the Nyquist floor increases. The increment of the Nyquist floor is contributed by the stroboscopic effect [10] which represents the increasing high-velocity dynamics above 12.5 Hz bandwidth. On the other hand, the dynamic range increases if the dynamics around 0.01 Hz in the low-frequency band is enhanced. The change in dynamic range relative to the pre-inoculation averages is shown in Figure 4.5. Increased dynamic range after inoculation was observed for *E. coli*, *S. enterica*, and *L. innocua*, but not for *L. monocytogenes*. Non-monotonic behavior may represent successive “waves” of infection or competition for nutrients.

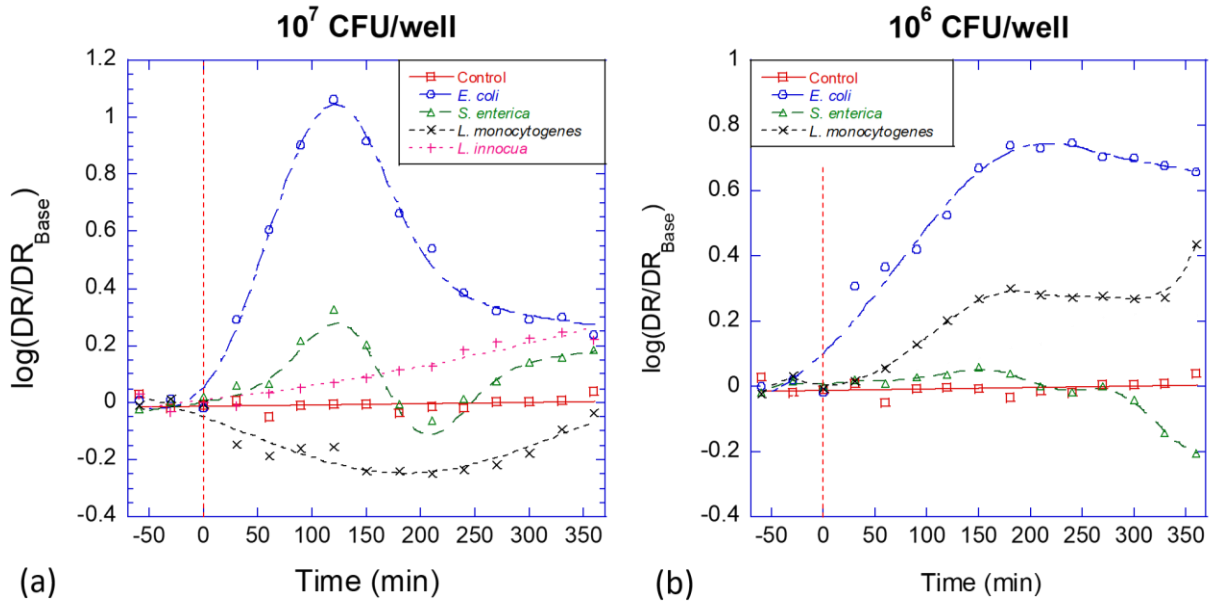


Figure 4.5 Dynamic range of (a) 10^7 CFU/well and (b) 10^6 CFU /well. The lower dose inoculation shows temporally delayed responses. 10^6 CFU inoculation of *L. monocytogenes* shows different behavior of 10^7 CFU which suggests 10^7 CFU inoculation partially captures Doppler signals from rapidly moving bacteria as well.

The difference between 10^7 CFU and 10^6 CFU inoculations are compared in terms of DR in Figure 4.5. Temporal DR responses of 10^6 CFU inoculation showed about 80 minutes of delayed response compared to 10^7 CFU inoculations. The reproduction cycle takes about 20~30 minutes and 80 minutes correspond to 3~4 reproduction cycles (8~16 times) which is consistent with the initial inoculation concentration difference.

Inoculations of 10^7 CFU/well and 10^6 CFU/well induce different optical characteristics due to the different number of bacteria/spheroid density. By assuming the bacteria inoculations spread bacteria at the bottom of the well, the bacteria density per area becomes 3×10^6 CFU/mm² and 3×10^5 CFU/mm² for 10^7 CFU/well and 10^6 CFU/well, respectively. Approximating the shape of DLD-1 spheroids as a cylinder with the diameter 1 mm and thickness 0.5 mm, the CFU of inoculated bacteria directly interacting with DLD-1 becomes 2.4×10^6 CFU and 2.4×10^5 CFU. The estimated bacterial density with a uniform infection of DLD-1 becomes 7×10^9 CFU/mL and 7×10^8 CFU/mL, and corresponding estimated optical densities (OD₆₆₀) are 2.23 cm^{-1} and 0.2 cm^{-1} .

¹, respectively [11]. The total intensity of scattered light from bacteria inside of DLD-1 spheroids can be estimated by the relation

$$I = I_0(1 - 10^{-ODz}) \quad (4.1)$$

From Eq.(4.1) and obtained ODs, the reflected light portions from bacteria are about 22% and 2% of incident light for 10^7 CFU/well and 10^6 CFU/well inoculation, respectively. The inoculation concentration 10^6 CFU/well was used for the antibiotic susceptibility assays.

OCI images of DLD spheroids, before and after infection by *E. coli*, *S. enterica*, *L. monocytogenes*, and *L. innocua* are shown in Figure 4.6 and Figure 4.7. Infection increased BSB for all bacterial strains. Increasing bacterial density in the host cell increased BSB by increasing optical heterogeneity around 3D cellular structures. The OCI images after infection showed a more heterogeneous intensity distribution. Also, MCI showed overall suppression with heterogeneous NSD distributions. The shape of the speckles did not change significantly.

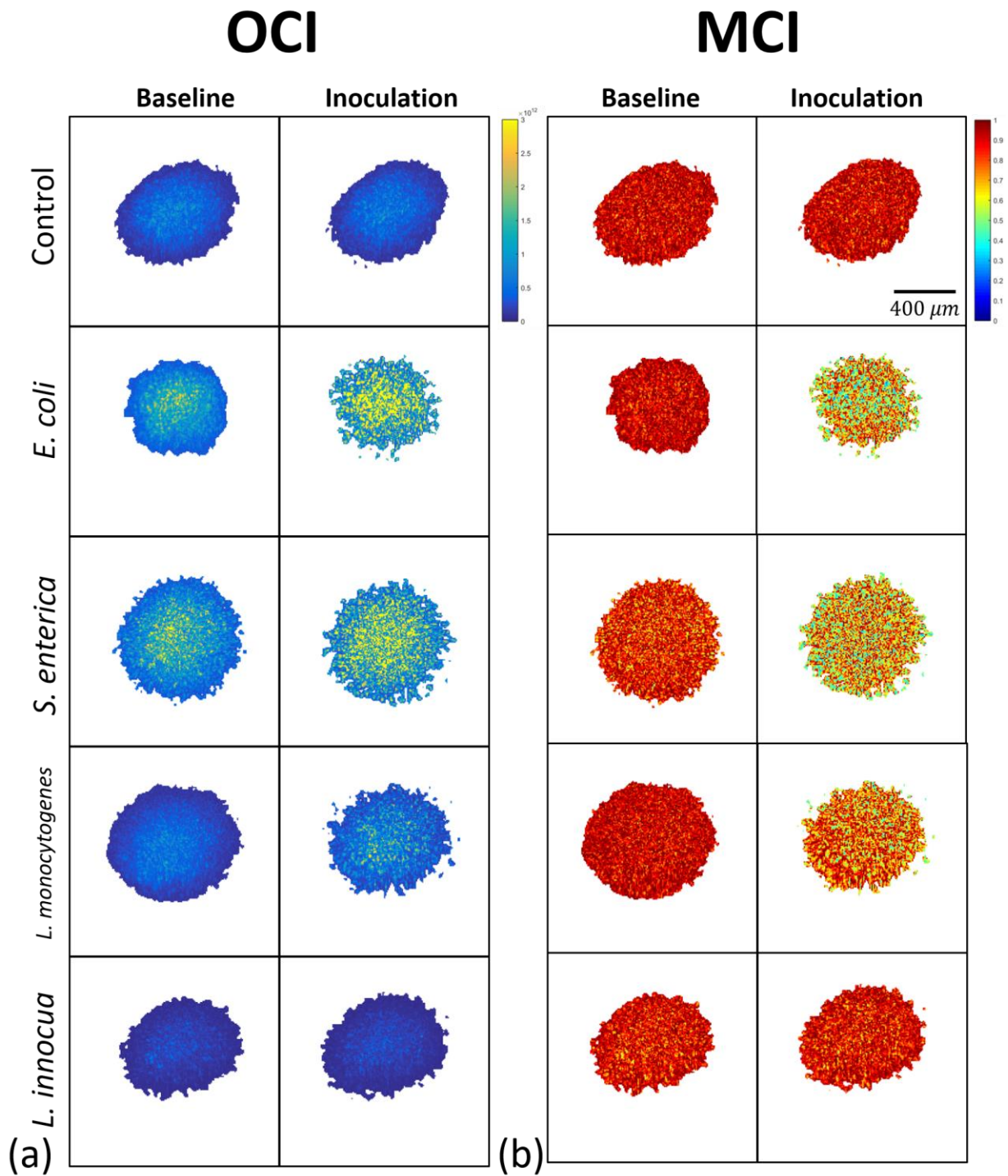


Figure 4.6 Initial and final (a) OCI and (b) MCI of DLD-1 spheroids infection by various bacteria strains by inoculating 10^7 CFU/well.

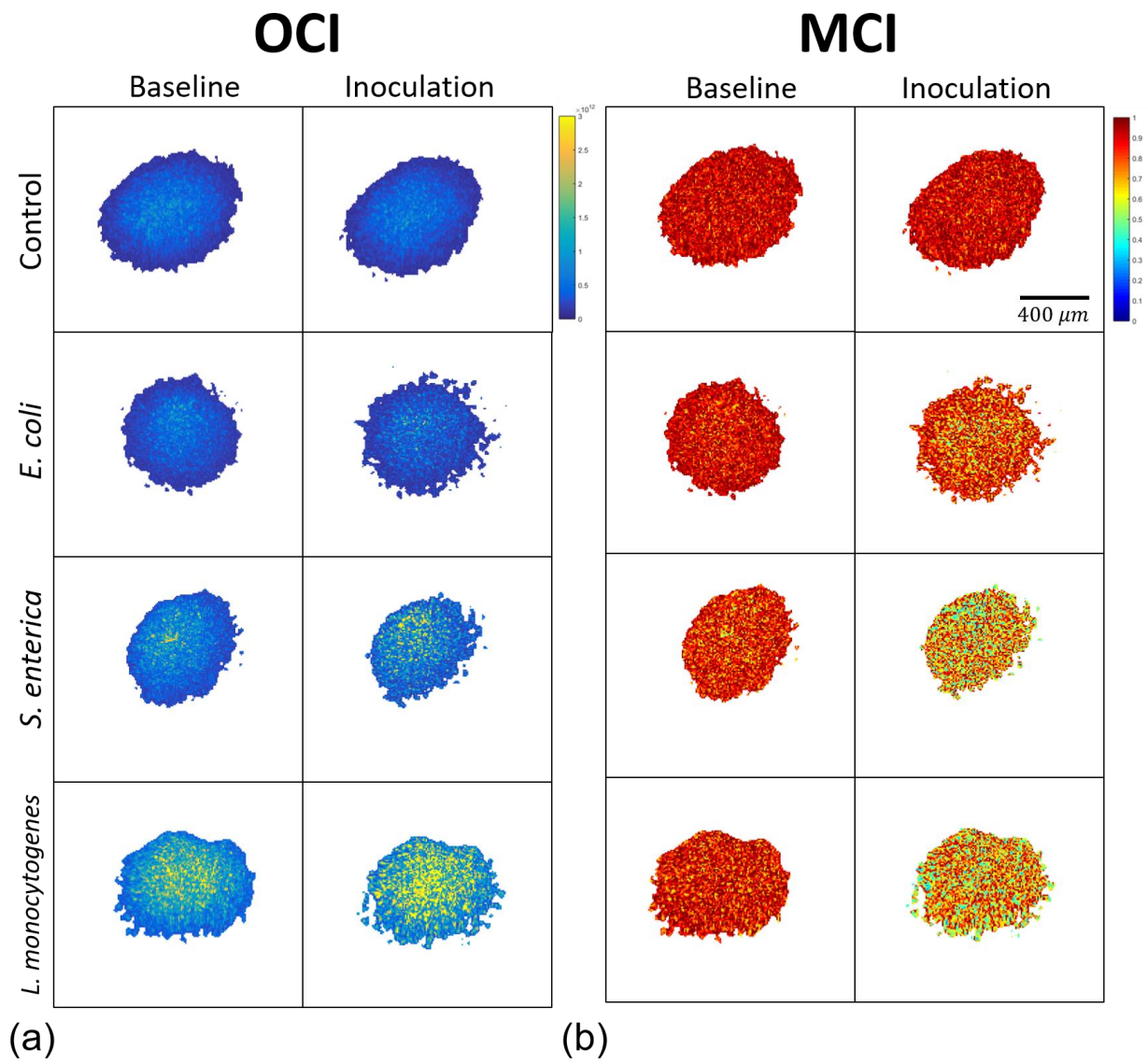


Figure 4.7 (a) OCI and (b) MCI for 10^6 CFU/well inoculation.

4.3 TDS of Infection Assays

Bacteria-host-cell interaction can be quantified by measuring power spectral variation after inoculation. Doppler spectral bands correspond to different dynamics such as the rheology band (0.01 Hz), the membrane band (0.1 Hz), and the organelle transport band (1 Hz) [12]. Suppression or enhancement of the power spectral density represents changes in dynamic characteristics. The power spectral densities of DLD-1 under 10^7 CFU/well *E. coli* inoculation are shown in Figure 4.8. The initial spectrum of the DLD-1 has a knee frequency feature at 0.1 Hz (corresponding to a characteristic intracellular speed of 30 nm/sec). When DLD-1 is exposed to *E. coli*, the spectral shape is converted to a $1/f$ spectrum with a suppression of the Doppler knee in the mid-frequency region, with an increased low-frequency rheology band, and a slight increase in the high-frequency region. Spectral densities are normalized by the intensity squared using the intensity normalization method. All spectrograms in this chapter used the intensity squared normalization. The TDS spectrograms of various bacterial infections are shown in Figure 4.9.

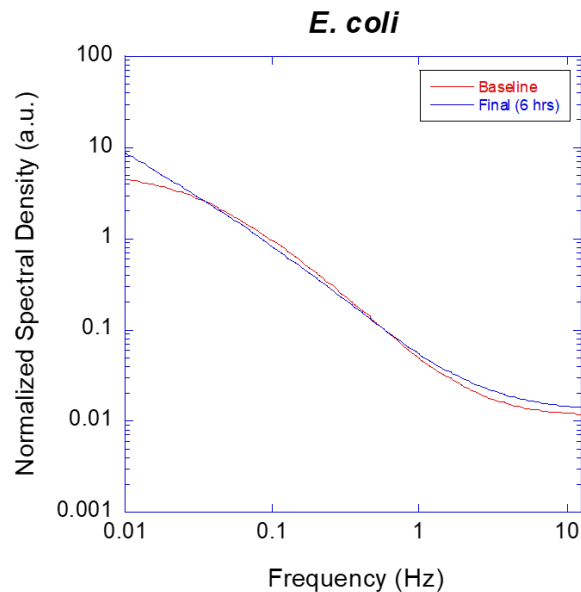


Figure 4.8 Spectrum of DLD-1 under infection by 10^7 CFU/well of *E. coli*. The time difference between the baseline and the final measurement is 6 hours.

Suppression on the spectral densities occurs for inoculation by all bacterial strains. *E. coli* shows an initial weak enhancement at the low-frequency region immediately after the inoculation. *S. enterica* shows a spectral enhancement at the high-frequency region about 200 minutes after inoculation which is also demonstrated in Figure 4.5. *L. monocytogenes* shows instantaneous high-

frequency enhancement which may be caused by bacterial foraging. *L. innocua* shows a minimal suppression at the mid-frequency region and minor delayed enhancement at the high-frequency region.

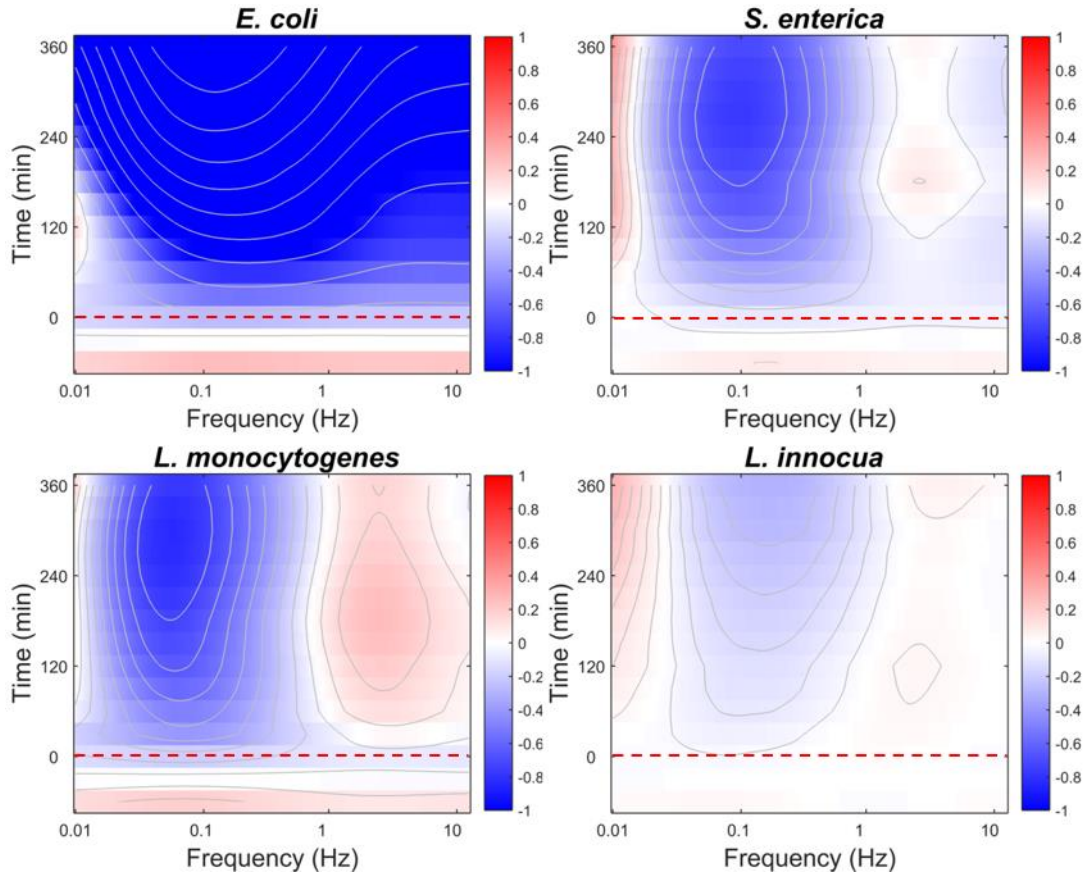


Figure 4.9 Tissue dynamics spectrograms (TDS) of DLD-1 tissue spheroids inoculated (red dashed lines) by 10^7 CFU/well of *E. coli*, *S. enterica*, *L. monocytogenes*, and *L. innocua*.

From Figure 4.5, different DR behavior of *L. monocytogenes* after inoculation suggests 10^7 CFU/well inoculation captures direct light scattering from bacterial while 10^6 CFU/well does not. To try to isolate the cellular response of DLD-1, 10^6 CFU/well was also inoculated and analyzed in Figure 4.10.

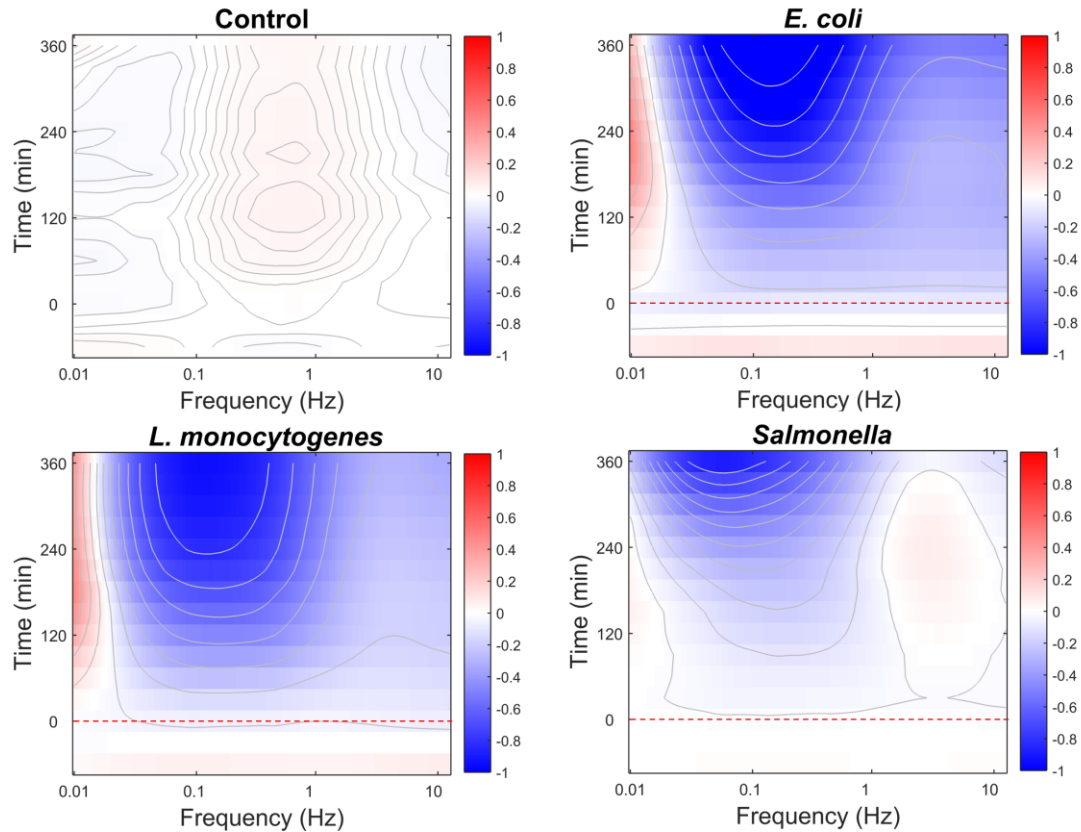


Figure 4.10 Spectrograms of *E. coli*, *L. monocytogenes*, and *S. enterica* at 10^6 CFU/well.

Spectral suppression induced by *E. coli* is not as significant as at 10^7 CFU/well inoculation. The high-frequency enhancement of *L. monocytogenes* observed in Fig 4.9 is not observed in Figure 4.10. The high-frequency enhancement of *S. enterica* is observed for 10^6 CFU/well as well as 10^7 CFU/well, which may be caused by the infection mechanism of *S. enterica* which hijacks the host cell's cellular functions and uses the host cell's resources to replicate.

4.4 Doppler Spectral Band Analysis

The time traces of selected spectral ranges are shown in Figure 4.11 for the rheology band (10 mHz) and the organelle transport band (2 Hz – 6Hz) for an applied exposure of 10^7 CFU/ well. The rheology band is associated with slow cellular shape changes and also with reduced speeds of mid-frequency processes related to membranes or larger organelles like the nucleus. At the high bacterial load of 10^7 CFU/well there is a strong non-monotonic time dependence of the spectral density of the rheology band as a maximum appears after approximately 2 hours and then the

signal decreases. In the case of *S. enterica* and *L. monocytogenes*, the secondary minimum gives way to a later increase, while for the non-pathogenic *E. coli* and *L. innocua* the secondary minimum does not occur. The organelle band presents a relatively “clean” signal because the only intracellular constituents that contribute to this spectral range are the smaller organelles and vesicles. The spectral density of the organelle band is enhanced for all but *E. coli* infection. Organelle and vesicle transport are associated with active cellular responses to xenobiotics as well as with early-stage apoptosis. The higher frequencies are also associated with the motion of the bacteria themselves.

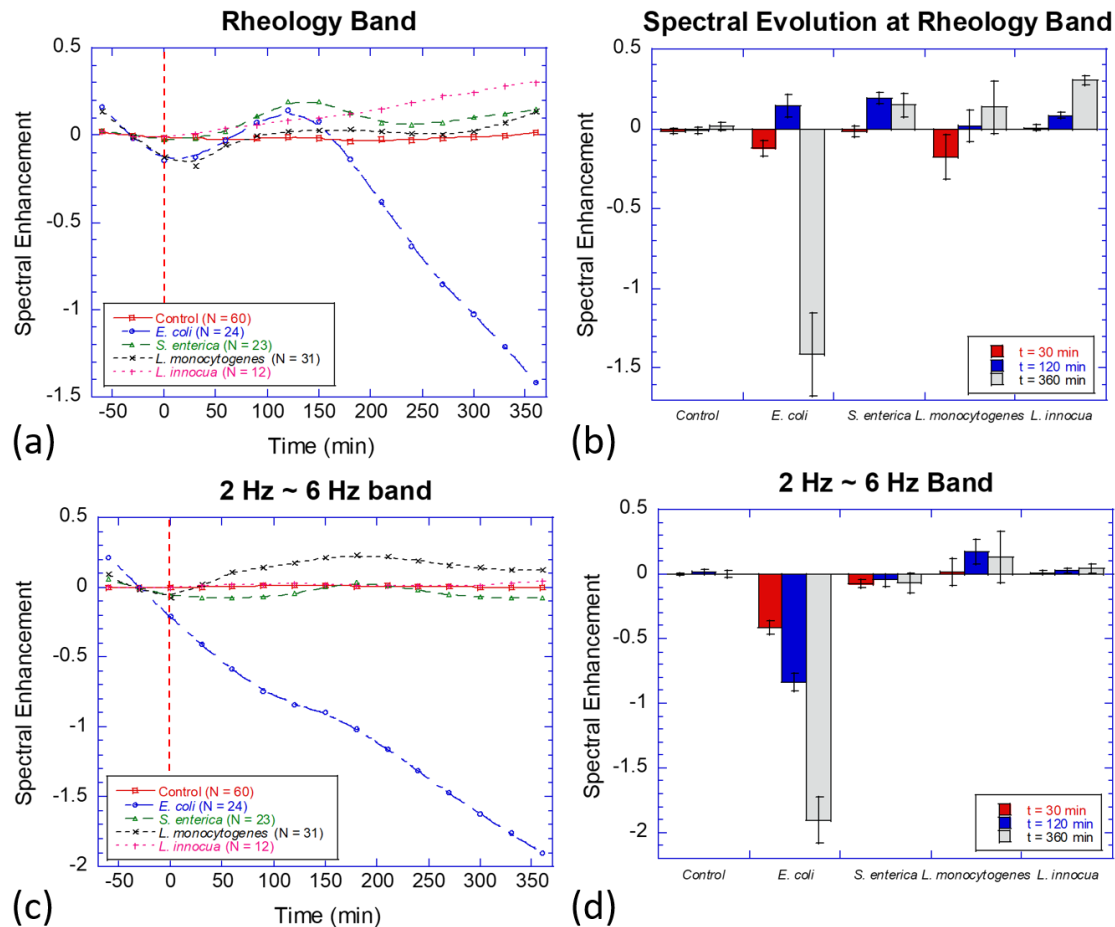


Figure 4.11 Time development of the relative spectral changes for a dose of 10^7 CFU/well. (a) The low-frequency limit for the rheology band. All bacterial strains showed temporal variation in this band. *E. coli* infection displays the strongest suppression. The two pathogenic strains, *S. enterica*, and *L. monocytogenes* show non-monotonic increases, with a decrease after the first maximum, followed by a long-term increase. Long-term increases for the rheology band have been associated with blebbing or the formation of apoptotic bodies associated with either uncontrolled or controlled cell death. *L. innocua* show a slow and monotonic increase. (b) Change in the Doppler rheology band for three selected times and standard errors. (c) Time dependence of the high-frequency band associated with organelle transport. *L. monocytogenes* show strong initial increases within one hour followed by a slow decrease at longer times. *S. enterica* show a weak enhancement at 3 hours after inoculation. The case for *E. coli* shows strong suppression consistent with an overall inhibition of Doppler activity. (d) Change in the Doppler organelle transport band at three selected times.

4.5 Tissue-dynamic Spectroscopic Imaging of Infection Assay

Tissue-dynamic spectroscopic imaging (TDSI) is an algorithm that creates maps of spectral shape evolution. For instance, the power spectral response of a DLD-1 spheroid may have regional heterogeneity due to inhomogeneous distribution of nutrients. Conventional BDI takes averages of the power spectra across the entire tissue sample, but spatial information is lost. To study the spatial characteristics of tissues, the spectral responses are obtained for each pixel of the OCI reconstruction. After measuring the baseline spectra for each pixel, the TDSI algorithm compares the spectral variation over time compared to the averaged baseline of the sample. Spectral shape changes can be mapped using biomarkers, and the multi-color algorithm marks pixels with red when the spectral response is strongly correlated to the biomarker and blue for anticorrelated (Figure 4.12).

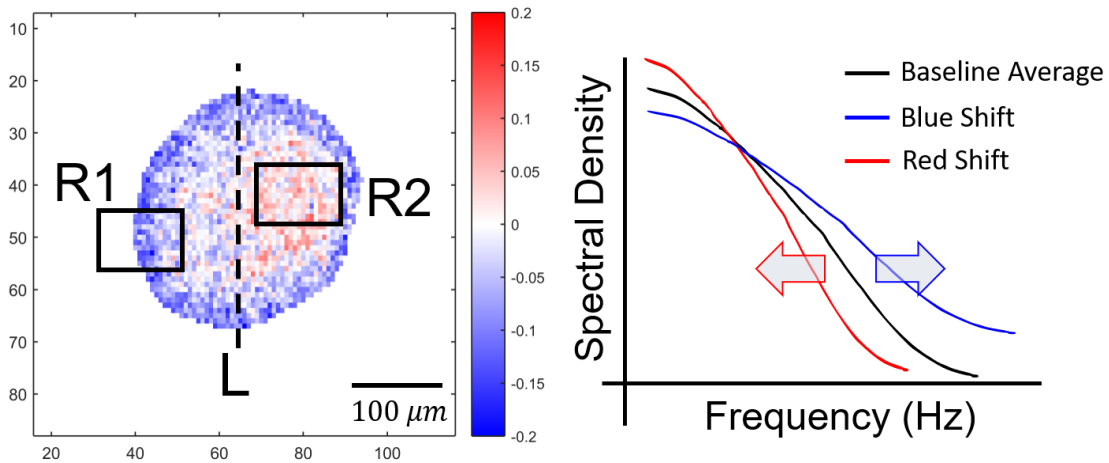


Figure 4.12 An example of tissue-dynamic spectroscopic imaging (TDSI). The blue and red color represents a blueshift or a redshift of power spectral density. The region R1 and R2 show different spectral shifts.

The biomarker for TDSI in Figure 4.13 was SDIP0 which detects spectral blue- and redshifts. As the bacterial infection induces an anomalous high-frequency enhancement, TDSI captures the spreading of the infection. Examples of TDSI for several bacterial strains are shown in Figure 4.13.

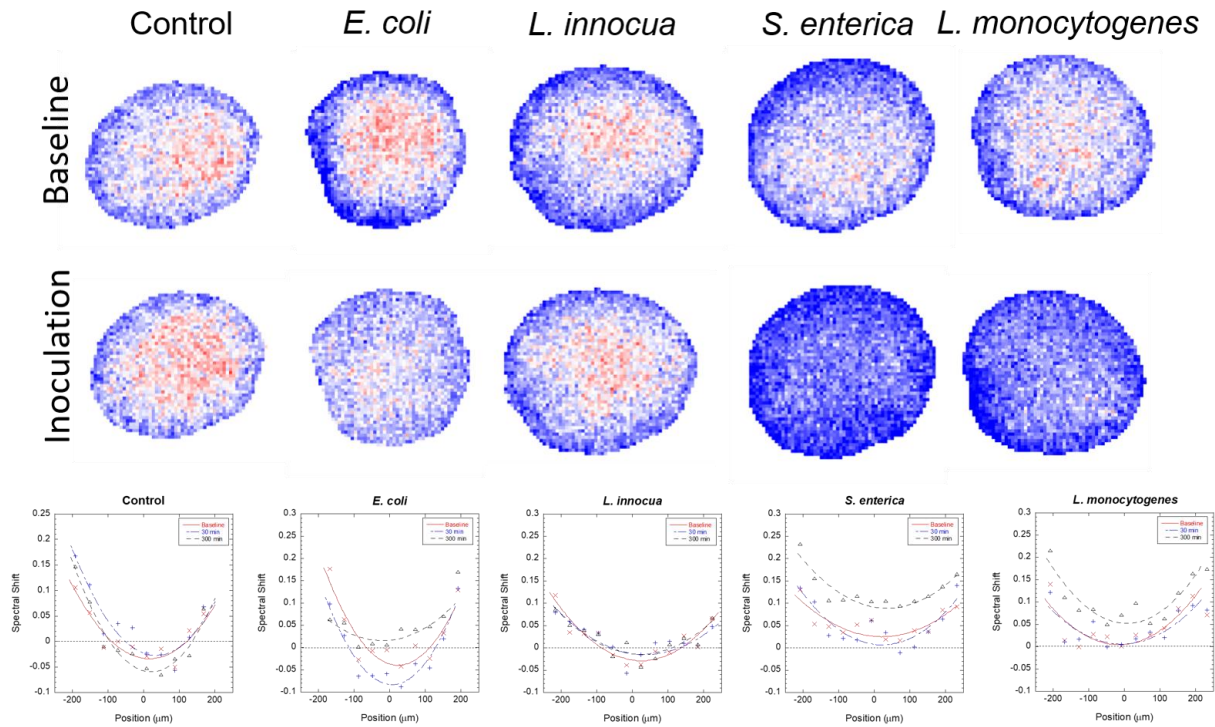


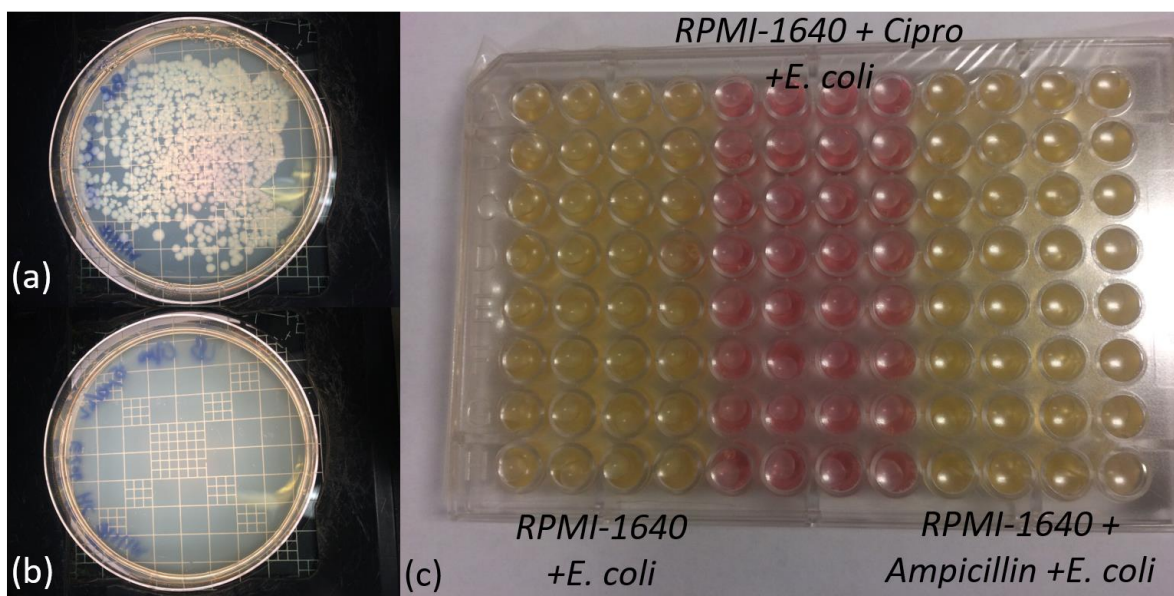
Figure 4.13 Bacterial infection and the corresponding TDSI. The invasive strains (*S. enterica* and *L. monocytogenes*) show spreading blueshift while non-invasive strains (*E. coli* and *L. innocua*) did not. Lower graphs represent a 1D plot at the centers of TDSIs.

Control and non-invasive strains did not show significant changes. In contrast, invasive strains (*S. enterica* and *L. monocytogenes*) showed spreading blueshifts toward the inner core which may be caused by bacterial migrations to neighboring uninfected host cells.

4.6 Antibiotic Responses of Antibiotic Resistance Bacteria

The standard method for testing antibiotic resistance is the agar plating method [13]. The method uses an agar plate containing nutrients and antibiotics, and establishes bacterial colonies on the agar surface for 24 hours. When bacteria are sensitive to the antibiotics in the agar, no colony can be formed on the agar. In contrast, when bacteria are resistive to the antibiotics, bacteria can form colonies. The method has good sensitivity but it requires 24 hours to have a result. BDI can measure infection signals, and antibiotics are expected to inhibit bacterial activities and recover the intracellular dynamics of the host cells.

Bacterial antibiotic responses were measured by applying antibiotics after applying bacteria to the DLD-1 spheroids. To measure antibiotic resistance, *E. coli* green-fluorescence protein (GFP) strain was selected (O157:H7 American Type Culture Collection 43894). *E. coli* GFP has ampicillin resistance because genes are genetically engineered to have an ampicillin resistance gene at the same promoter as the GFP synthesizing gene [14]. The *E. coli* strain used for the antibiotic resistance assay has ampicillin resistance enabling the bacteria to survive up to a dose of 50 µg/ml ampicillin. 10⁶ CFU/well *E. coli* were inoculated into DLD-1 wells. After the inoculation, the infection progressed for 5 hours. The negative control group was treated by the RPMI-1640 medium that does not contain antibiotics. The antibiotic treatment used two antibiotics separately which are ampicillin and Cipro. The ampicillin-resistant *E. coli* secretes β-lactamase enzymes and neutralizes chemical toxicity against *E. coli* [15]. However, the chemical structure of Cipro is different from ampicillin, and the ampicillin resistance mechanism is unable to neutralize the toxicity of Cipro (Figure 4.14).



	RPMI-1640 Medium	Medium + <i>E. coli</i> (N = 3)	Medium + <i>E. coli</i> + ampicillin (N = 3)	Medium + <i>E. coli</i> + ciprofloxacin (N = 3)	Medium + DLD-1 (N = 16)
pH	7.4	6.79 ± 0.01	6.76 ± 0.03	8.08 ± 0.01	7.47 ± 0.01

Figure 4.14 Ampicillin resistant *E. coli* colony formation on an agar plate (a) with ampicillin and (b) with Cipro. (c) The RPMI-1640 medium inoculated by 10⁶ CFU/well *E. coli* and incubated for 24 hours. The pH of the RPMI-1640 medium was altered by the *E. coli* growth but the medium with Cipro did not. The increment of pH of the RPMI-1640 medium is caused by losing CO₂ dissolved in the bicarbonate buffer.

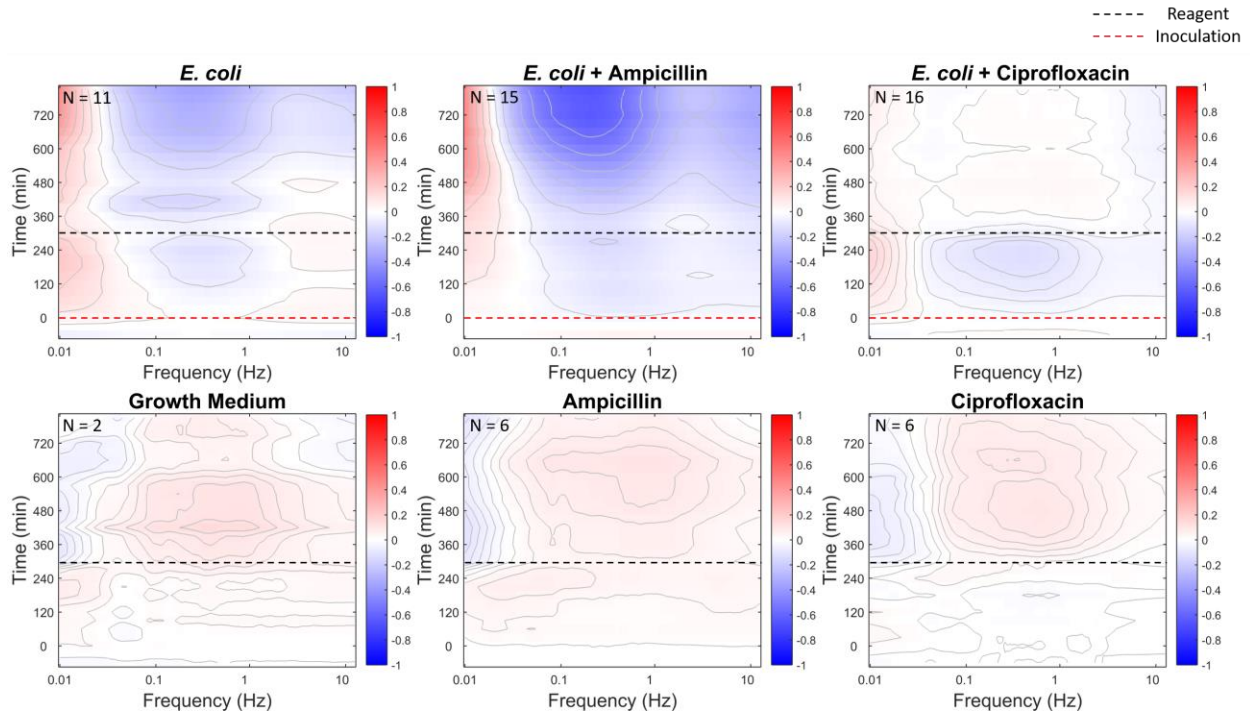


Figure 4.15 Antibiotic-resistant assay. The upper row group was inoculated by *E. coli*. The lower group was not inoculated. The first column was treated by the RPMI-1640 growth medium without antibiotics. The second column was treated by RPMI-1640 with ampicillin (50 $\mu\text{g}/\text{mL}$). The last column was treated by Cipro (3.5 $\mu\text{g}/\text{mL}$). The group treated by Cipro completely recovered from the infection.

BDI tracks the *E. coli* infection spectrum of DLD-1 for 4.5 hours, at which time three different treatments are applied to the tissue sentinels in separate wells: growth medium (control), ampicillin (50 $\mu\text{g}/\text{ml}$) and ciprofloxacin (3.5 $\mu\text{g}/\text{ml}$). The time-course spectrograms are shown in Figure 4.15 for the three treatments. The top row shows the responses for the infected DLD-1 spheroids. The dashed red line is the time of bacterial inoculation, and the dashed black line is the time of antibiotic application. The bottom row shows the responses of the tissue sentinel controls without bacterial infection. The controls are similar for all treatments, displaying a mild mid-frequency enhancement in response to the treatment that includes replenished growth medium with nutrients. The DLD-1 spheroids with bacterial infection show a broad-band suppression of activity within the tissue. Application of ampicillin has little effect (for this ampicillin-resistant strain), while Cipro removes the bacterial infection and returns the tissue to a condition comparable to the control.

4.7 Discussion

Light scattered from living tissue displays a broad range of Doppler frequency shifts related to complex cellular processes and their associated dynamic motion. The Doppler fingerprint of living tissue is extremely sensitive to subtle changes in intracellular dynamics, and BDI provides a powerful new technique for monitoring the response of 3D living tissue to xenobiotic challenges. In this chapter, we describe the first use of BDI to monitor the infection of 3D living tissue by bacteria. Bacteria affect many of the dynamic processes within the living host, allowing the cellular response to perform the role of a living sentinel, reporting on the effects of the bacterial infection as well as monitoring the efficacy of antibiotic treatments. To illustrate the infection-induced power spectral responses, tumor spheroids of the DLD-1 colon adenocarcinoma cell lines were used to highlight different characteristics caused by infection by different bacterial strains. The spectral enhancements represent changes in dynamics with different frequency ranges associated with different types of intracellular motion. This work demonstrates the potential to translate BDI to the clinic to test for antibiotic-resistant infections.

4.8 References

- [1]. C. Unger, N. Kramer, A. Walzl, M. Scherzer, M. Hengstschlager, and H. Dolznig, "Modeling human carcinomas: physiologically relevant 3D models to improve anti-cancer drug development," *Adv Drug Deliv Rev* **79-80**, 50-67 (2014).
- [2]. B. Weigelt, C. M. Ghajar, and M. J. Bissell, "The need for complex 3D culture models to unravel novel pathways and identify accurate biomarkers in breast cancer," *Adv Drug Deliv Rev* **69-70**, 42-51 (2014).
- [3]. B. M. Baker and C. S. Chen, "Deconstructing the third dimension – how 3D culture microenvironments alter cellular cues," *Journal of Cell Science* **125**, 3015 (2012).
- [4]. K. Jeong, J. J. Turek, and D. D. Nolte, "Volumetric motility-contrast imaging of tissue response to cytoskeletal anti-cancer drugs," *Opt Express* **15**, 14057-14064 (2007).
- [5]. M. Hamon, H. Bierne, and P. Cossart, "Listeria monocytogenes: a multifaceted model," *Nat Rev Microbiol* **4**, 423-434 (2006).
- [6]. S. Hannemann, B. Gao, and J. E. Galán, "Salmonella modulation of host cell gene expression promotes its intracellular growth," *PLoS Pathog* **9**, e1003668-e1003668 (2013).

- [7]. S. P. Riley, K. C. Goh, T. M. Hermanas, M. M. Cardwell, Y. G. Chan, and J. J. Martinez, "The Rickettsia conorii autotransporter protein Sca1 promotes adherence to nonphagocytic mammalian cells," *Infect Immun* **78**, 1895-1904 (2010).
- [8]. S. Y. Lee, "High cell-density culture of Escherichia coli," *Trends Biotechnol* **14**, 98-105 (1996).
- [9]. J. Slaghuis, M. Goetz, F. Engelbrecht, and W. Goebel, "Inefficient replication of Listeria innocua in the cytosol of mammalian cells," *J Infect Dis* **189**, 393-401 (2004).
- [10]. D. Pasculli and G. Manacorda, "Real-time, pseudo real-time and stroboscopic sampling in time-domain GPRs," in *2015 8th International Workshop on Advanced Ground Penetrating Radar (IWAGPR)*, 2015), 1-4.
- [11]. H. Pan, Y. Zhang, G.-X. He, N. Katagori, and H. Chen, "A comparison of conventional methods for the quantification of bacterial cells after exposure to metal oxide nanoparticles," *BMC microbiology* **14**, 222 (2014).
- [12]. Z. Li, H. Sun, J. Turek, S. Jalal, M. Childress, and D. D. Nolte, "Doppler fluctuation spectroscopy of intracellular dynamics in living tissue," *J Opt Soc Am A Opt Image Sci Vis* **36**, 665-677 (2019).
- [13]. L. B. Reller, M. Weinstein, J. H. Jorgensen, and M. J. Ferraro, "Antimicrobial Susceptibility Testing: A Review of General Principles and Contemporary Practices," *Clinical Infectious Diseases* **49**, 1749-1755 (2009).
- [14]. P. M. Fratamico, M. Y. Deng, T. P. Strobaugh, and S. A. Palumbo, "Construction and Characterization of Escherichia coli O157:H7 Strains Expressing Firefly Luciferase and Green Fluorescent Protein and Their Use in Survival Studies‡," *Journal of Food Protection* **60**, 1167-1173 (1997).
- [15]. R. Fernandes, P. Amador, and C. Prudêncio, "β-Lactams: Chemical structure, mode of action and mechanisms of resistance," (2013).

CHAPTER 5. PASE-SENSITIVE BIODYNAMIC IMAING

5.1 Introduction and Background

The mechanical properties of biological systems have been investigated by many optical techniques. For example, optical coherence tomography [1] and fluorescence imaging [2] can visualize micro-scale dynamics in real-time to provide a deeper understanding of biological dynamics. However, at high resolution, the quantitative analysis of dynamics is limited by the optical field of view. Biodynamic imaging (BDI) provides a quantitative analysis of intracellular dynamics [3, 4] by implementing a large field of view with low NA optics. BDI uses digital holographic spectroscopy to measure the broadband Doppler shifts caused by dynamic light scattering (DLS) with 3-dimensional intracellular dynamics of biological specimens [5]. Doppler shifts form a dynamic interference in speckle intensity, and the power spectral density of the Doppler signal can be acquired by performing temporal Fourier transforms of the dynamic speckle intensity fluctuations. The Doppler power spectral density changes over time after applying reagents. The method has measured the chemotherapy responses of various biological specimens, such as canine B-cell lymphoma [6], 3-dimensional xenografts [7], and standard cancer cell lines [8].

The Doppler signal is intrinsically carried by the phase of images. However, there exist difficulties analyzing the phase information due to inherent phase instability contributed by external mechanical perturbations. Heterodyne detection is highly sensitive to mechanical motions, and phase noise makes the interpretation of the heterodyne power spectral density challenging. Many methods have been proposed to stabilize the phase information of functional images by introducing complicated optical set-ups [9-11]. Here we describe a stabilized and sensitive Doppler power spectrum through a method that acquires a probability density function (PDF) of Doppler phase displacements. This provides an intuitive dynamic picture of the target, and the Doppler power spectral density derived from the PDF shows greater sensitivity and stability than the conventional heterodyne power spectrum. Furthermore, changes in the PDF shape induced by bacterial infections of epithelial cells demonstrates pathogenic bacterial dynamics characterized by random-walk models with anomalous ballistic motions.

5.2 Dynamic Light Scattering: Homodyne and heterodyne detection

Biodynamic imaging (BDI) uses a digital holographic low-coherence Mach-Zehnder interferometer to measure broadband Doppler spectra induced by DLS inside a living tissue sample (Figure 5.1 (a)). Digitally reconstructed dynamic speckle from a holographic image at the Fourier plane (FP) has intensity and phase information. A power spectrum of the broadband Doppler signal is obtained by performing a temporal Fourier transform on an intensity time series. The power spectrum obtained from the temporal intensity information is defined as a homodyne power spectrum as

$$S_{\text{hom}}(\omega) = \left| \int I(t) e^{i\omega t} dt \right|^2 \quad (5.1)$$

where I is the intensity time series. The power spectrum from Eq. (5.1) does not include the phase information. The phase of functional images can further represent the intracellular dynamics of the sample. A heterodyne power spectrum incorporates the phase information by performing temporal Fourier transforms on complex-valued fields by

$$S_{\text{het}}(\omega) = \left| \int E(t) e^{i\phi(t)} e^{i\omega t} dt \right|^2 \quad (5.2)$$

where $E(t)$ and $e^{i\phi(t)}$ are the time series of amplitude and phase values of the complex-valued electric field of the digitally reconstructed holograms (Figure 5.1 (a)).

5.3 Calibration Experiments

5.3.1 Vertically Moving Paper

For calibration, a circular-shaped paper sheet with a 3 mm radius and 15 μm thickness was prepared. The paper floated on a water reservoir surface and vertically moved toward the bottom of the reservoir caused by water surface evaporation. The evaporation speed was measured to be about 10 mm/day which corresponds to around 0.1 $\mu\text{m/s}$. While the paper is vertically moving, the low-coherence light illuminates the paper and an interference pattern is formed at the Fourier plane by matching the optical path difference between the object and reference arms to within the coherence length (~ 20 mm) of the optical source. The evaporation speed is constant and the vertical motion induced by the evaporation is steady, giving the power spectral density in Figure 1(b) a Doppler peak.

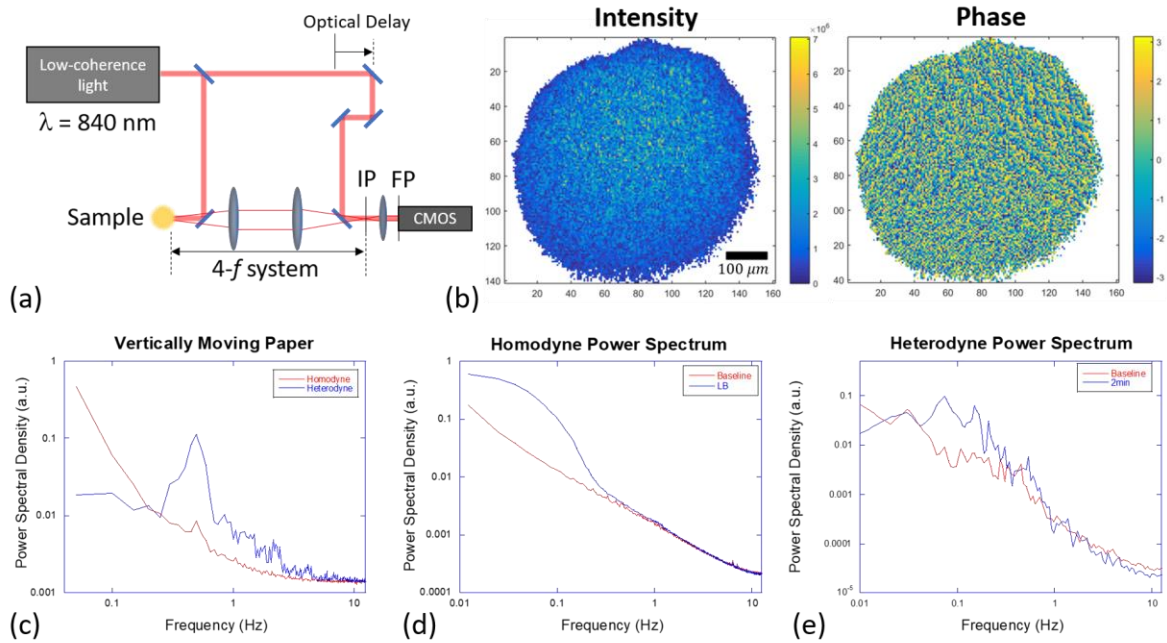


Figure 5.1 Calibration experiments of the power spectra of dynamic speckle. (a) Schematic diagram of BDI and (b) reconstructed hologram intensity and phase at a fixed time. Speckle formed at the image plane (IP) is Fourier transformed to the Fourier plane (FP). (c) Homodyne and heterodyne power spectra of the vertically moving paper due to the water surface evaporation. A Doppler peak appears in the power spectrum of the sinking paper at 0.45 Hz, which corresponds to a settling speed of 150 nm/s. (d) Homodyne power spectral density enhancement of *Escherichia coli* (*E. coli*) pellet by applying the Lysogeny broth (LB) medium shows a prominent Doppler edge, (e) while the heterodyne power spectra cannot detect the Doppler edge.

The characteristics of homodyne and heterodyne power spectra are compared in Figure 5.1. The homodyne and heterodyne power spectra of the vertically moving paper were measured (shown in Figure 1(c)). When the paper was at the coherence-gated depth, holographic dynamic speckle was recorded with 25 fps for 20 seconds (bandwidth 0.02 Hz to 12.5 Hz). Fourier transformation on the 500-frame intensity time series has 249 positive and negative non-zero frequency components and one DC component at $\omega = 0$. Positive and negative non-zero Fourier components are symmetric for a homodyne power spectrum, and the positive components are plotted in Figure 1 (c). The heterodyne power spectrum has an asymmetric shape because the dynamics of the vertically moving paper is biased. The heterodyne power spectrum of the negative Fourier components containing the Doppler peak was plotted. The homodyne power spectrum shows a clear peak at 0.45 Hz, which corresponds to a speed of 150 nm/sec for the moving paper. On the other hand, the homodyne spectrum shows only a “residual” Doppler peak.

5.3.2 Bacterial Dynamics

Homodyne and heterodyne power spectra of bacterial chemotaxis-induced swarming are demonstrated in Figure 1(d) and (e). BDI depth scanning can measure the Doppler power spectra of bacterial swarms driven by chemotaxis of more than a million bacteria in real-time. The statistical characteristics of bacterial swarms were analyzed by measuring the Doppler edge frequency which is caused by 3-dimensional ballistic motion with long persistence times [5]. To measure the 3-dimensional bacterial swarm induced by chemotaxis, a dense *Escherichia coli* (*E. coli*) high-bacterial-density pellet (10^{10} CFU/mL) was extracted from a culture medium (10^8 CFU/mL) by centrifugation (15000 rpm for 3 min). The pellets were dipped in 300 mL of 1% NaCl solution for 5 hours to establish *E. coli* in the stationary state. To induce a nutrient shock and chemotaxis, 150 mL of the medium was removed and added to 150 mL of the Lysogeny-broth (LB) medium. The Doppler signals of *E. coli* pellets were measured by BDI before and after applying the LB medium, and 2048 holograms were recorded per measurement with the sampling frequency of 25 fps. The collective motion of *E. coli* after applying the LB medium was observed by the homodyne detection method in Figure 5.1(d). A prominent Doppler edge appeared immediately after applying the LB medium, while the heterodyne detection spectra did not show a measurable power spectral enhancement in Figure 5.1(e). The Doppler edge shown in Figure 5.1(d) represents 3-dimensional persistent motion. The frequency of the maximum spectral density enhancement by the nutrient shock represents the inverse characteristic time τ_c of the persistent motion [5], which is related to the average speed of the bacterial swarm along the vertical direction as

$$\frac{1}{\tau_c} = \mathbf{q} \cdot \mathbf{v} \quad (5.3)$$

As shown in Figure 5.1(c), heterodyne detection on the slowly moving paper shows much better sensitivity. However, the higher sensitivity often becomes a disadvantage if phase stabilization of the measurement system was not achieved. The contrast of spectral shape changes shown in Figure 5.1(d) and (e) demonstrates the disadvantage of heterodyne detection. While the homodyne power spectra show a Doppler edge, the heterodyne spectra do not.

5.4 Phase-Sensitive Detection

The dynamic characteristics of random processes can be characterized as diffusive or ballistic. Biological processes have more ballistic characteristics due to active transport such as molecular motors, intracellular undulations, cell crawling, etc. Doppler shifts produced by scattering from biological systems carry the characteristics of ballistic phase displacements. However, the phases of scattered photons also carry random phase excursions caused by external mechanical perturbations, diffusive background, and optical phase drifts which disturb the heterodyne power spectral densities of Doppler signals as shown in Figure 5.1(e). The advantage of obtaining the temporal PDF uses the characteristics of ballistic motions which have persistent lengths and times. The time evolution of the PDF demonstrates both persistent phase displacement and phase noise excursions in terms of the temporal shift of maximum likelihood and the temporal width-broadening of PDF, respectively. Random processes with different dynamic characteristics are shown in Figure 5.2. Systems with diffusive characteristics (Figure 5.2(a), 3D isotropic) and ballistic (Figure 5.2(b), 1D isotropic or 3D ballistic) induce different Doppler shifts and speckle formation has different phase displacement statistics. The analysis of the phase displacement statistics and the extraction of ballistic characteristics of the Doppler shift will be demonstrated by introducing PDFs.

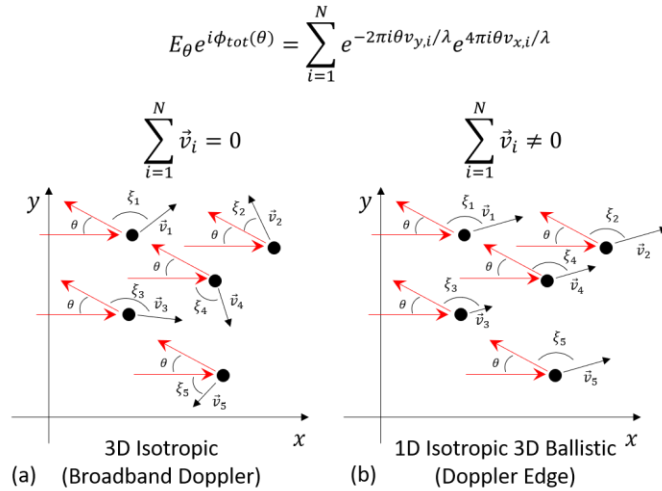


Figure 5.2 Schematic diagram of dynamic light scattering. The total phase value ϕ_{tot} is determined by contributions of N identical photons with slightly different phases. Black and red arrows represent the average velocities of scattering elements over the sampling window (40 ms) and wave vectors of scattered photons, respectively. When photons interact with (a) 3D random isotropic dynamic particles, the average phase displacement of the Doppler shift per sampling window becomes zero. (b) On the other hand, when the dynamic particle has 3D ballistic dynamics or 1D isotropic motion, the average phase displacement of the Doppler shift has a non-zero value.

5.4.1 Phase Displacements and Probability Density Function (PDF)

Reconstructed dynamic speckle at the Fourier plane (FP) produces a functional image that contains Doppler information. The phase of reconstructed holograms is limited to values between $-\pi$ to $+\pi$ radian, and the time series of the phase often drifts through external phase noise. As previously demonstrated in Figure 5.1(e), the heterodyne power spectrum cannot demonstrate spectral enhancement when phase stabilization has not been achieved. An alternative approach finds the drifting phase of individual pixels within specified times and constructs a probability density function (PDF) of phase displacements. The PDF of phase displacements shows the characteristics of the dynamics of the sample. Two different dynamic characteristics were assumed in Figure 5.2. 3D isotropic motion produces a power-law Doppler power spectral density. When motion is 1D isotropic or 3D ballistic, then the Doppler power spectral density has a Doppler edge. For instance, when bacteria are in the stationary state, the Doppler power spectrum has 3D isotropic motion characteristics (Figure 5.2(a)). When DLS occurs with 3D isotropic dynamic particles that have a short persistence time, the averaged phase displacement with the sampling window (40 ms) is zero ($\Delta\phi_{\text{tot}} = 0$) which means the shape of the PDF is symmetric. However, when light is scattered by persistently moving particles as shown in Figure 5.2(b), the phase displacement per sampling window has a non-zero averaged phase displacement. The phase of randomly interfering photons can be described as,

$$Ae^{i\phi_{\text{tot}}} = \sum_{n=1}^N e^{i\phi_n} \quad (5.3)$$

where A is an arbitrary amplitude after vector summation in Figure 5.2. A photon with wavevector \mathbf{q} scatters from a scattering element at \mathbf{r} contributing to the phase angle and is assumed to have isotropic Doppler shifts. The average Doppler shift can be expressed as

$$\phi_{\text{tot}}(\mathbf{r}, t) = \phi_{\text{geo}} + \mathbf{q}(\mathbf{r}) \cdot \mathbf{v}t \quad (5.4)$$

where ϕ_{geo} is a global phase angle determined by a geometric factor of scattering elements. The geometric contribution is static when we assume the distribution of the scattering elements does not change rapidly. On the other hand, the Doppler frequency shift contribution to phase is on the time term, so the time derivative of $\phi_{\text{tot}}(\mathbf{r}, t)$ contains the total contribution from Doppler shifts. As a result, the time-averaged total Doppler shifts contributing to speckle phase can be defined as

$$\Delta\bar{\phi}(\mathbf{r}, \tau) = \int_0^\tau \frac{\partial\phi(\mathbf{r}, t)}{\partial t} dt \quad (5.5)$$

To avoid the phase wrapping problem, the phase displacements were acquired by $e^{i\Delta\phi} = e^{i(\phi_f - \phi_i)}$ between consecutive reconstructed holograms. The phase time series $\phi(\mathbf{r}, \tau)$ of the functional images are reconstructed by adding $\Delta\phi(\mathbf{r}, \tau) = \tan^{-1} \left[\frac{\text{Im}(e^{i\Delta\phi(\mathbf{r}, \tau)})}{\text{Re}(e^{i\Delta\phi(\mathbf{r}, \tau)})} \right]$ to the previous frame.

5.4.2 Probability Density Function (PDF) of Phase Excursions

The phase of dynamic speckle varies with time, and experimentally acquired PDFs show a stable distribution (Figure 5.3). The PDF of dynamic speckle phase variance introduces phase-sensitive detection to the dynamic characteristics of a specimen. The phase difference from Eq. (5.4) and (5.5) is

$$\frac{\Delta\phi}{\Delta t} = \mathbf{q} \cdot \mathbf{v} \quad (5.6)$$

and the phase displacement by N dynamic scattering elements contributing to the Doppler shift can be estimated by

$$\frac{\Delta\phi}{\Delta t} = \sum_{i=1}^N qv_i \cos \xi_i \quad (5.7)$$

where v_i and ξ_i are the velocities, respectively. The experimentally measured time-averaged phase displacement ($\Delta\bar{\phi}$) over a sampling window ($\Delta\tau$) becomes

$$\Delta\bar{\phi} = \sum_{i=1}^N q\Delta x_i \cos \xi_i \quad (5.8)$$

Here, the time-averaged displacement $\Delta\bar{x}_i$ of the i th dynamic particle should be a non-zero value to contribute to the phase shift. When the persistence time of the dynamic particle is shorter than the sampling window, or the particle's dynamics are intrinsically diffusive, then the time-averaged Doppler shift induced by the time-averaged dynamics vanishes. The probability of $\Delta\bar{\phi}_i$ and Δx_i has the relation

$$P(\Delta\bar{\phi}_i) = \frac{\Delta x_i \cos \xi_i}{\sum_{i=1}^N \Delta x_i \cos \xi_i} \quad (5.9)$$

which ensures that the PDF measures the net Doppler shifts contributed by dynamic particles. Also, the averaged phase displacement $\Delta\bar{\phi}$ derived from a PDF represents an average persistence length $\Delta\bar{x}$ of the dynamic particles. When an external noise contributes to the PDF, it contributes to the width of the PDF, while the expectation value of the average phase displacement $\Delta\bar{\phi}$ remains constant. For instance, mechanical oscillations or optical source noise can perturb the average $\Delta\bar{\phi}$ between two consecutive frames, but the effect vanishes by taking a time average over many frames due to the zero-mean noise characteristic [12].

5.4.3 Calibration with Macroscopic Directed Motion

To obtain a PDF from functional images, the statistical phase displacements of the functional images from the experiment conducted in Figure 5.1 were acquired. The schematic diagram of the temporal phase information is shown in Figure 5.3(a). A phase displacement distribution can be acquired by subtracting two frames with the time interval τ , and the normalized histogram of the phase displacement represents the probability density function. The PDF of the phase displacement of the time interval τ is obtained by

$$PDF(\tau) = \frac{1}{N} \sum_{t=1}^N \sum_{x,y} histogram[\phi(\mathbf{r}, t + \tau) - \phi(\mathbf{r}, t)] \quad (5.10)$$

The statistics of $\Delta\phi$ are collected over the dynamic speckle, and the spatial information (x and y) is lost during this procedure. The temporal evolution of the PDF is shown in Figure 5.3(b) and (c). The stationary paper has phase noise contributions from the optical source, mechanical vibrations, and detector noise, and the Gaussian distribution is shown in Figure 5.3(b). The vertically moving paper has persistent motion and the optical measurement captures the Doppler signal caused by the vertical dynamics and the background noise simultaneously. Here the Doppler slope is defined as an averaged phase displacement $\Delta\bar{\phi}$ per time delay t which can be obtained by

$$\frac{\Delta\bar{\phi}}{\tau} = \frac{1}{\tau} \sum_{\Delta\phi=-\pi}^{\pi} \Delta\phi PDF(\Delta\phi) \quad (5.11)$$

The sign of the phase was set to be positive for upward and negative for downward, so the PDF with different t in Figure 5.3(c) shows the negative Doppler slope in Figure 5.3(f).

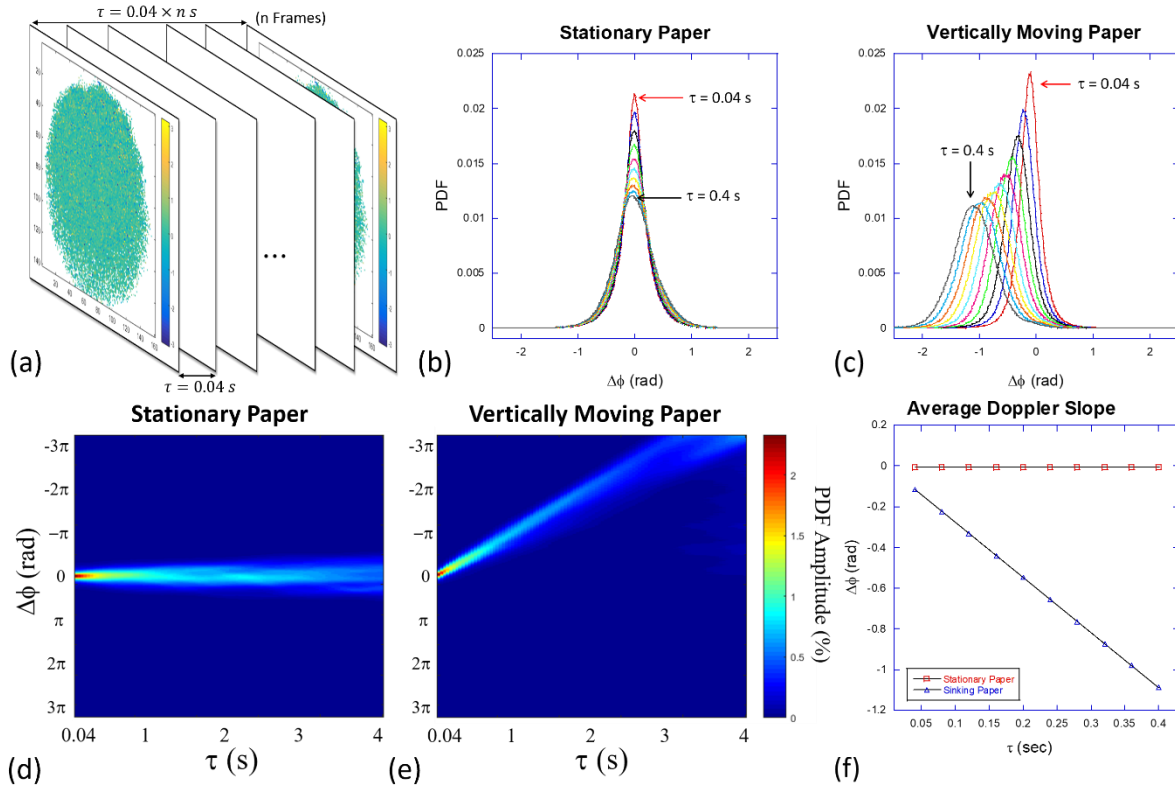


Figure 5.3 Doppler information acquisition from functional images. (a) Schematic diagram of phase information time series of dynamic speckle. $PDF(\tau)$ is obtained from the subtraction between frames with a τ difference and histogrammed. PDFs of (b) stationary paper and (c) slowly moving paper in Figure 5.1 (b) and the corresponding 2D PDF representations of (d) stationary paper and (e) moving paper. The Doppler slope of the average displacement $\overline{\Delta\phi}$ shown in (f) with different time intervals in (c) is 2.70 rad/s which corresponds to 0.43 Hz and 143 nm/s by Eq. 5.6. The Doppler peak of the power spectrum in Figure 5.1(b) and the average phase displacement of the PDF show good agreement.

Both of the amplitudes of PDF shown in Figure 5.3 (b) and (c) decreased because of the optical decoherence [12]. However, the time-averaged speed of the slowly moving paper can be estimated from $\overline{\Delta\phi}$. The speed of the paper was estimated to be 143 nm/s which is consistent with the power spectral Doppler peak frequency in Figure 5.1(b).

5.4.4 PDF of Bacterial Swarms Induced by Nutrient Shock

The nutrient shock of bacterial pellets induced by chemotaxis showed prominent Doppler shifts in the homodyne spectra in Figure 5.1(c). The same method used for obtaining the PDF in Figure 5.3 was used to obtain the chemotaxis PDFs of *E. coli* pellets. The time evolution of the PDF showed non-zero phase displacement immediately after adding a nutrient. Equal volumes (150 mL) of reagents were added to the wells (medium was subtracted and re-added to the same well to test the pipetting-perturbation effect) and 1% and 7% NaCl media were used to verify the effect of applying medium without nutrient and to test osmotic pressure of the LB medium without nutrient components. The sign of the phase was calibrated by the moving paper experiment from Figure 5.3 and set a positive direction for upward, and negative direction for downward. The baselines were measured 3 times for 6 minutes while the *E. coli* pellet was in a stationary state. After applying reagents, responses were measured 13 times for 26 minutes. The temporal evolution of PDFs immediately after applying reagents are shown in Figure 5.4. (a) and (b). The average Doppler slopes from each measurement are shown in Figure 5.4 (c). The average Doppler slope showed immediate responses after applying reagents then decays exponentially. The temporal decay coefficients α and amplitudes of the average Doppler slopes are shown in Figure 5.4(c) and summarized in Table 5.1.

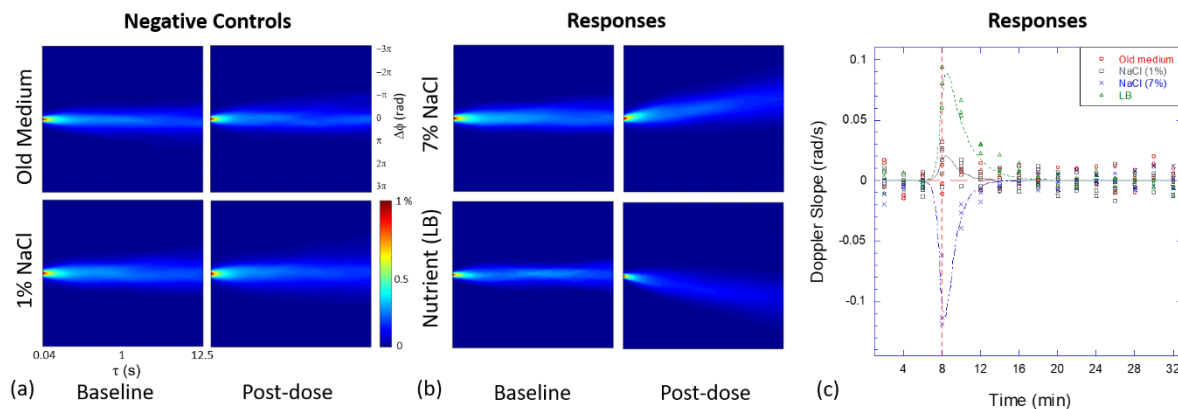


Figure 5.4 Temporal evolution of PDFs of *E. coli* pellets and Doppler slopes. (a) Temporal response of PDFs immediately after applying negative-control reagents (perturbed medium with a pipette and adding 1% NaCl medium) and (b) high-osmotic pressure solution (7% NaCl), and nutrient (LB). (c) Doppler slopes from PDFs. One data point represents a single measurement. Applying medium (pipetting perturbation) and 1% NaCl solution (LB medium base without nutrient compound) did not induce significant shifts. 7% NaCl (osmotic shock) and LB (nutrient shock) media showed shifts of PDFs with opposite signs.

Table 5.1 Response characteristics to different reagents.

Reagent	α (t^{-1})	Maximum Doppler Slope Amplitude (rad/s)	Average velocity (nm/s)
Old Medium	N.A.	N.A.	N.A.
NaCl (1%)	0.53 ± 0.41	0.05 ± 0.04	2.6 ± 2.2
NaCl (7%)	0.59 ± 0.06	-0.31 ± 0.1	-15.4 ± 5
LB	0.26 ± 0.06	0.25 ± 0.05	13 ± 3

The Doppler slope measurements on *E. coli* pellets after applying various reagents showed different characteristics. Applying 1% NaCl solutions showed the slowest speed (2.6 nm/s). In the case of applying 7% NaCl solutions, it induced a net motion in the negative direction (downward) with the fastest speed (15.4 nm/s). The motions of *E. coli* induced by 1% and 7% NaCl solutions showed similar decay coefficients. The LB medium induced an intermediate speed, and the motion lasted about twice longer than applying NaCl solution. The pipetting perturbation of the *E. coli* pellet was not measurable.

5.4.5 Stabilization of the Heterodyne Doppler Spectrum

The time evolution of a PDF is equivalent to the temporal correlation of the Doppler shift. The experimentally-obtained PDF becomes stable while averaging the phase displacement distribution. Therefore, the reconstruction of the power spectral density from a PDF should have a more stable Doppler spectral density. The autocorrelation of a field with a time interval τ can be estimated from a PDF by calculating the expectation value of $e^{i\Delta\phi}$ which can be denoted as

$$AC(\tau) = E^2 \sum_{\Delta\phi} PDF(\Delta\phi(\tau)) e^{i\Delta\phi(\tau)} \quad (5.12)$$

by assuming the field amplitude varies more slowly than the phase displacement $\Delta\phi(\tau)$. The stabilized heterodyne power spectrum of the signal can be obtained by performing a Fourier transform on $AC(\tau)$ by the Wiener-Khinchin theorem [13].

$$S_{het}(\omega) = \int AC(\tau) e^{i\omega\tau} d\tau \quad (5.13)$$

From the PDF of the vertically moving paper (Figure 3(e)) and the *E. coli* pellet (Figure 5.4(b)), the autocorrelation and the corresponding power spectrum were obtained and shown in Figure 5.5.

The Fourier transform of the autocorrelation has a limited time window due to the limited sampling bandwidth (0.02 Hz ~ 12.5 Hz). The sampling time window is 20 sec and the AC shown in Figure 5.5(b) has a limited time window from -10 sec to 10 sec. The spectrum obtained from the autocorrelation has a similar spectral shape to the heterodyne detection spectra in Figure 5.5(c). The heterodyne power spectrum of vertically moving paper shows about 50 times enhanced detection sensitivity compared to the conventional heterodyne power spectrum by suppressing the phase noise through the PDFs. The raw heterodyne power spectrum did not display the Doppler edge shown in Figure 5.5(d). But the heterodyne power spectra derived from the PDFs show prominent Doppler edges in Figure 5.5(f). Although there exist aliasing effects due to the limited $\Delta\phi$ domain of the histograms, the low-frequency spectral components illustrate much better heterodyne spectral enhancement than the raw heterodyne spectra. Also, the homodyne spectrum is always symmetric which means the spectrum cannot distinguish the signs of dynamics, but the refined heterodyne power spectrum shows well-characterized heterodyne power spectral enhancement including the sign of dynamics as shown in Figure 5.5(c).

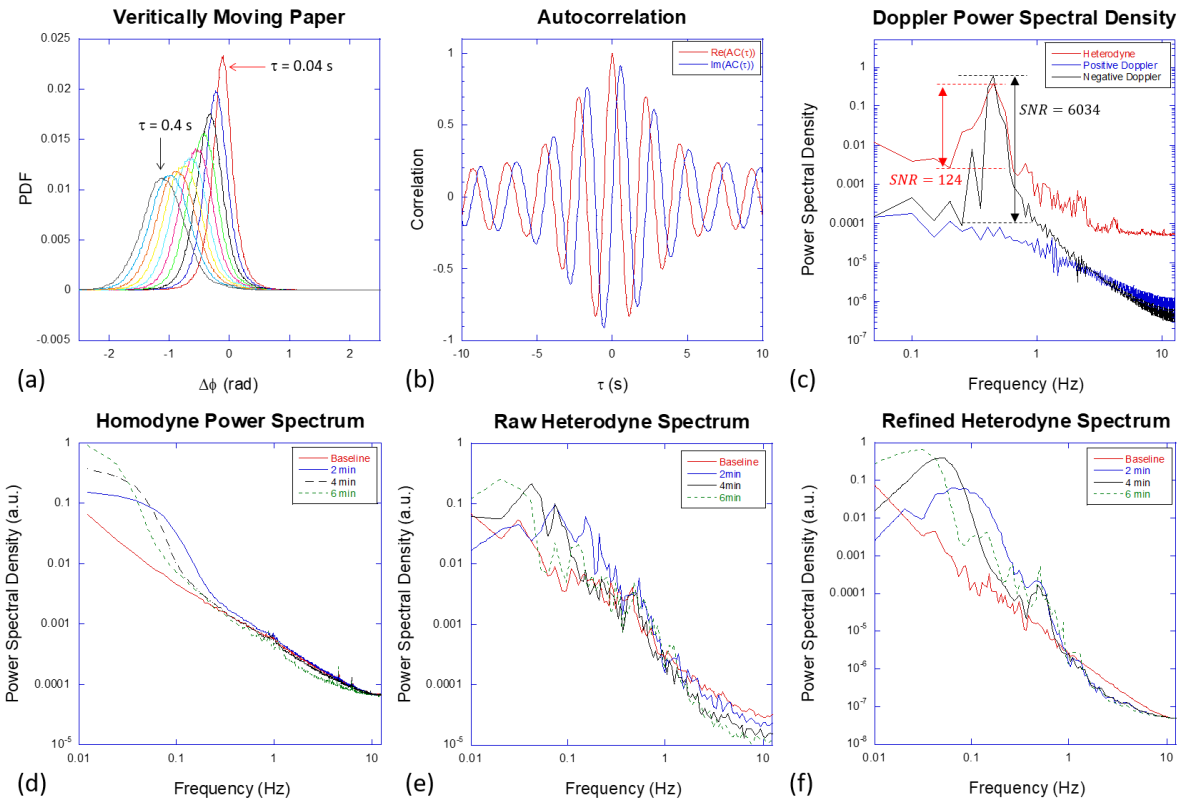


Figure 5.5 (a) PDF of the vertically moving paper from Figure 5.3 (b) Autocorrelation (AC) obtained from (a) by Eq. (5.12). The AC of negative time is the complex conjugate of positive time, so the real valued AC is symmetric and the imaginary valued AC is asymmetric. (c) The power spectrum derived from the complex autocorrelation by the Weiner-Khinchin theorem and compared with the heterodyne spectrum. Positive and negative spectral components are compared. (d) Homodyne power spectrum of nutrient shock applied to an *E. coli* pellet and (e) the raw heterodyne power spectrum. (f) Heterodyne power spectrum derived from PDFs in Figure 5.4(b). For the relative spectral density comparisons, all Nyquist floors were calibrated to have the same values at 12.5 Hz.

5.5 Levy Stable Distributions

The dynamics of scattering elements may have Levy-flight-like anomalous occasional ballistic motions [14-16]. DLS with Levy-flight particles can have large random phase excursions with low probability which can form power-law tails. The slope of the power-law tails represents the frequency of the occasional ballistic motions. Probability distributions can have power-law behavior at large values of the random variable. For instance, the probability in the tail may behave as [17]

$$P(|x|) \propto \frac{1}{|x|^{1+\alpha}} \quad (5.14)$$

Such distributions are said to have *heavy tails* because the probability falls more slowly than exponential for large arguments. Heavy tails on a distribution cause rare but high-amplitude events that are referred to as outliers and sometimes as “black swans” [18]. These events are fundamentally part of the distribution and are not anomalies, but can have a disproportionate effect when attempting to calculate variances or even mean values. For instance, there is a large class of probability distributions for which the variance and high-order moments are infinite. A subset of such distributions includes stable distributions.

In probability theory, a class of distributions is called *stable* if a sum of two independent random variables that come from a distribution have the same distribution. The normal (Gaussian) distribution has this property because the sum of two normally distributed independent variables is also normally distributed. The variance and possibly the mean may be different, but the functional form is still Gaussian.

The general form of a probability distribution can be obtained by taking a Fourier transform as

$$P(x) = \frac{1}{2\pi} \int_{-\infty}^{\infty} \varphi(k) e^{-ikx} dk \quad (5.15)$$

where $\varphi(k)$ is known as the *characteristic function* of the probability distribution. A special case of a stable distribution is the Lévy symmetric stable distribution obtained as [17]

$$P_{\alpha,\gamma}(x) = \frac{1}{\pi} \int_0^{\infty} e^{-\gamma q^\alpha} \cos(qx) dq \quad (5.16)$$

and characterized by the parameters α and γ . The characteristic function, in this case, is a stretched exponential. The Lévy distribution has a power-law tail at large values, given by Eq.(5.14), but for smaller values has a characteristic length scale set by the parameter γ . The special case of the Lévy distribution for $\alpha = 2$ is a normal distribution. The special case of the Lévy distribution for $\alpha = 1$ is the Cauchy distribution given by

$$P_{1,\gamma}(x) = \frac{1}{\pi} \frac{\gamma}{\gamma^2 + x^2} \quad (5.17)$$

The Cauchy distribution is normalizable (probabilities integrate to unity) and has a characteristic scale set by γ , but it has a divergent mean value, violating the central limit theorem. For distributions that satisfy the central limit theorem, increasing the number of samples from the distribution allows the mean value to converge on a finite value. For the Cauchy distribution, on the other hand, increasing the number of samples increases the chances of obtaining a black swan, which skews the mean value to larger values as the mean value diverges to infinity in the limit of an infinite number of samples.

Examples of Levy stable probability distribution functions are shown in Figure 5.6 for a range between $\alpha = 1$ (Cauchy) and $\alpha = 2$ (Gaussian). The heavy tail is seen even for the case $\alpha = 1.99$ close to the Gaussian distribution. In the case of the Gaussian distribution, the mean-squared displacement is finite. However, for all other cases, the mean-squared displacement is divergent, caused by the large path lengths that become more probable as α approaches unity.

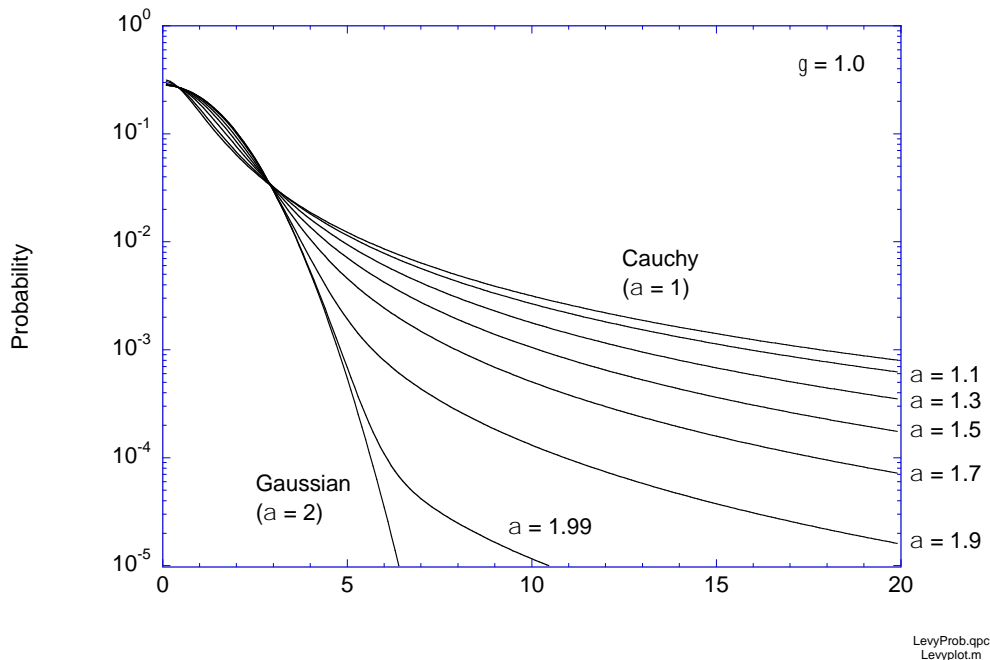


Figure 5.6 Levy stable probability distribution functions between $\alpha = 1$ (Cauchy) and $\alpha = 2$ (Gaussian). The heavy tail is seen even for $\alpha = 1.99$ close to the Gaussian case.

Stable distributions with divergent moments play important roles in biology. For instance, a random walk with a Levy distribution of path lengths, known as a Levy flight, can be an efficient means for an organism to search for food [16, 19]. They also can participate in intracellular transport processes. Waiting times can have stable distributions as well as path lengths. The sampling of these processes from stable probability distributions is one way that anomalous transport emerges in intracellular motion.

5.6 Levy Spectroscopy

The PDF represents the statistical characteristics of the random process associated with scattering elements. The phase displacements $\Delta\phi$ have a one-to-one correspondence to the displacements Δx of the scattering elements by Eq. (5.8). Fitting the shape of the PDF with the Levy distribution of Eq.(5.16) may help display the anomalous ballistic characteristics of scattering elements. To reduce the external phase noise contribution to the shape of the PDF, the smallest sampling window τ_{\min} was used to analyze the statistical characteristics of $PDF(\tau_{\min})$. Analysis of the power-law tails requires a large sample size because the characteristics of power-law tails depend on the decaying tendency of rare probabilities. The size of the functional image is about 10^4 pixels and the images were recorded for more than 2000 frames. Therefore, the statistics of the PDF were established on about 10^7 samples of experimental measurements. The PDF of $\Delta\phi$ spanned from $-\pi$ to π radian with a resolution of 0.01 radian. Various PDFs were analyzed in terms of Levy α values in Eq.(5.16).

5.6.1 Levy-like Characteristics of PDFs

Calibration experiments were analyzed by Levy alpha spectroscopy. The Levy fits of the PDFs of the stationary paper, sinking paper, tumor spheroids, and *E. coli* pellets are shown in Figure 5.7. The PDF of stationary paper showed a Levy alpha close to 2 which represents the Gaussian phase noise of the optical source. The moving paper from Figure 5.1(b) shows a slightly decreased alpha contributed by the mechanical motion, but the alpha is still close to 2. The biological objects, such as tumor spheroids and an *E. coli* pellet, showed a Levy alpha less than 1.6 which are more Cauchy-like and may be related to ballistic random-walks observed in biological systems [14-16].

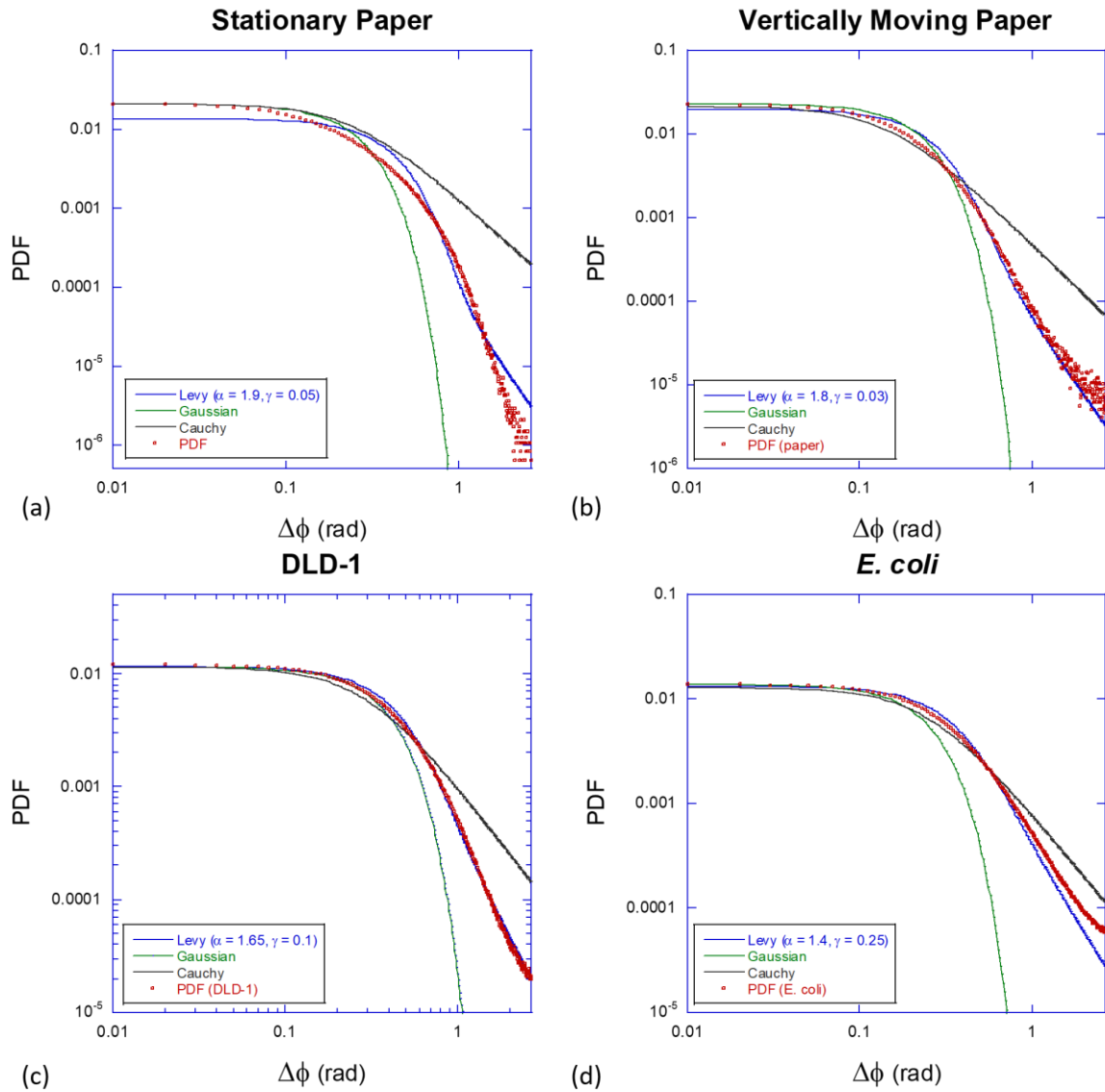


Figure 5.7 PDFs of various targets fitted with Levy, Gaussian, and Cauchy distributions of (a) stationary paper, (b) vertically moving paper, (c) DLD-1 spheroids, and (d) *E. coli* pellet. The Cauchy probability density shows power-law tails with $a = 1$ (black solid lines) and the Gaussian probability density with $\alpha = 2$ (green solid lines). Levy distributions show similar heavy tails of experimentally obtained PDFs'. The power-law tails of Levy probability densities are numerically obtained and fitted with the smallest residual squares. To quantify the slopes of the power-law tails, the maximum likelihoods of PDFs are shifted at $\Delta\phi = 0$ to plot symmetrically.

5.6.2 Bacteria and Host-cell Selection and Preparation

Foodborne pathogens have various infection mechanisms. For instance, *L. monocytogenes* target epithelial cells and infiltrate host-cells by physically penetrating cell walls. After internalization, *L. monocytogenes* synthesizes actin tails by using host-cell resources to gain a propulsion force toward neighboring host-cells [20, 21]. The spreading infection goes beyond diffusion [21], and the spreading speed may be governed by the rare-outliers which is a key characteristic of Levy flights. On the other hand, *Listeria innocua* (*L. innocua*) are from the same *Listeria* genus, but *L. innocua* do not have an effective infection mechanism [22]. The interaction of *L. innocua* with host-cell is passive and opportunistic compared to *L. monocytogenes* [23].

L. monocytogenes and *L. innocua* were cultured in an LB medium for 24 and 48 hours, respectively, at 37 degrees Celsius to reach 10^8 CFU/ml. For host-cell preparation, DLD-1 (Epithelial adenocarcinoma cell line) was selected which has 3-dimensional tissue characteristics and loose cellular structure for observing rapidly spreading infection. The seed cells (American Type Culture Collection) were cultured in RPMI-1640 medium with 25 μ M HEPES buffer (Gibco), 10% fetal bovine serum (Atlanta Biologicals) and antibiotics (100 U/ml Penicillin and 100mg/ml streptomycin) for 4~5 days. When DLD-1 forms the multicellular spheroids structure, they were transferred to a 96-well BioCoat plate (Corning) with an antibiotic-free RPMI-1640 medium (300 ml/well). After DLD-1 transfer, the media were refreshed with RPMI-1640 without antibiotics.

5.6.3 Infection Assay

The infection assay using DLD-1 spheroids was analyzed using Levy alpha spectroscopy of the PDF. Interaction between bacteria and DLD-1 should change the statistical characteristics of scattering elements due to the inoculated bacterial dynamics. Also, the different strategic behaviors of *L. monocytogenes* related to *L. innocua* are expected to produce different PDF shapeshifts where *L. monocytogenes* actively interact with DLD-1 host-cells and show more ballistic behaviors. Before applying bacteria to DLD-1, 3 baselines were measured for 90 minutes. After the baselines were established, 10^7 CFU of *L. monocytogenes* or *L. innocua* were inoculated for the infection cohort and growth medium for the control cohort, respectively. The dynamic speckle of the two cohorts were measured for 6 hours. The PDF of each DLD-1 was obtained to compare the Levy

alpha values of baselines and infection measurements. The initial Levy alpha values can vary due to DLD-1 characteristics, and 3 Levy alpha values of baseline measurements were averaged. After inoculation, the shifts of Levy alpha values were obtained. The group inoculated by *L. monocytogenes* showed significantly decreased alpha values (more outliers), while *L. innocua* showed only a small change. The PDF of DLD-1 before and after infection are compared in Figure 5.7(a) and (b). Decreased alpha value suggests that the mechanical behavior of random processes become more Cauchy-like (ballistic) than Gaussian-like (diffusive) after bacterial inoculation.

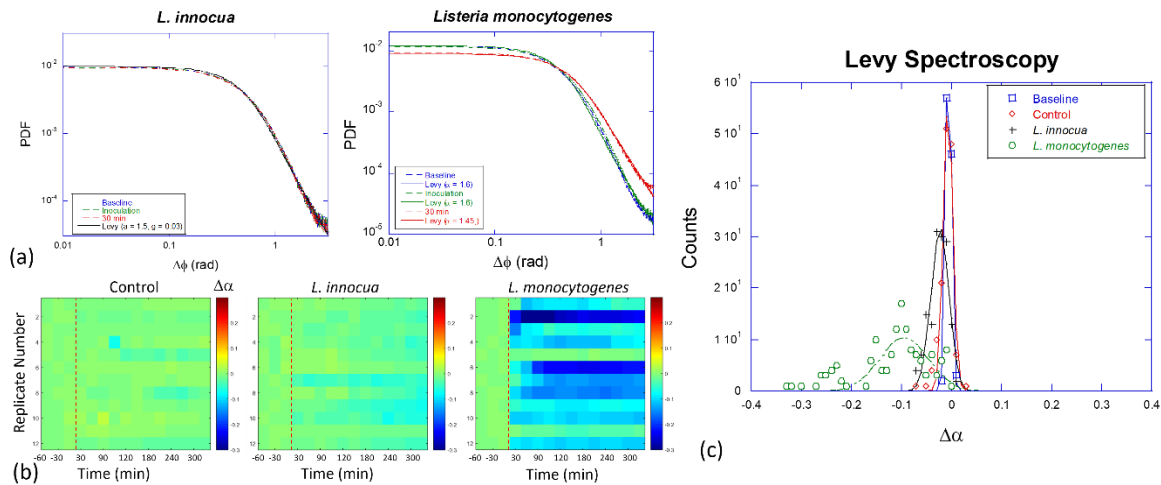


Figure 5.8 Levy Alpha spectroscopy infection assays. Two bacterial strains with the same genus with different pathogenicities were inoculated into DLD-1. (a) Examples of PDF and Levy distribution comparison. *Listeria innocua* (*L. innocua*) induces a slight change in the Levy alpha while *Listeria monocytogenes* (*L. monocytogenes*) significantly decreased the Levy alpha. (b) Statistical analysis of the Levy alpha value change ($\Delta\alpha$) of 12 replicates. Bacteria were inoculated at 60 min (Red-dashed line) and PDFs were measured for 6 hours. The Levy alpha changes of the control and the *L. innocua* infection group showed comparable variations, while *L. monocytogenes* showed a significant decrease in the alpha. (c) The histogram of Levy alpha value spectroscopy, collected from Figure 8(b). Invasive *L. monocytogenes* induces Levy-alpha shifts while passive *L. innocua* shows only a minor shift on the average Levy-alpha value. Control and baselines showed almost identical statistical behaviors. Lines are fitted Gaussian distributions.

The statistical separations of Levy alpha shifts are shown in Figure 5.8(c). Baselines of all cohorts showed a stable distribution and the variance of Levy alpha values shows almost identical overlap with the control. Inoculation by *L. monocytogenes* and *L. innocua* showed negative shifts due to bacterial dynamics. The average Levy alpha shifts are shown in Table 5.2.

Table 5.2 Levy Alpha Spectroscopy of Bacterial Infections.

	Baseline	Control	<i>L. innocua</i>	<i>L. monocytogenes</i>
$\Delta\alpha$	-0.005 ± 0.006	-0.01 ± 0.01	-0.03 ± 0.02	-0.11 ± 0.07

The baselines were measured for 90 minutes. The control also showed a stable distribution over a 6-hour measurement. *L. monocytogenes* has the largest variance due to the characteristics of the infection. The scanned area of DLD-1 may have fully infected regions, partially infected regions or may be isolated from infection. Therefore, the structural heterogeneity may produce larger variations. *L. monocytogenes* potentially can generate larger shifts of Levy alpha compared to *L. innocua* whose interaction with epithelial cells is known to be more passive.

5.7 Conclusions

Statistical analysis of the phase-sensitive detection method of Doppler shifts by DLS has been demonstrated. Comparisons between the calibration experiments and the phase-sensitive detection method showed good agreement and improved stability compared to the conventional heterodyne detection method. By introducing statistical averaging on the time-delayed phase displacement, the random phase noise could be canceled while the net Doppler shift by ballistic motions remains detectable which improves the detection sensitivity. Furthermore, the probabilistic analysis of the phase displacement showed an anomalous ballistic distribution which is close to the Levy distribution. The Levy alpha values of PDFs were obtained numerically, and shifts of the Levy alpha values by bacterial infection were measured. Invasive bacterial infection of DLD-1 showed significantly decreased Levy alpha values while the control group and the group inoculated by non-pathogenic bacteria showed only a slight change in the alpha. The PDF drift induced by pathogenic bacteria inoculation showed more Cauchy-like (ballistic) statistics than Gaussian-like (diffusive) statistics. PDF shapeshifts caused by invasive bacterial infection may provide a statistical representation of infection[24].

5.8 References

- [1]. D. Huang, E. A. Swanson, C. P. Lin, J. S. Schuman, W. G. Stinson, W. Chang, M. R. Hee, T. Flotte, K. Gregory, C. A. Puliafito, and et al., "Optical coherence tomography," *Science* **254**, 1178-1181 (1991).
- [2]. A. Dufour, V. Shinin, S. Tajbakhsh, N. Guillen-Aghion, J. C. Olivo-Marin, and C. Zimmer, "Segmenting and tracking fluorescent cells in dynamic 3-D microscopy with coupled active surfaces," *IEEE Trans Image Process* **14**, 1396-1410 (2005).
- [3]. K. Jeong, L. Peng, J. J. Turek, M. R. Melloch, and D. D. Nolte, "Fourier-domain holographic optical coherence imaging of tumor spheroids and mouse eye," *Appl Opt* **44**, 1798-1805 (2005).
- [4]. K. Jeong, J. J. Turek, and D. D. Nolte, "Volumetric motility-contrast imaging of tissue response to cytoskeletal anti-cancer drugs," *Opt Express* **15**, 14057-14064 (2007).
- [5]. Z. Li, H. Sun, J. Turek, S. Jalal, M. Childress, and D. D. Nolte, "Doppler fluctuation spectroscopy of intracellular dynamics in living tissue," *J Opt Soc Am A Opt Image Sci Vis* **36**, 665-677 (2019).
- [6]. H. Choi, Z. Li, H. Sun, D. Merrill, J. Turek, M. Childress, and D. Nolte, "Biodynamic digital holography of chemoresistance in a pre-clinical trial of canine B-cell lymphoma," *Biomed Opt Express* **9**, 2214-2228 (2018).
- [7]. D. Merrill, R. An, H. Sun, B. Yakubov, D. Matei, J. Turek, and D. Nolte, "Intracellular Doppler Signatures of Platinum Sensitivity Captured by Biodynamic Profiling in Ovarian Xenografts," *Sci Rep* **6**, 18821 (2016).
- [8]. H. Sun, D. Merrill, R. An, J. Turek, D. Matei, and D. D. Nolte, "Biodynamic imaging for phenotypic profiling of three-dimensional tissue culture," *J Biomed Opt* **22**, 16007 (2017).
- [9]. S. Tozburun, C. Blatter, M. Siddiqui, E. F. J. Meijer, and B. J. Vakoc, "Phase-stable Doppler OCT at 19 MHz using a stretched-pulse mode-locked laser," *Biomedical optics express* **9**, 952-961 (2018).
- [10]. J. F. de Boer, B. Cense, B. H. Park, M. C. Pierce, G. J. Tearney, and B. E. Bouma, "Improved signal-to-noise ratio in spectral-domain compared with time-domain optical coherence tomography," *Opt. Lett.* **28**, 2067-2069 (2003).

- [11]. M. A. Choma, M. V. Sarunic, C. Yang, and J. A. Izatt, "Sensitivity advantage of swept source and Fourier domain optical coherence tomography," *Optics Express* **11**, 2183-2189 (2003).
- [12]. K. Kikuchi, "Characterization of semiconductor-laser phase noise and estimation of bit-error rate performance with low-speed offline digital coherent receivers," *Opt Express* **20**, 5291-5302 (2012).
- [13]. S. M. Kay and S. L. Marple JR, "Spectrum Analysis-A modern Perspective," *Proc. of the IEEE* **69**(1981).
- [14]. F. Detcheverry, "Generalized run-and-turn motions: From bacteria to Levy walks," *Phys Rev E* **96**, 012415 (2017).
- [15]. M. de Jager, F. J. Weissing, P. M. J. Herman, B. A. Nolet, and J. van de Koppel, "Lévy Walks Evolve Through Interaction Between Movement and Environmental Complexity," *Science* **332**, 1551 (2011).
- [16]. N. Humphries and D. Sims, "Optimal foraging strategies: Lévy walks balance searching and patch exploitation under a very broad range of conditions," *Journal of theoretical biology* **358**(2014).
- [17]. R. N. Mantegna, "Fast, accurate algorithm for numerical simulation of Levy stable stochastic processes," *Physical Review E* **49**, 4677-4683 (1994).
- [18]. N. N. Taleb, *The black swan : the impact of the highly improbable*, 1st ed. (Random House, New York, 2007), pp. xxviii, 366 pages.
- [19]. N. E. Humphries, H. Weimerskirch, N. Queiroz, E. J. Southall, and D. W. Sims, "Foraging success of biological Levy flights recorded in situ," *Proc Natl Acad Sci U S A* **109**, 7169-7174 (2012).
- [20]. F. S. Soo and J. A. Theriot, "Large-Scale Quantitative Analysis of Sources of Variation in the Actin Polymerization-Based Movement of *Listeria monocytogenes*," *Biophysical Journal* **89**, 703-723 (2005).
- [21]. F. E. Ortega, E. F. Koslover, and J. A. Theriot, "*Listeria monocytogenes* cell-to-cell spread in epithelia is heterogeneous and dominated by rare pioneer bacteria," *eLife* **8**, e40032 (2019).
- [22]. J. Slaghuis, M. Goetz, F. Engelbrecht, and W. Goebel, "Inefficient replication of *Listeria innocua* in the cytosol of mammalian cells," *J Infect Dis* **189**, 393-401 (2004).

- [23]. C. Kocks, J. B. Marchand, E. Gouin, H. d'Hauteville, P. J. Sansonetti, M. F. Carlier, and P. Cossart, "The unrelated surface proteins ActA of *Listeria monocytogenes* and IcsA of *Shigella flexneri* are sufficient to confer actin-based motility on *Listeria innocua* and *Escherichia coli* respectively," *Mol Microbiol* **18**, 413-423 (1995).
- [24]. S. Hannemann, B. Gao, and J. E. Galán, "Salmonella modulation of host cell gene expression promotes its intracellular growth," *PLoS Pathog* **9**, e1003668-e1003668 (2013).

APPENDIX A. DOPPLER LIGHT SCATTERING FROM INTRACELLULAR DYNAMICS OF SINGLE-CELL DERIVED SPHEROIDS

A.1 Cancer Metastasis and Circulating Tumor Cells (CTC)

Circulating tumor cells (CTC) are single cancer cells circulating in the bloodstream derived from a primary cancer tumor of a cancer patient. Extravasation of a CTC is the first step to metastasis, and investigation of the CTC mobility provides an early-stage diagnosis. Collecting CTCs from the bloodstream of a patient and measuring the chemosensitivity of CTCs to cytotoxic or targeted chemotherapeutics is one method to prescribe a personalized chemotherapy with higher efficacy for metastasis disease. To study the characteristics of CTCs in a metastatic stage, it would be advantageous to grow a multi-cellular three-dimensional tissue culture from a single CTC. In this study, small tumor spheroids were prepared by placing a single breast cancer cell (MCF7) on a collagen-I substrate in an RPMI-1640 growth medium. The CTC spheroids take about 2 weeks to grow up to a diameter of approximately 300 μm and 200 μm thickness.

A.2 BDI phenotype measurement of CTC-derived Spheroids

BDI illuminates the cancer spheroids with a low-coherence light source and collects backscattered light. A reconstructed optical section at a specified depth (200 μm) is shown in Figure A.1(a). Optical coherence image (OCI) and the corresponding motility contrast image (MCI) shows the characteristics of the dynamic speckle of a CTC spheroid. The geometry of the CTC spheroid is a two-layered system with a collagen substrate layer and a CTC spheroid layer which is shown in Figure A.1(b). The coherence-gate scans from the bottom up through the collagen layer and collects signals from the CTC spheroid. The collected signal carries Doppler shifts and the spectral density of the signal represents intracellular dynamics. Two chemotherapeutic agents (Doxorubicin and Taxol) were applied on CTC spheroids and changes in the Doppler spectra were measured. Doxorubicin inhibits DNA synthesis and causes apoptosis. Taxol inhibits microtubule synthesis which suppresses organelle transports and results apoptosis. Spectral densities before and after treatment are compared in Figure A.1(c).

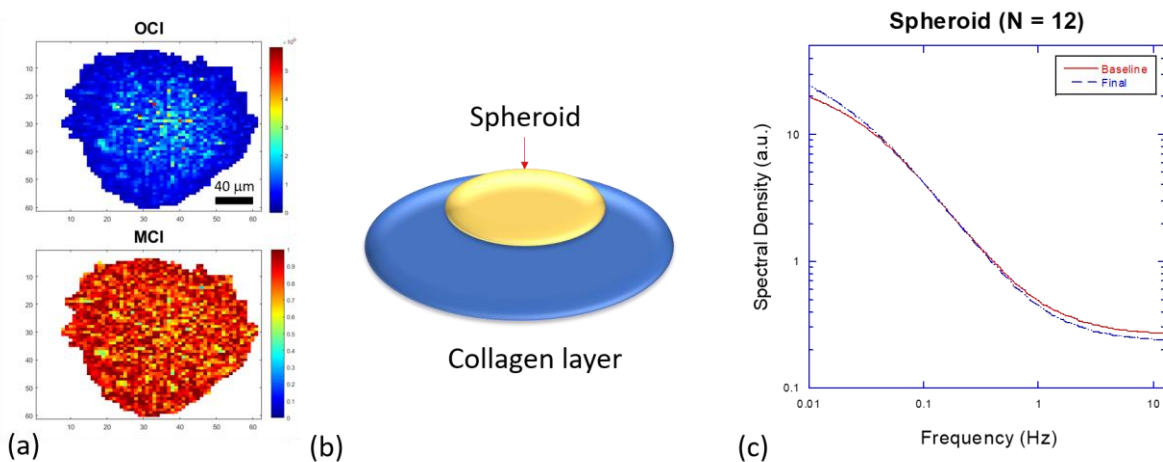


Figure A.1 (a) Digitally reconstructed OCI and MCI of a CTC spheroid. (b) Diagram of a CTC spheroid on the top of the collagen type-I layer. Incident light comes from beneath and backscattered light was collected. (c) Spectral density measured from a CTC spheroid on a poly-d-lysine plate.

A.3 Measurement of 3D Tissue on Collagen

To compare the intracellular dynamics of CTC spheroids with and without collagen, CTC spheroids were deployed on 500 μm thickness collagen layer and immobilized on poly-d-lysine plate. The spheroids were covered in the RPMI-1640 medium and maintained at 37 degrees Celsius. To measure the intracellular dynamic responses of CTC spheroid on the poly-d-lysine plate, 3 baselines and 15 post-dose responses were measured. After the baseline measurement, 100 μL of the RPMI-1640 medium was subtracted and 100 μL of RPMI-1640 medium with taxol (10 μM) or doxorubicin (20 μM) dissolved by 0.2% DMSO were applied to the well. The drug response spectrograms are shown in Figure A.2. The control group was treated by 0.2% DMSO for comparison.

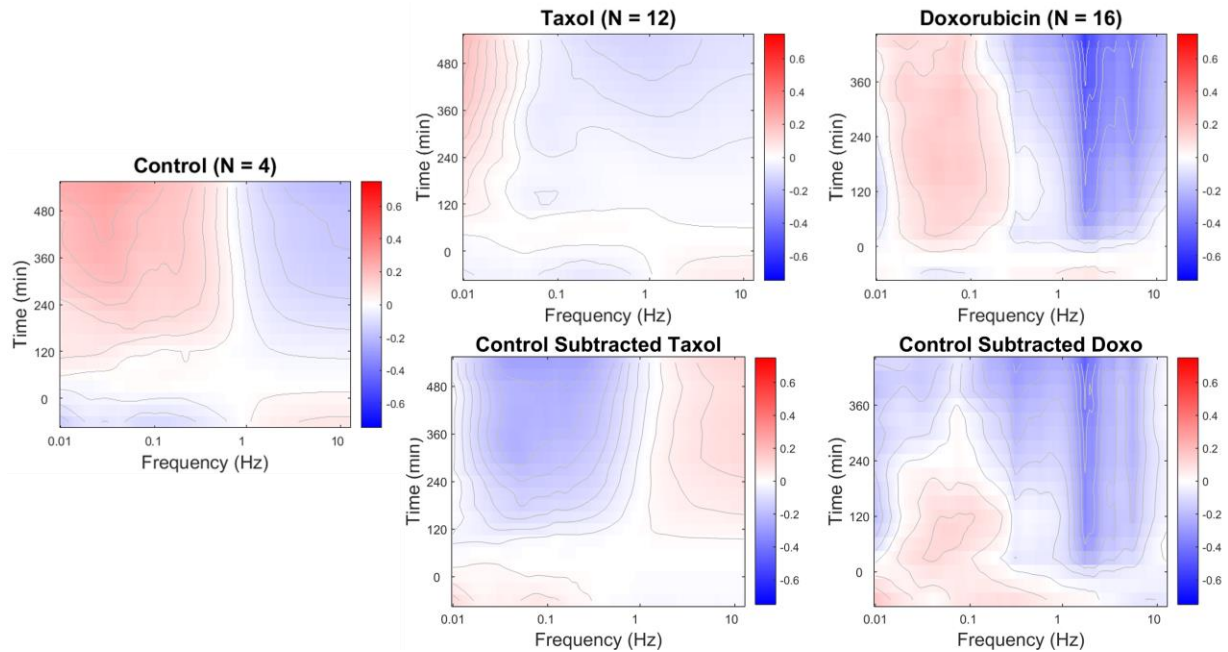


Figure A.2 drug response-spectrograms of 3D CTC spheroids grown from a single cell. Spheroids were deployed on a 96-well plate coated with poly-d-lysine for immobilization. The control and other groups treated by taxol or doxorubicin showed different spectral shifts. The group treated by taxol shows suppression of the mid-frequency compared to the control. The doxorubicin treatment shows a minor suppression at the low-frequency and high-frequency.

At the beginning of metastasis, a single CTC may become implanted in a receptive stromal microenvironment. To mimic such an environment, a 500 μm type-I collagen layer was used and a small breast cancer cell line (MCF7) spheroid was deployed on top of the collagen layer. Figure A.3 shows flythrough scanning images of OCT and MCI of a spheroid with 50 μm thickness on the collagen layer.

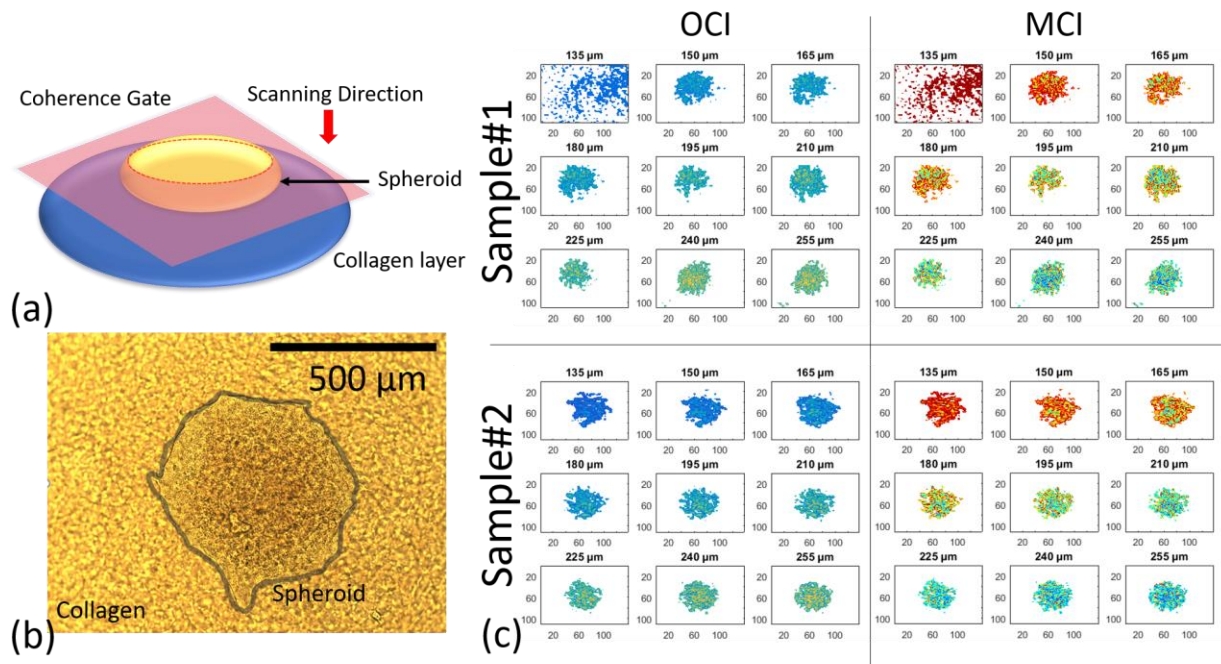


Figure A.3 (a) Diagram of the collagen layer and a spheroid structure and coherence-gating along the CTC spheroid. (b) microscopic image of the CTC spheroid. (c) OCI and MCI images of at successive depth scanning with a 15 μm scanning step. The collagen layer shows low speckle fluctuation.

The 3 dimensional CTC spheroid on the collagen layer showed different speckle properties at different depths. The backscatter brightness and motilities are compared in Figure A.4. Scanning through the collagen layer induces a strong background signal which makes the measurement challenging. The collagen layer scatters light 10 times more than the CTC spheroid. However, because of the advantage of the low-coherence light interferometry, a distinct difference in the motility is shown. The signal collected from the collagen layer has a motility lower than 0.5 and the motility gradually increased when the coherence-gate scanned through the CTC spheroid.

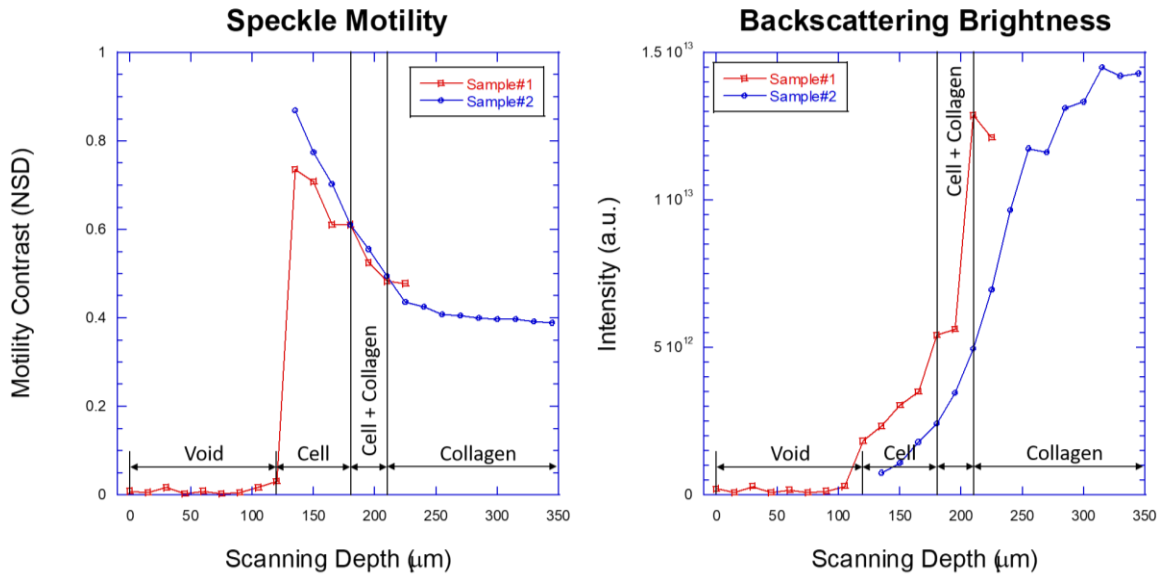


Figure A.4 BDI measurement of two CTC spheroids on a collagen layer. Speckle motility and backscatter brightness as a function of the depth of the coherence-gate. The segment with decreasing speckle motility shows an increasing backscatter brightness. The estimated CTC spheroid thickness is about 50 μm and the collagen layer scatters about 10 times more light than the CTC spheroid.

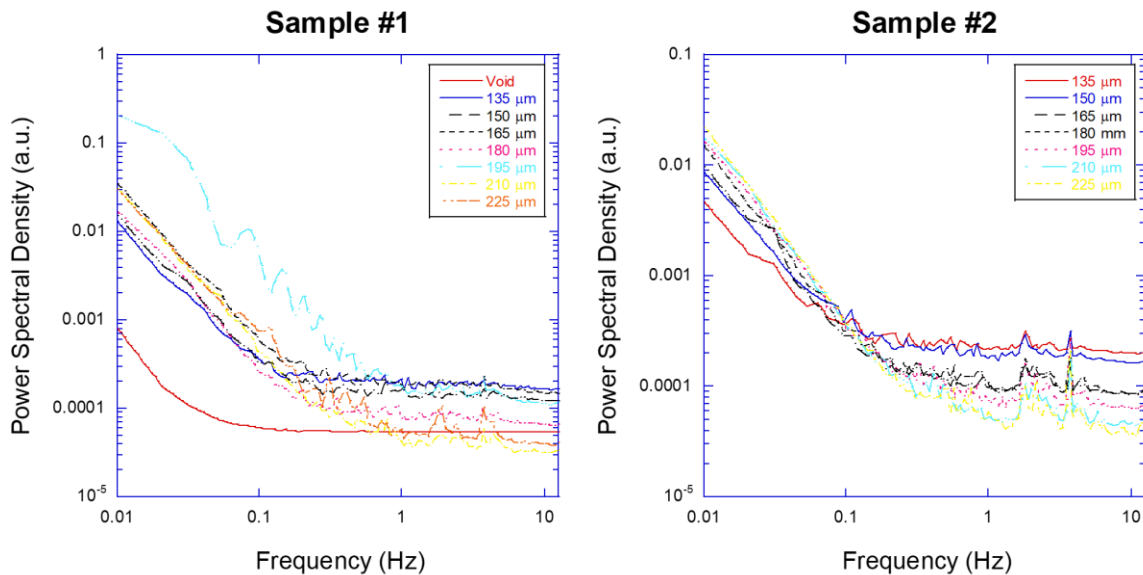


Figure A.5 Power spectral densities of two samples at different depths. Sample #1 shows spectral densities at a depth between 135 μm to 195 μm showing increased Nyquist floor which is expected when scanning the CTC spheroid. When a depth becomes deeper than 210 μm the Nyquist floor is suppressed. Scanning of Sample #2 shows the consistent behavior of decreasing the Nyquist floor when the coherence-gate scanned the collagen layer. Scanning of the void region did not show a spectral density. The spectral densities are intensity normalized.

Power spectral densities of single cell-derived spheroids on a collagen layer were measured. Because the collagen layer scattered significantly more light than the spheroids, the spectral densities shown in Figure A.5 has narrow dynamic ranges. Yet, the Nyquist floor characteristics show a consistent behavior that the spheroids have more high-frequency Doppler power spectral density. Scanning on a void region shows a flat and $1/f$ featured spectral density.

A.4 Discussion

This work demonstrates the possibility of measuring drug response phenotypes of living 3D CTC spheroids grown from a single cell. BDI scans through deep regions of biological samples by coherence-gated optical sectioning and measures intracellular dynamics. The intracellular dynamics are represented in terms of Doppler power spectral densities, and applying different reagents causes different spectral shifts. Applied chemotherapeutic agents taxol and doxorubicin induce different mechanisms of actions and also the Doppler power spectral responses.

A potential challenge for using BDI for this application is the use of the thick type-I collagen layer which scatters light 10 times more light than CTC spheroids which attenuate signals from the CTC spheroids. Living tissues tend to be translucent with weak backscatter brightness. Therefore, the high brightness and strong attenuation of the thick collagen layer combined with the thin living tissue layer with low backscatter could have precluded the use of BDI for the application. The experimental results presented here demonstrate that the living tissue dynamics are detectable despite the challenges posed by the growth structure.

The dynamic character of the signal from the living CTC-spheroids relative to the static collagen layers demonstrates a successful BDI profile of the CTC-spheroids response to applied chemotherapeutic agents. The Doppler shifts acquired by scattering in the CTC spheroids are carried through multiple scattering events in the collagen to the detector plane where the temporal fluctuations arise almost exclusively from the CTC spheroid layer despite the low signal levels. This trait is a key advantage of the application of BDI that enables tissue grown on the optically turbid collagen substrate to be characterized by the fluctuation spectroscopy.

The drug response spectrograms obtained through the application of taxol and doxorubicin are typical of these treatments that are observed in larger multicellular CTC spheroids. The control spectrum, where no therapeutic is applied, does show a drift of spectral weight to lower

frequencies, possibly caused by the change in environment on the sample stage. However, this background drift is substantially different than the drug responses to taxol and doxorubicin. Both drugs induce a mid-frequency (approximately 0.1 Hz) inhibition that has been correlated with an early apoptotic response. Therefore, this work has demonstrated the feasibility of performing optically-based phenotypic profiling of 3D tissue culture grown from single cells.

PUBLICATIONS

- [1]. S. Lee, W. Ha, H. Choi, J. Park, S. Kim, and K. Oh, "Ring defect photonic crystal fibers for low-loss and flattened dispersion," in *OECC 2010 Technical Digest*, 2010), 622-623.
- [2]. H.-J. Lee, J.-H. Ha, S.-G. Kim, H.-K. Choi, Z. H. Kim, Y.-J. Han, J.-I. Kim, Y. Oh, V. Fragoso, K. Shin, T. Hyeon, H.-G. Choi, K.-H. Oh, I. T. Baldwin, and C.-M. Park, "Stem-piped light activates phytochrome B to trigger light responses in *Arabidopsis thaliana* roots," *Science Signaling* **9**, ra106-ra106 (2016).
- [3]. H. Choi, Y. Jeong, and K. Oh, "Wide, tunable band rejection filter based on micro-optical waveguide on microactuating platform covering O, E, S, C, L, and U bands," *Opt. Lett.* **36**, 484-486 (2011).
- [4]. H. Son, H. Choi, and K. Oh, "Three-dimensional analysis of free-space light propagation based on quantum mechanical scattering theory of light," *Optics Communications* **382**, 533-538 (2017).
- [5]. H. Choi, M. Park, D. S. Elliott, and K. Oh, "Optomechanical measurement of the Abraham force in an adiabatic liquid-core optical-fiber waveguide," *Physical Review A* **95**, 053817 (2017).
- [6]. H. Choi, Z. Li, H. Sun, D. Merrill, J. Turek, M. Childress, and D. Nolte, "Biodynamic digital holography of chemoresistance in a pre-clinical trial of canine B-cell lymphoma," *Biomed Opt Express* **9**, 2214-2228 (2018).
- [7]. H. Choi, J. Turek, Z. Li, M. Childress, and D. Nolte, *Biodynamic imaging of therapeutic efficacy for canine B-cell lymphoma: preclinical trial results*, SPIE BiOS (SPIE, 2018), Vol. 10493.